# Tunneling Transport and Spectroscopy of Two-Dimensional Magnetic Materials

by

Bowen Yang

A thesis
presented to the University of Waterloo
in fulfillment of the
thesis requirement for the degree of
Doctor of Philosophy
in
Physics (Quantum Information)

Waterloo, Ontario, Canada, 2022

**Examining Committee Membership**

The following served on the Examining Committee for this thesis. The decision of the Examining Committee is by majority vote.

| | |
|---|---|
| External Examiner: | Young June Kim<br>Professor, Dept. of Physics, University of Toronto |
| Supervisor(s): | Adam Wei Tsen<br>Assistant Professor, Dept. of Chemistry,<br>University of Waterloo |
| Internal Member: | Jan Kycia<br>Professor, Dept. of Physics, University of Waterloo |
| Internal-External Member: | Guo-Xing Miao<br>Associate Professor, Dept. of Electrical and Computer Engineering, University of Waterloo |
| Other Member(s): | François Sfigakis<br>Research Assistant Professor, Dept. of Chemistry,<br>University of Waterloo |

## Author's Declaration

This thesis consists of material all of which I authored or co-authored: see Statement of Contributions included in the thesis. This is a true copy of the thesis, including any required final revisions, as accepted by my examiners.

I understand that my thesis may be made electronically available to the public.

## Statement of Contributions

The transfer system for device fabrication was designed and set up by Prof. Adam Wei Tsen (AWT) and Daniel McHaffie and was improved by Hyun Ho Kim (HHK) and Bowen Yang (BY). The He-4 cryogenic system for the low-temperature transport measurements in Chapter 7 was set up by AWT and Shazhou Zhong (SZ) and later maintained by SZ and BY.

1. Chapter 4:
   Published as: Hyun Ho Kim, Bowen Yang, Tarun Patel, Francois Sfigakis, Chenghe Li, Shangjie Tian, Hechang Lei, and Adam W. Tsen. "One million percent tunnel magnetoresistance in a magnetic van der Waals heterostructure." Nano Letters 18(8) (2018): 4885-4890

   - AWT and HHK designed the experiment. HHK and BY fabricated the devices with Tarun Patel's assistance and performed the low-temperature transport measurement with Prof. Francois Sfigakis (FS)'s assistance. HHK and BY operated a He-4 cryogenic system under the guidance of FS.
   - Chenghe Li (CL), Shangjie Tian (ST) and Prof. Hechang Lei (HL) grew and characterized the $CrI_3$ crystals.
   - HHK, BY and AWT analyzed the data.

2. Chapter 5 and 6:
   Published as: Hyun Ho Kim, Bowen Yang, Siwen Li, Shengwei Jiang, Chenhao Jin, Zui Tao, George Nichols et al. "Evolution of interlayer and intralayer magnetism in three atomically thin chromium trihalides." Proceedings of the National Academy of Sciences 116(23) (2019): 11131-11136.

   - AWT and HHK designed the experiment. HHK and BY fabricated the devices and performed the low-temperature transport measurement. HHK and BY operated a He-3 cryogenic system under the guidance of George Nichols.

- Siwen Li performed spin wave analysis under the guidance of Prof. Kai Sun and Prof. Liuyan Zhao.
- Shengwei Jiang (SJ) , Chenhao Jin and Zui Tao performed the magnetic circular dichroism measurement under the guidance of Prof. Jie Shan and Prof. Kin Fai Mak.
- CL, ST and HL grew and characterized the $CrI_3$ crystals.
- HHK, BY and AWT analyzed the data together with Prof. Guo-Xing Miao.

3. Chapter 7:
   This work is accepted in Nature Materials and waiting to be published at the time of finishing this thesis.

   - AWT and BY designed the experiment. BY fabricated the devices and conducted the transport measurement.
   - Yin Min Goh, Suk Hyun Sung, and Prof. Robert Hovden (RH) performed the electron diffraction measurement.
   - Gaihua Ye performed Raman spectroscopy measurement under the guidance of Prof. Rui He.
   - Sananda Biswas and David A. S. Kaib performed Density Function Theory calculations under the guidance of Prof. Rose Valentí (RV).
   - Prof. Stephen M. Winter (SMW) and Ramesh Dhakal performed *ab initio* calculations.
   - Shaohua Yan, CL and HL grew and characterized the $\alpha$-$RuCl_3$ crystals.
   - Fangchu Chen grew and characterized the $T_d$-$MoTe_2$ crystals.
   - SJ performed the magnetic circular dichroism measurement.
   - BY and AWT analyzed the data together with RH, RV and SMW.

## Abstract

The recent discoveries of magnetism in the single atomic layer have opened up a new direction for two-dimensional (2D) materials research. In this thesis, two types of magnetic materials are investigated: chromium trihalides and $\alpha$-$RuCl_3$.

Benefiting from the layer-dependent magnetism of few-layer $CrI_3$, we realize a very large negative magnetoresistance in a van der Waals heterostructure incorporating few-layer $CrI_3$, arising from spin flipping across the $CrI_3$ atomic layers. At certain voltage bias, the value of magnetoresistance reaches nearly one million percent. This finding provides new opportunities for spintronics devices and elucidates the nature of the magnetic state in ultrathin $CrI_3$.

Prompted by the large magnetoresistance in $CrI_3$, we then conduct a comprehensive study for the entire family of magnetic chromium trihalides ($CrX_3$, X=I, Br, Cl) by incorporating both few-layer and bilayer samples in van der Waals tunnel junctions. The tunneling measurements with magnetic field, combined with magnetic circular dichroism data, uncover interlayer magnetism, exchange gap and magnetic anisotropy of the three materials. Moreover, we demonstrate that ferromagnetism can persist down to monolayer in $CrBr_3$. We then perform inelastic electron tunneling spectroscopy measurement for studying their magnon excitations. Their spin Hamiltonians are later determined by fitting with spin wave calculations.

Finally, we change our focus to $\alpha$-$RuCl_3$, which is predicted to realize spin liquid in the frame of Kitaev physics. We use a combination of tunneling spectroscopy, magnetotransport, electron diffraction, and *ab initio* calculations to study the layer-dependent magnons, anisotropy, structure, and exchange coupling in atomically thin samples. We find that the extremely large magnetic anisotropy in bulk crystals is reversed in monolayer. Given that the predicted magnetic field to make a spin-liquid phase transition is hardly accessible in bulk crystals, this observation shows that quantum spin liquid phase is possibly easier to induce in a pure 2D limit.

**Acknowledgements**

First, I want to express my gratitude to my supervisor, Prof. Adam Wei Tsen, for the continuous support during the last five years. His guidance and enthusiasm in academic research helped me went through many difficulties in research and always pointed out a direction for me. I would also like to thank the members of my defence committee for critically reading this thesis and providing their comments.

In addition, I want to thank my past and present group members: Hyun Ho Kim, Fangchu Chen, Daozhi Shen, Tarun Patel, Shazhou Zhong, Archana Tiwari, Tina Dekker and Fangzhou Yin. In particular, I would like to thank Hyun Ho Kim. Most projects I was involved were accomplished with him. He was always working in the lab with full enthusiasm. I really appreciate that he was willing to share everything with me he knows in science with great patience. He let me know the correct attitude for research and set an example for me with his own conduct. I was very enjoying working with him, and I sincerely express my best wishes to him and his family. I also want to thank Fangchu Chen for his knowledge in crystal growing. Daozhi Shen and Tarun Patel are experts in optics. Thanks to them, I was able to acquire recent advances in optics and broaden my perspective. Besides, I am thankful to Shazhou Zhong for maintaining cryostat and thanks to him, nowadays our cryostat has been running for years without serious problems.

Outside our group, I want to thank Prof. Hechang Lei's group for the high-quality $CrI_3$ and $\alpha$-$RuCl_3$ crystals. I would like to thank Prof. Francois Sfigakis for teaching me about cryogenic instruments and electronics, as well as sharing with me his design of a breakout box. I am thankful towards Prof. Rose Valentí, Prof. Stephen M. Winter and their students for multiple fruitful discussions on $\alpha$-$RuCl_3$ project. Also, Prof. Robert Hovden and his students, Yin Min Goh, Suk Hyun Sung, did a great help on this project for performing electron diffraction measurement with hard efforts. I am also grateful to Prof. Rui He and her students, Gaihua Ye and Zhipeng Ye, for helping us taking Raman spectroscopy data. Besides, I want to thank Prof. Kin Fai Mak and Shengwei Jiang for their cooperation in our chromium trihalides project.

Lastly, words cannot express my thankfulness to my parents and my girlfriend, Zhenjie, for their love and support.

## Dedication

This is dedicated to my parents for their endless love and support.

# Table of Contents

# List of Figures

# List of Tables

# Chapter 1

# Magnetism: From Bulk to Two-Dimension

## 1.1 Magnetism and Heisenberg Model

Magnetism originates from spontaneous alignment of spins in various ways, corresponding to multiple magnetic phases; for example, spins point to the same directions in ferromagnetic materials, whereas nearest-neighbor spins are anti-parallel with each other in antiferromagnets. These diverse periodic patterns in spin alignments normally exist in a macroscopic scale, collectively forming a long-range order. Such diversity is dominated by spin-spin interactions, i.e., magnetic coupling. Couplings between spins have various forms, among which the exchange interaction is crucial, and widely exists in numerous magnetic systems.

Simply speaking, the exchange interaction or coupling can be established by the singlet-triplet energy difference of two-electron wavefunctions, due to the Coulomb interaction and Pauli exclusion principle as two electrons directly overlap with each other[1, 2, 3]. The spin Hamiltonian can be written as

$$H = -\sum_{<i,j>} J\mathbf{S}_i \cdot \mathbf{S}_j \tag{1.1}$$

where $J$ denotes the exchange coupling between two nearest-neighbor spins, $\mathbf{S}_i$ and $\mathbf{S}_j$. To minimize the energy, as $J$ is positive or negative, two adjacent spins favor parallel or antiparallel (ferromagnetic (FM) or antiferromagnetic (AFM)), respectively.

In addition to a simple direct interaction between two electrons, another mechanism that leads to exchange interaction is superexchange. Two adjacent transition-metal ions indirectly interact by coupling to the two electrons through a common nonmagnetic anion. The mechanism was proposed by Anderson[4]: one electron virtually hops from the ligand to a neighboring magnetic ion and then exchange interaction occurs between another electron on the ligand and the other neighboring magnetic ion. Goodenough[5] and Kanamori[6] predicted that the sign of superexchange interaction is dependent on the angle formed by two cations and one ligand and the number of d-shell electrons in cations. As the cation-ligand-cation angle is 180°, AFM interaction is expected between half-filled $d$ orbitals, whereas FM interaction is established between one half-filled and one empty orbital. In the case of 90°, superexchange interaction prefers to be FM.

There are more possible mechanisms to realize an exchange interaction[7]; for example, indirect exchange by interacting with surrounding conduction electrons, or double exchange through a mobile electron traveling between magnetic ions. They are not the focus of this thesis.

One may notice that such coupling is isotropic, which means that the interaction only depends on the relative orientation of two spins. There is no preferred direction for spins to align with and the collective orientation of spins is only determined by the direction of the applied magnetic field. However, in reality, magnetic anisotropy generally exists — higher (or lower) magnetic field is required to magnetize along the hard (or easy) axis. The formation of magnetic anisotropy relies on anisotropic magnetic interactions from a variety of sources[7] such as magneto-crystalline anisotropy, exchange anisotropy and the Dzyaloshinskii–Moriya (DM) interaction. One direct consequence of the magnetic

anisotropy is to induce a magnon excitation gap, which is essential for two-dimensional (2D) magnetism.

## 1.2 Two-Dimensional Magnetism

Nowadays, magnetic materials have been applied to various technologies, for example, data storage[8] or quantum spintronic devices[3]. Classical magnetic materials (bulk magnetism) gradually no longer satisfy the public's desire for miniaturization of electronic devices, and thus reduction of dimensionality in magnetic materials is urgently required. The attempts to reduce the size of magnets started in 1968[9]. A quasi-two-dimensional magnetic order was characterized by neutron scattering in a bulk system, $K_2NiF_4$, where the long-range magnetic order exists within the magnetic nickel ions. Since then, research in 2D magnets was activated and thanks to crystal growth techniques, in the last decade of the $20^{th}$ centuries, magnetic thin films with only single atomic layers were able to be grown on substrates[10].

However, some drawbacks still remain since these advances. First, even though quasi-2D magnetic order is achieved, the magnetic order still exists in a bulk crystal, hindering its application in real electronic devices. Second, interlayer coupling is still the key to stabilize the magnetic order, which is not an ideal case for fundamental studies of 2D magnetism. Third, growing monolayer magnetic materials on substrates is a great success, but defects are easily introduced during fabrication process and the strong adhesion between substrates also limits its practical use. Lastly, not only in experiments, at that moment the challenge for studying real freestanding 2D magnetic materials also remains in theory.

The Hohenberg-Mermin-Wagner theorem[11, 12] strictly proves that as dimensionality is reduced, at any nonzero temperature, the long-range order can be suppressed due to thermal fluctuations in a magnetic system, if the system only allows an isotropic short-range interaction. In contrast to 3D magnetic system whose magnon density of states (DOS) spectrum always increases from zero (Figure 1.1 a), such continuous symmetry

in an isotropic 2D system brings a finite DOS for magnons at zero excitation energy (gapless magnons) (Figure 1.1 b) [13, 14] and hence minute thermal energy sufficiently excite massive magnons, destroying the magnetic states.

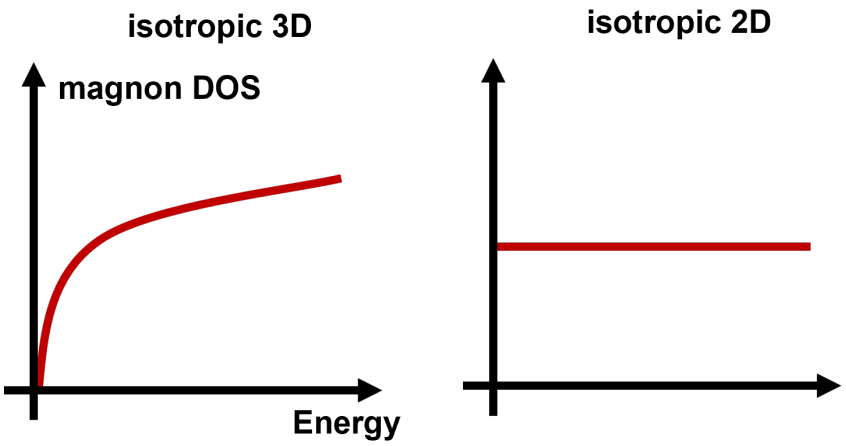


Figure 1.1: Schematics of magnon DOS spectrum in isotropic magnetic systems. (a) In 3D, magnon spectrum increases from zero DOS. (b) In 2D, magnon DOS is flat, starting from zero excitation energy. At a finite temperature, more magnons are excited in 2D than 3D. Reproduced from ref[14].

A few limitations should be pointed out for the famous theorem. First, the theorem only applies to isotropic systems with nearest-neighbor interactions, whereas long-range intralyer and interlayer interactions for few-layer crystals is hardly avoided. Second, the theorem considers an infinitely large 2D system, which implies finite-size effect might breaks the limitation for real 2D devices with micro-meter sizes. Third, defects or disorder, which is commonly observed in reality, is not included in the theoretical model since the theorem assumes an exactly continuous symmetry of Hamiltonian. Therefore, in order to realize and study 2D magnetism, various factors should be taken into accounts.

Despite of these limitations, breaking continuous symmetry is still the central factor to stabilize 2D magnetic order at nonzero temperature. The two-dimensional Ising model[15],

which hosts discrete symmetries, is one of the easiest ways to satisfy this.

In the Ising model, spins can be in one of two states (+1 or -1). The spin Hamiltonian is written as

$$H = -\sum_{<i,j>} JS_i^z S_j^z \tag{1.2}$$

The strong easy-axis anisotropy could open a spin wave excitation gap, giving rise to a compensation with finite thermal energy and thus stabilizing long-range magnetic order below a nonzero critical temperature (called Curie temperature for ferromagnets, $T_c$, and Néel temperature for antiferromagnets, $T_N$). However, in most circumstances, $T_c^{2D}$ is still lower than $T_c^{bulk}$ due to the interlayer exchange coupling. It is worth to note that such transition can be used to mark the crossover from bulk to a truly 2D characteristic[16].

In contrast to the easy-axis anisotropy, the XY model with easy-plane anisotropy was also theoretically investigated. In the XY model, orientations of all spins are constrained within the 2D atomic plane. In spite of the existence of magnetic anisotropy, the system is still not expected to possess a typical magnetic order due to the continuous symmetry, whereas Berezinskii-Kosterlitz-Thouless transition [17, 18] may occur at a finite temperature: At low temperature, vortex-anivortex pairs are formed and decay in relatively slow rate at boundaries, leading to a quasi-long-range order within an atomic layer. This is not the focus of this thesis.

Inspired by the isolation of freestanding graphene in 2003[19], experimentalists then turned to "van der Waals materials" whose magnetic anisotropy has been reported in bulk form. In 2017, the difficulties listed above were overcome with the discovery of 2D magnetism in two van der Waals materials, $CrI_3$[20] and $Cr_2Ge_2Te_6$[14]. A brief introduction to van der Waals materials is given in the next section.

## 1.3 Van der Waals Materials

2D materials are a family of ultrathin crystalline solids with thickness of single or few atomic layers. Together with layered ionic solids and surface assisted nonlayered materials[21], various van der Waals materials, which is the focus of this thesis, constitutes the field of 2D materials. The most well-known van der Waals materials is graphene[19], leading to a Nobel Prize in 2010 for its extraordinary physical properties and subsequently hundreds of various van der Waals materials were discovered and investigated for their interesting properties and potential applications in field-effect transistors[22], spintronic devices[23], and optical devices[24] etc.

Van der Waals material is not merely a thin crystal. Layered graphite consists of loosely stacked graphene layers and behaves as a conductor of electricity. Once carbon layers are segregated, the monolayer graphene behaves like a semimetal with no bandgap. The linear dispersion near Dirac points leads to emergence of massless Dirac Fermion[19, 25]. Emergent phenomena including integer and fractional quantum hall effect were discovered [26, 25, 27]. In contrast, bandgap opens in bilayer graphene and highly tunable with external electric field[28].

Such extensive research inspired exploration on other 2D materials, broadening the 2D family to semiconductors and insulators, along with discovery of more unprecedented properties. One representative is transition metal dichalcogenides, which cover from insulators to conductors. For example, bandgap of $MoS_2$[29] transitions from indirect to direct as the thickness is reduced to monolayer, dramatically enhancing the intensity of photoluminescence compared to bilayer and bulk crystals. These examples unveil how important the role of dimensionality control is playing in fundamental studies of condensed matter physics.

For van der Waals materials, in-plane strong covalent bonds stabilize each atomic layer, and rather weak van der Waals interaction between layers allows easy separation of layers. This feature provides a unique opportunity to design and fabricate any desired artificial

nanostructure for various purposes, called van der Waals heterostructures, by simply stacking isolated atomic layers of van der Waals materials from top to bottom (see Section 3.3 for more fabrication details). Compared with traditional growth methods, van der Waals heterostructures break the constraints of lattice matching and processing compatibility[30], yielding an ultraclean and atomically sharp interface.

One example in practical use is tunnel devices with hexagonal boron nitride (h-BN). The large bandgap ($\sim$ 6 eV) [31] and perfectly flat surface free of dangling bonds[32] makes it an excellent choice for tunnel barriers. Previous work has demonstrated a prototype of field-effect tunneling transistors by integrating h-BN with graphene as electrodes and external gates[33]. Moreover, due to its chemical stability and high breakdown voltage, h-BN is widely used as protection layer of van der Waals heterostructures from oxidation[20].

## 1.4 Pristine 2D Magnetic Materials: Van der Waals Magnets

Since the discovery of graphene, various attempts have been concentrating on extrinsically inducing magnetism in nonmagnetic van der Waals materials, by either introducing defects for breaking continuous symmetry[34] or proximity effect[35] relying on the sharp interface in van der Waals heterostructure. In 2017, the chapter for 2D magnetic materials was started by two van der Waals chromium compounds: $CrI_3$[20] and $Cr_2Ge_2Te_6$[14], wherein $CrI_3$ is one of the focuses in this thesis.

Bulk $CrI_3$[36] and $Cr_2Ge_2Te_6$[37] both are ferromagnetic semiconductors with easy-axis anisotropy, which motivated researchers to explore the 2D magnetism for these materials. Monolayer $CrI_3$ is an Ising-type ferromagnetic 2D semiconductor (Figure 1.2 a). The Curie temperature is 45 K, slightly lower than the bulk $T_c$ (61 K[36]) due to the weak interlayer exchange coupling. In contrast, thin $Cr_2Ge_2Te_6$ follows Heisenberg model with a weak magnetic anisotropy generated by a small unit-cell distortion, slightly lifting the

Hohenberg-Mermin-Wagner restriction (Figure 1.2 b). The Curie temperature of bilayer $Cr_2Ge_2Te_6$ drops by over 50%, compared to the bulk case, and the magnetic order has to be stabilized with assistance of a small external field (0.065 T). Stimulated by these ground-breaking results, intrinsic 2D magnetic materials have been broadened to a big and growing family in the recent years.

Our work evidences that the other two analogues to $CrI_3$, $CrBr_3$ and $CrCl_3$, are also able to maintain magnetism down to the atomically thin limit using the magnetic-optical Kerr effect and tunneling spectroscopy (see Chapter 5 and 6). In parallel, Klein et al. also reported similar findings[38]. In addition, some other transition metal chalcogenides compounds similar to $Cr_2Ge_2Te_6$ have also been discovered to have 2D magnetism. $FePS_3$[39] is the one with Ising-type antiferromagnetism in few-layer structure and $Fe_3GeTe_2$[40] is the first conducting 2D Ising-type ferromagnet. The Curie temperature of monolayer reaches as high as 130 K (even though it is still quite lower than bulk $T_c = 205$ K). Surprisingly, the $T_c$ was discovered to be highly tunable with electric doping and was finally able to increase up to room temperature, providing possibilities for practical use.

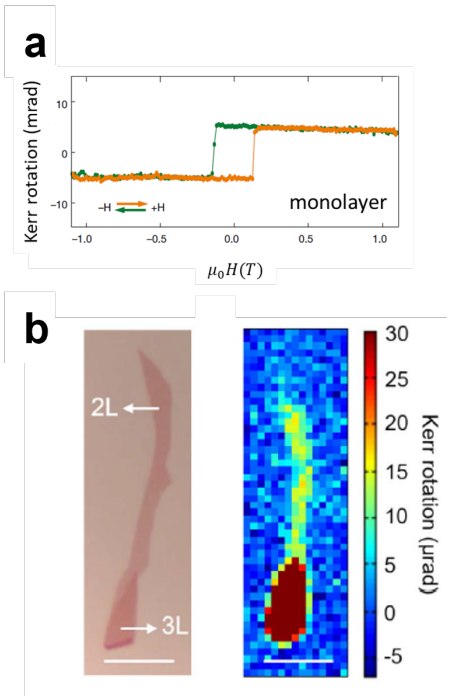


Figure 1.2: 2D magnetism in $CrI_3$ and $Cr_2Ge_2Te_6$. (a) Magnetic-optical Kerr effect (MOKE) signal of graphite-sandwiched monolayer $CrI_3$ as a function of applied magnetic field. The hysteresis loop shows indicates the existence of FM with easy-axis anisotropy. (b) Optical image and Kerr image of bilayer and trilayer $Cr_2Ge_2Te_6$ exfoliated on $SiO_2$/Si with scale bars of 10 mm. The Kerr response indicates easy-axis ferromagnetic nature. Adapted from ref[20] and [14].

Having such new role joining in the sizable 2D material library with dispersive fascinating properties, van der Waals heterostructure displays more possibilities for future applications, for instance, low-power spintronics: Instead of h-BN, with a 2D magnetic semiconductor serving as tunnel barrier in a tunnel junction, tunneling resistance could be easily tuned by external magnetic field. We fabricated such magnetic tunnel junction by incorporating few-layer $CrI_3$ with graphene electrodes, demonstrating an incredibly large magnetoresistance (see Chapter 4).

What I listed above only covers a few van der Waals magnets in monolayer or few-layer structures verified in experiments. A full library based on experimental observations and theoretical prediction can be found in several review papers[3, 41], one of which provides a detailed summary of van der Waals magnetic materials[3] (Figure 1.3). In this table, only one van der Waals material owns a unique color code: $\alpha$-$RuCl_3$. The crystal is considered as a candidate for long-sought exotic state of matter, Kitaev quantum spin liquid (KQSL) state, hosting long-range coherence and fractionalized excitations. The application in fault-tolerant topological quantum computing[42] attracted tremendous interest in pursuing the KQSL state. In the past decades, theoretical and experimental work both focused on bulk crystal whereas KQSL is a 2D model. My last three years of PhD program primarily concentrated on investigating magnetism of the monolayer and few-layer $\alpha$-$RuCl_3$ and the work is shown in Chapter 7.

<table>
<tr><td>Chalcogenides</td><td>$Cr_2Ge_2Te_6$, $Cr_2Si_2Te_6$, $Fe_3GeTe_2$, $VSe_2$*, $MnSe_x$*</td><td colspan="2">$Fe_2P_2S_6$, $Fe_2P_2Se_6$, $Mn_2P_2S_6$, $Mn_2P_2Se_6$, $Ni_2P_2S_6$, $Ni_2P_2Se_6$, $CuCrP_2Se_6$*, $AgVP_2S_6$, $AgCrP_2S_6$, $CrSe_2$, $CrTe_3$, $Ni_3Cr_2P_2S_9$, $MnBi_2Te_4$*, $MnBi_2Se_4$*</td><td>$CuCrP_2S_6$</td></tr>
<tr><td rowspan="2">Halides</td><td rowspan="2">$CrI_3$*, $CrBr_3$, $GdI_2$</td><td rowspan="2">$CrCl_3$, $FeCl_2$, $FeBr_2$, $FeI_2$, $MnBr_2$, $CoCl_2$, $CoBr_2$, $NiCl_2$, $VCl_2$, $VBr_2$, $VI_2$, $FeCl_3$, $FeBr_3$, CrOCl, CrOBr, CrSBr, $MnCl_2$*, $VCl_3$*, $VBr_3$*</td><td>$CuCl_2$, $CuBr_2$, $NiBr_2$, $NiI_2$, $CoI_2$, $MnI_2$</td></tr>
<tr><td>α-$RuCl_3$</td></tr>
<tr><td>Others</td><td>$VS_2$, $InP_3$, GaSe, GaS</td><td>$MnX_3$ (X = F, Cl, Br, I), $FeX_2$ (X = Cl, Br, I), MnSSe, $TiCl_3$, $VCl_3$</td><td>SnO, GeS, GeSe, SnS, SnSe, GaTeCl, CrN, $CrB_2$</td></tr>
</table>

Figure 1.3: Van der Waals magnets library. Green: bulk ferromagnetic van der Waals crystals; Orange: bulk antiferromagnets; Yellow: bulk multiferroics; Gray: theoretically predicted van der Waals ferromagnets (left), half metals (center), and multiferroics (right); Purple: $\alpha$-$RuCl_3$(a proximate Kitaev quantum spin liquid). Adapted from ref[3].

## 1.5 Thesis Outline

This thesis concentrates on transport properties and spectroscopy of atomically thin 2D van der Waals magnetic materials: chromium trihalides and $\alpha$-$RuCl_3$, whose magnetic properties for interlayer and intralayer couplings are discussed in Chapter 2. The mechanism for the tunneling measurements we perform is introduced in Chapter 3.

In Chapter 4, we report a very large magnetoresistance by tunneling current through few-layer $CrI_3$. This emergent phenomenon is attributed to the change between antiparallel to parallel alignment of spins across layers of A-type antiferromagnetic $CrI_3$. We find that the magnetoresistance is able to reach one million percent under certain conditions, which is a few orders of magnitude larger than other common magnetic systems.

Relying on the significant spin-filtering effect, in Chapter 5, we further conduct a systematic study for the interlayer magetism of the three chromium trihalides, together with magnetic circular dichroism measurement, in which the types of interlayer coupling, magnetic anisotropy and exchange splitting gaps are determined. In addition, we prove the existence of ferromagnetism in monolayer $CrBr_3$, with transition temperature surprisingly close to that of the bulk and the antiferromagnetism of $CrCl_3$ survives down to bilayer limit.

Chapter 6 reports the magnetic excitations for three three chromium trihalides, $CrI_3$, $CrBr_3$, and $CrCl_3$. By incorporating bilayer samples in van der Waals tunnel junctions, we find that magnon excitations evolve with changing halogen atom in inelastic electron tunneling spectrums. By fitting to a spin wave theory that only considers nearest-neighbor exchange interactions, we are able to determine magnetic couplings for all three bilayer systems and classify them into Ising, anisotropic Heisenberg, and XY spin models.

In Chapter 7, we shift our focus to a more complicated magnetic system: $\alpha$-$RuCl_3$. As mentioned, the crystal is a promising material to potentially realize the long-sought Kitaev quantum spin liquid with fractionalized excitations. While evidence of this exotic state has been reported under a modest in-plane magnetic field, such behavior is largely

inconsistent with theoretical expectations of Kitaev phases emerging only in out-of-plane fields. These predicted field-induced states are out of reach due to the strong easy-plane anisotropy of bulk crystals, however. Motivated by the results in chromium trihalides family, we continue to use tunneling spectroscopy to investigate the strong correlated system. Together with magnetotransport, electron diffraction, and *ab initio* calculations, we explore layer-dependent magnons, anisotropy, structure, and exchange coupling in atomically thin samples.

In Chapter 8, the thesis is summarized and I discuss about the potential application of twisting technique in modulating interlayer magnetic coupling in bilayer $CrI_3$.

# Chapter 2

# Magnetic Interactions of 2D van der Waals Magnetic Materials

Compared with other materials, van der Waals materials do not have a relatively strong interaction between layers including exchange interaction, and thereby magnetic couplings should be categorized into two classes: interlayer and intralayer coupling. In the chapter, 2D magnetism of the two materials we focus on, chromium trihalides ($CrX_3$, X=Cl, Br, I) and $\alpha$-$RuCl_3$, is introduced.

## 2.1 Chromium Trihalides

### 2.1.1 Intralayer coupling

Within each layer, Cr atoms form a honeycomb lattice, and each two nearest neighbour Cr atoms are separated by two X atoms. Then six X atoms, surrounding a single Cr atom, forms an edge-sharing octahedra (Figure 2.1). In such environment, Cr atom is oxidized and contributes three electrons to the surrounding ligands, thereby having three electrons

on the outer shell with electron configuration of $3s^2 3d^3$. In this scenario, $X^-$ ions have no paired electrons and becomes purely non-magnetic.

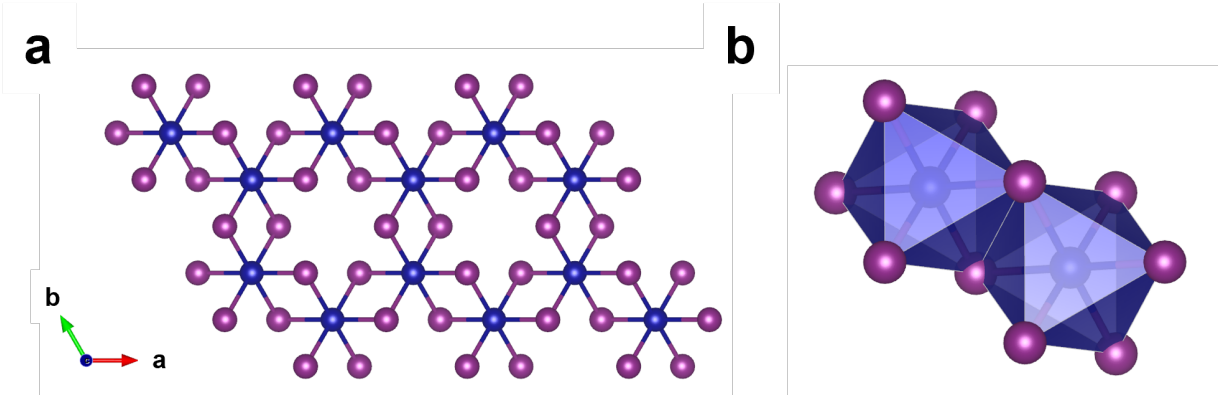


Figure 2.1: Illustration of monolayer $CrI_3$ structure. (a) Bird's eye view of monolayer. (b) Edge-sharing octahedra. Rendered from the crystallographic data in ref[36].

In an octahedral environment, five degenerate $d$ orbitals should split into two states: triply $t_{2g}$ orbitals with lower energy, and doubly $e_g$ orbitals with higher energy, due to crystal field splitting (Figure 2.2 a). Figure 2.2 b shows the band structure of $CrI_3$ in fully ferromagnetic configuration from standard density functional theory (DFT) calculation. The three outer electrons separately occupy the $t_{2g}$ manifold with parallel spins (spins point up) by following Pauli exclusion principle and the first Hund's Rule. It forms the valence band, resulting in quench of total orbital moments[43]. The empty $e_g$ states, which also favour up spins, form the bottom of the conduction band. With minority spin (spins point down), $t_{2g}$ states are even higher than $e_g$ states with majority spins. As a consequence of exchange interaction, this spin-dependent band gap is referred to exchange splitting or exchange gap, leading to the spin-filtering effect discussed in Chapter 3. At the same time, total spin of $S = 3/2$ from the three unpaired electrons contribute entire magnetic moment of each $Cr^{3+}$ ion with orbital moments $L = 0$, leading to ordered moments of $\sim 3\mu_B$ for $CrX_3$.

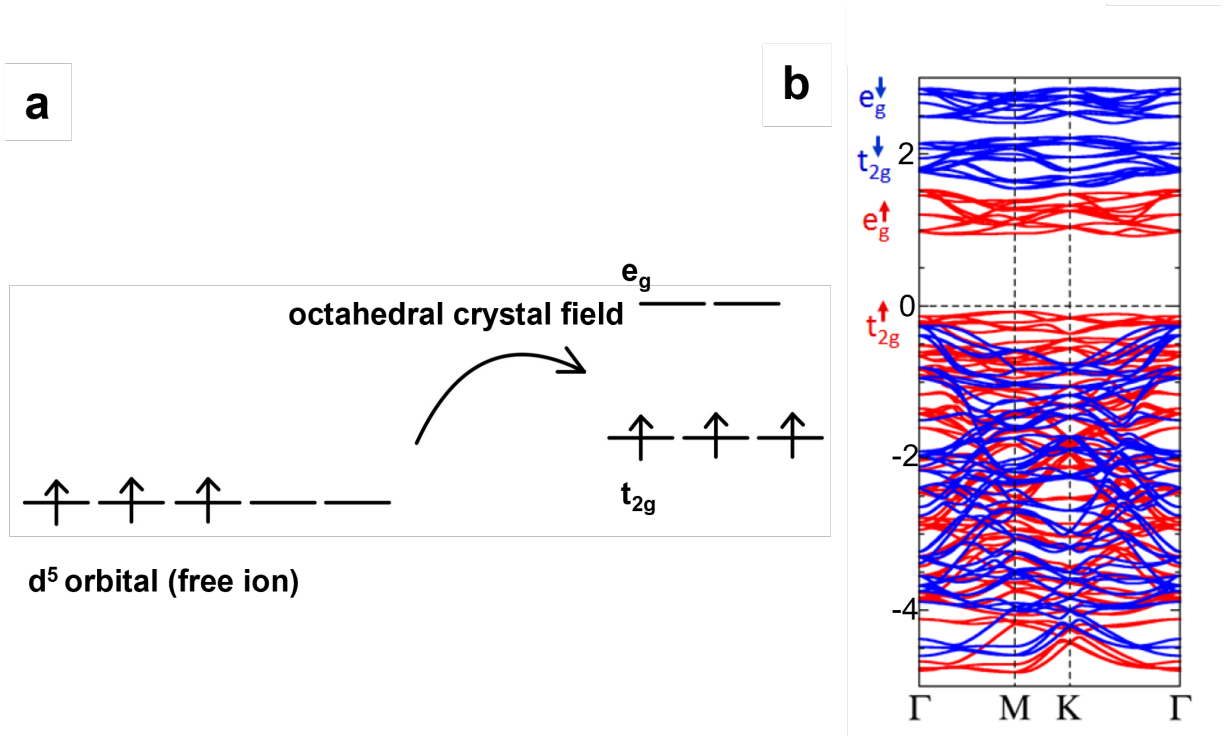


Figure 2.2: Crystal field splitting in an octahedral environment. (a) Crystal field splitting diagram for $Cr^{3+}$ ions. (b) DFT calculations for bulk $CrI_3$. Spin-dependent bands are clearly shown and an exchange splitting gap is formed between $e_g^{\uparrow}$ and $t_{2g}^{\downarrow}$. Adapted from ref[44].

Interaction between magnetic cations determine which type of magnetism each layer forms. Direct interaction is negligible due to large separation of $Cr^{3+}$ ions ($\sim$ 4 Å[36]). Due to the semiconductor nature, indirect interaction is forbidden and only superexchange mechanism is possible. Superexchange is a virtual interaction between the half filled $t_{2g}$ and the empty $e_g$, mediated by the $p$ orbitals of non-magnetic ligands. In the case of $CrX_3$, the angle is nearly 90 degree, yielding a strong ferromagnetic coupling, $J > 0$ between $Cr^{3+}$ ions, according to the Goodenough-Kanamori rule.

As mentioned in Chapter 1, different magnetic anisotropies could possibly stem from

DM interaction, magneto-crystalline anisotropy, exchange anisotropy. DM interaction is inherently forbidden by inversion symmetry of the Cr-X-Cr bonds[45]. The other two couplings are allowed by such symmetry, whereas density functional theory results have shown that for $CrI_3$, the magneto-crystalline anisotropy is significantly weaker than exchange anisotropy[43]. Such easy-axis magnetic anisotropy in $CrI_3$ predominantly originates from the SOC of iodine. With reducing the element number of halogen, the strength of SOC from ligands is weakened. For $CrCl_3$, SOC in Cl is negligible and thus holds the weakest magnetic anisotropy originating from shape anisotropy, which broadly exists in classical magnetic mediums.

Based on the above discussion, in the early studies for the $CrX_3$ system, a simplified generic spin Hamiltonian can be proposed with the addition of exchange anisotropy:

$$H = -\sum_{<i,j>} J\mathbf{S}_i \cdot \mathbf{S}_j - \lambda \sum_{<i,j>} S_i^z S_j^z \tag{2.1}$$

where $\lambda$ represents the exchange anisotropy. More terms are shown to be required for precisely describing the 2D magnetic systems by later studies[46], such as Heishenberg interactions and DM interaction on next-nearest neighbors. It should also be noticed that, since interlayer coupling is over one order of magnitude smaller than intralayer coupling $J$ [47], interlayer exchange interaction is not included in the simple spin Hamiltonian, either.

### 2.1.2 Interlayer coupling

In contrast to the bulk $CrI_3$, few-layer $CrI_3$ exhibits antiferromagnetic coupling between ferromagnetic layers (A-type antiferromagnetism). The interlayer interaction is missing in Equation 2.1 and above discussion cannot interpret why bulk $CrI_3$ is ferromagnet whereas thin $CrI_3$ is A-type antiferromagnetic. Such confliction indicates that the interlayer magnetic exchange is changed as crystals are thinned.

The interlayer coupling is driven by a more complicated interaction: super-superexchange[48, 49], where virtual electron hopping between the $Cr^{3+}$ $d$ orbitals through the $p$ orbitals of two

nearby $I^-$ anions. This process depends on the orbital overlapping between ions, and thus the stacking order and relative angles of layers greatly affects the interlayer magnetic order. Ultimately, in case of $CrI_3$, which favours ferromagnetism and antiferromagnetism in rhombohedral and monoclinic, respectively. Above 200 K, $CrI_3$ has monoclinic structure[36]. As cooled below 200 K, the structure for bulk $CrI_3$ is rhombohedral[36], whereas 2D $CrI_3$ stacking remains unchanged at low temperature[50, 51]. Below the Curie temperatures (bulk: 61 K; few-layer: 45 K), for bulk and thin cases, low-temperature structures imply ferromagnetic and antiferromagnetic exchange, respectively, which are consistent with the observed interlayer magnetic couplings of $CrI_3$.

Similar to bulk $CrI_3$, bulk $CrBr_3$ is ferromagnet with easy-axis anisotropy below $T_c$=37 K[52], while bulk $CrCl_3$[53] has antiferromagnetic coupling between layers with easy-plane anisotropy below the Néel temperature $T_N$=17 K (see Figure 2.3 for summary). Their interlayer magnetism is later shown in our work (see Chapter 5) and several relevant works[54, 38]: antiferromagnetic and ferromagnetic interlayer coupling persist down to bilayer for $CrCl_3$ and $CrBr_3$, respectively, with minor decrease in critical temperatures.

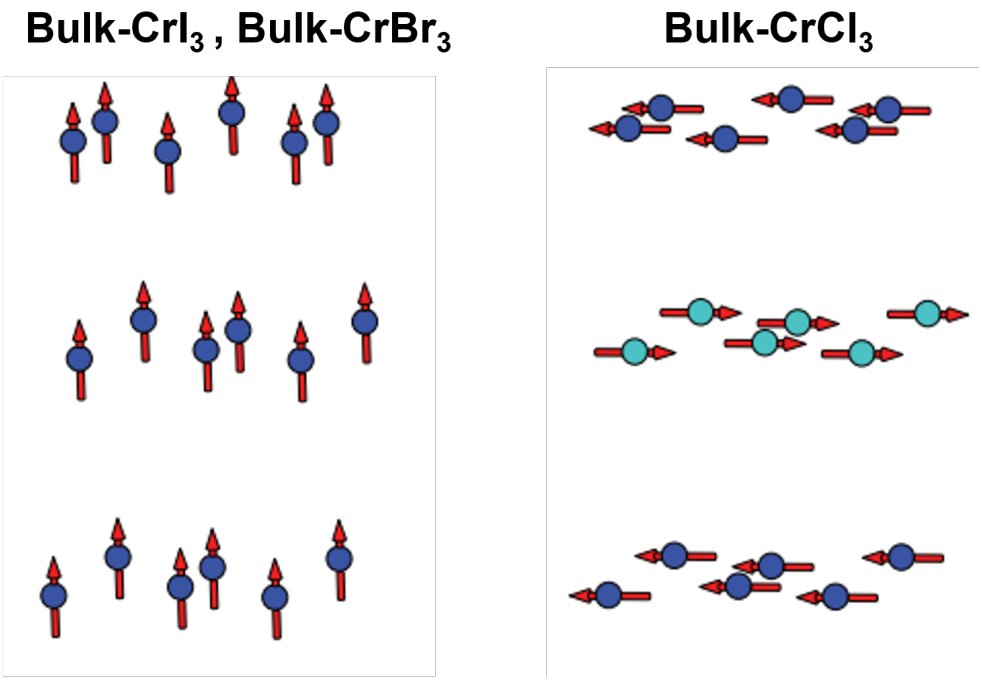


Figure 2.3: Interlayer magnetic coupling for bulk $CrX_3$. Adapted from ref[55].

## 2.2 $\alpha$-$RuCl_3$

### 2.2.1 Kitaev model

The Kitaev model is a celebrated spin-1/2 model on the 2D honeycomb lattice with bond-dependent Ising interactions[56], which features a highly entangled quantum spin liquid (QSL) ground state, fractionalized Majorana excitations, and a series of magnetic-field-induced quantum phase transitions[56, 57, 58, 59, 60, 61, 62]. This model was proposed by Alexei Kitaev with exact solution in 2006. The Kitaev Hamiltonian has three orientation-dependent Ising-type terms for each site on the honeycomb lattice:

$$H = \sum_{<i,j>} S_i^\gamma S_j^\gamma \tag{2.2}$$

where $\gamma = \{x, y, z\}$, correlating to the X-, Y- and Z-bonds, shown in Figure 2.4. In this Hamiltonian, spin-spin interaction depends on the type of the bond connecting the two nearest neighbour spins with easy axes parallel to x-, y-, and z-axes, perpendicular to each other. In this scenario, it is impossible to satisfy all interactions simultaneously. In a classical picture, infinite degenerate magnetic states are allowed at ground state. As the quantum mechanical effect is turned on, the magnetic frustration leads to a highly entangled QSL state.

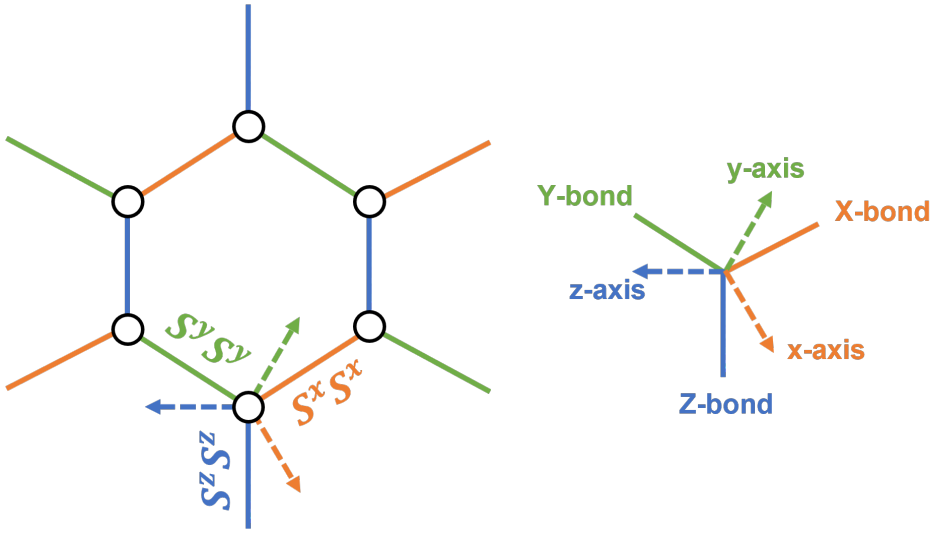


Figure 2.4: The Kitaev model. Color code: orange denotes X-bond; green denotes Y-bond; blue denotes Z-bond. Corresponding to three bonds, three easy axes can be defined. Each axis is perpendicular to its correlated bond and the three axes are perpendicular to each other. To be noted that even though it is a 2D model, the three axes are not coplanar.

### 2.2.2 Jackeli-Khaliullin mechanism and $\alpha$-$RuCl_3$

The search for materials realizing the Kitaev model has been an ongoing challenge for over a decade and may potentially lead to applications in fault-tolerant topological quantum computing[42]. The mechanism for realizing Kitaev interaction was proposed by Jackeli and Khaliullin[63] in 4d and 5d transition-metal-based Mott insulator with strong SOC. They considered the magnetic interaction between adjacent $d^5$ ions in an octahedral environment, where the crystal field splits the $d$ orbitals into $t_{2g}$ (lower energy) and $e_g$ (higher energy) states. The strong SOC further splits $t_{2g}$ states into two states with total angular momentum of $j_{eff} = 1/2$ and $j_{eff} = 3/2$, with higher and lower energies, respectively. Then the $j_{eff} = 3/2$ state is fully filled and leave one hole localized in $j_{eff} = 1/2$ subject to strong electronic correlation (large Hubbard limit), as shown in Figure 2.5.

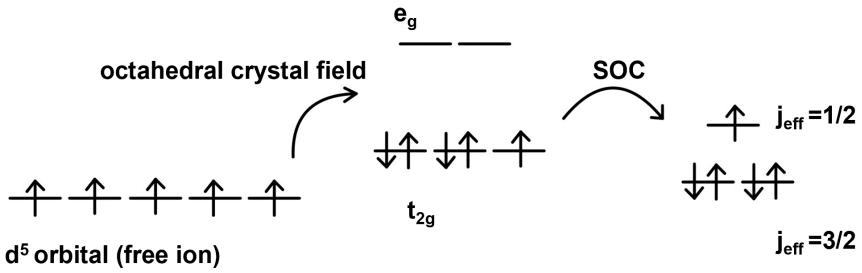


Figure 2.5: Formation of $j_{eff} = 1/2$ moments for ions in a $d^5$ electronic configuration.

For the strongly coupling system, a generic Hamiltonian should be considered[64]:

$$H = \sum_{<i,j>} J_{ij}\mathbf{S}_i \cdot \mathbf{S}_j + \mathbf{D}_{ij} \cdot (\mathbf{S}_i \times \mathbf{S}_j) + \mathbf{S}_i \cdot \mathbf{\Gamma}_{ij} \cdot \mathbf{S}_j \tag{2.3}$$

where $J_{ij}$ is the Heisenberg term, $\mathbf{D}_{ij}$ is the DM term and $\mathbf{\Gamma}_{ij}$ is the symmetric pseudo-dipolar tensor.

Apparently, a pure Kitaev system requires net zero for Heisenberg term, DM interaction and off-diagonal components of pseudo-dipolar tensor and only one diagonal component

should remain nonzero (for example, only $\Gamma_{zz}$ on the diagonal in the pseudo-dipolar tensor is nonzero as the $< i, j >$ bond is z-type). Jackeli and Khaliullin[63] proved that an idealized edge-sharing octahedra with inversion symmetry is able to realize such condition. Considering the virtual hopping between the two neighbouring magnetic ions through the ligands on the shared edge, the hopping path between two $j_{eff} = 1/2$ states is cancelled out by interference, whereas the path between $j_{eff} = 1/2$ and $j_{eff} = 3/2$ is allowed. Then the two holes individually on $j_{eff} = 1/2$ and $j_{eff} = 3/2$ are interacting through Hund's coupling, yielding a bond-dependent Ising interaction, Kitaev interaction.

However, non-Kitaev interactions inevitably present in real materials[64]: direct exchange between *d*-*d* orbital hopping; next-nearest neighbour exchange due to the extended $4d$ and $5d$ orbitals; and DM term due to deviation from ideal octahedral environment (cation-ligand-cation angle is not perfectly 90 degree). These factors may lead to extensions of the Jackeli-Khaliullin mechanism with various coupling terms (Heisenberg, off-diagonal in $\mathbf{\Gamma}_{ij}$, next-nearest neighbor, etc.) and almost always drive the ground state away from the Kitaev QSL phase with magnetic orderings. Therefore, a careful tuning of the exchange parameters is needed[65, 66, 67, 64].

In this thesis, we work with a layered van der Waals material that is a particularly promising candidate to realize Kitaev physics, $\alpha$-$RuCl_3$. Similar to chromium trihalides, edge-sharing RuCl6 octahedra form a honeycomb lattice and adjacent layers are coupled by van der Waals interaction. Together with the nature of spin-orbit assisted Mott insulator, the nearly ideal octahedral structure is likely to satisfy Jackeli-Khaliullin mechanism. As shown in Chapter 7, tuning for magnetic coupling is achieved by spontaneous structure distortion down to monolayer limit.

As a consequence of these non-Kitaev interactions, the ground state of $\alpha$-$RuCl_3$ is zigzag (ZZ) antiferromagnetic (AFM) below Néel temperature $T_N \sim 8$ K with strong easy-plane anisotropy[68], although this ordering can be suppressed with the application of an $\sim$ 6–8 T in-plane magnetic field. The presence of a half-integer thermal quantum Hall effect has been reported in this intermediate phase at low temperature[69, 70], while an

unusual continuum of magnetic excitations can be seen even without magnetic field that persists far above the Néel temperature[71, 72]. Both observations hint at $\alpha$-$RuCl_3$ being in proximity to a QSL, making it a current subject of intense scrutiny. However, two main problems remain unsolved and hinder further investigation.

- Experimental debate: Recent experiments[73, 74, 75] have indicated the possibility of a phase analogous to the Kitaev spin liquid being accessed at the intermediate in-plane fields in the bulk, where the zigzag magnon is completely gapless. However, this finding remains controversial because no extended Kitaev model has yet been demonstrated to feature such a phase, despite extensive theoretical searches, and several contradictory results have been reported to show a gapped nature of the zigzag magnetic order[76, 77].

- Inaccessible experimental condition: From a theoretical point of view, a QSL induced by in-plane field generally cannot be accounted for, as most calculations for $\alpha$-$RuCl_3$ show Kitaev phases more broadly emerging from an out-of-plane field[61, 78, 79, 80, 81]. Due to the strong easy-plane magnetic anisotropy of bulk crystals, however, prohibitively high fields above 30 T are required to access such states[82, 83, 84].

The interlayer coupling is still under debate due to the unclear mechanism of interaction between atomic layers[85, 86]. Moreover, the reported stacking fault in $\alpha$-$RuCl_3$[87] makes the interlayer interaction even more mysterious. Given that the Kitaev model is purely a 2D model, in this thesis, we only focus on the intralayer magnetism in this system.

# Chapter 3

# A Probe for Interlayer Coupling and Magnetic Excitations: Tunneling Heterostructure

Chromium trihalides and $\alpha$-$RuCl_3$ crystals are layered van der Waals semiconductor with various band gaps (1.2 eV, 2.1 eV, 2.3 eV and 1.9 eV for $CrI_3$[88], $CrBr_3$[89], $CrCl_3$[89], $\alpha$-$RuCl_3$[90], respectively), thereby offering a chance to perform a tunneling measurement to investigate the magnetic properties down to few-layer and even monolayer limit. Here, we propose two mechanisms for studying interlayer and intralayer magnetism, using a tunneling heterostructure Metal/Magnetic Barrier/Metal, as shown in Figure 3.1 a.

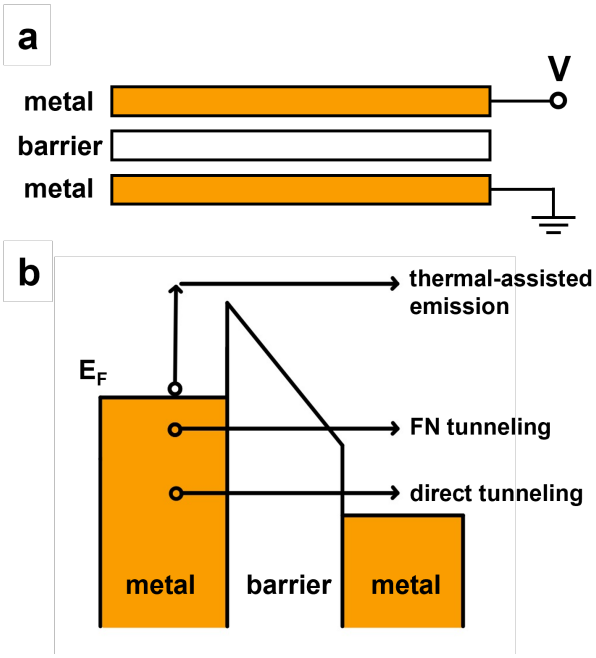


Figure 3.1: Tunneling heterostructure with a voltage bias. (a) Metal/Magnetic Barrier/Metal heterostructure. A voltage bias is applied between the two electrodes. (b) Three types of transmission mechanisms.

## 3.1 Interlayer Magnetism: Fowler–Nordheim Tunneling and Spin-Filtering Effect

As a voltage bias is applied between the two metallic layers, quantum mechanics predicts a nonzero tunneling probability. Generally, three types of transmission may occur: direct tunneling, Fowler-Nordheim (FN) tunneling and thermal-assisted tunneling (Figure 3.1 b).

In direct tunneling, the emitted electron tunnels across the whole barrier, which always happen in general cases. As the voltage bias increases, electrons in the metallic electrode, especially close to the Fermi level, shall see the canted top of the energy barrier with a thinner barrier. The whole tunneling process is thus strongly dependent on the bias:

the higher the voltage bias is, the more dominant the FN tunneling will be. At high temperature, another mechanism is enabled. Electrons close to the Fermi surface are thermally excited over the bottom of conduction band in barrier, and thus moves freely across the barrier.

The current-voltage relation for direct and FN regimes can be expressed as[91]:

$$\ln \frac{I_{direct}}{V^2} \propto \ln \frac{1}{V} - \frac{2d\sqrt{2m_e\Phi}}{\hbar} \tag{3.1}$$

$$\ln \frac{I_{FN}}{V^2} \propto -\frac{4d\sqrt{2m_e\Phi^3}}{3\hbar e}\left(\frac{1}{V}\right) \tag{3.2}$$

where e is electronic charge, $V$ is the applied bias across the barrier, $m$ is the effective electron mass, which we estimate to be the free-electron mass, $\hbar$ is the Planck's constant, and $\Phi$ is the barrier height. In principle, by applying a linear fitting between $\ln(I/V^2)$ and $1/V$ (or $\ln(1/V)$) to current-voltage characteristic curves, we can extract the barrier height from Equation 3.2 (or 3.1). However, since FN tunneling is dominant at higher voltage regime, where the signal-to-noise ratio is higher, in practice we normally use FN tunneling to extract the barrier height.

For ferromagnetic materials, the energy barrier becomes spin-dependent, due to the presence of exchange splitting gap (Figure 3.2 a). Above the Curie temperature, exchange gap does not exist, and then energy barrier, $\Phi_{PM}$, is related to paramagnetic (PM) state. Below the Curie temperature, between minority and majority spins, an exchange splitting gap is open at the original barrier height (Figure 3.2 b), and two tunneling barriers are generated, determined by the minority- and majority-spin energy band, yielding two tunneling currents. The current through the lower majority-spin band dominates. Then the energy barrier extracted from the current-voltage characteristic curve can be approximated as majority-spin energy band ($\Phi_{FM}$). As the exchange splitting is turned on or off, from FN tunneling, we can measure $\Phi_{FM}$ or $\Phi_{PM}$, respectively. Therefore, we can approximately estimate this fundamental quantity for ferromagnetic materials by $E_{ex} = 2(\Phi_{PM}–\Phi_{FM})$. Moreover, since the tunneling electrons with the majority spin is dominant, the current

becomes spin-polarized after tunneling, just like "filtered" by the spin-dependent barriers. Therefore, this effect is called spin-filtering effect.

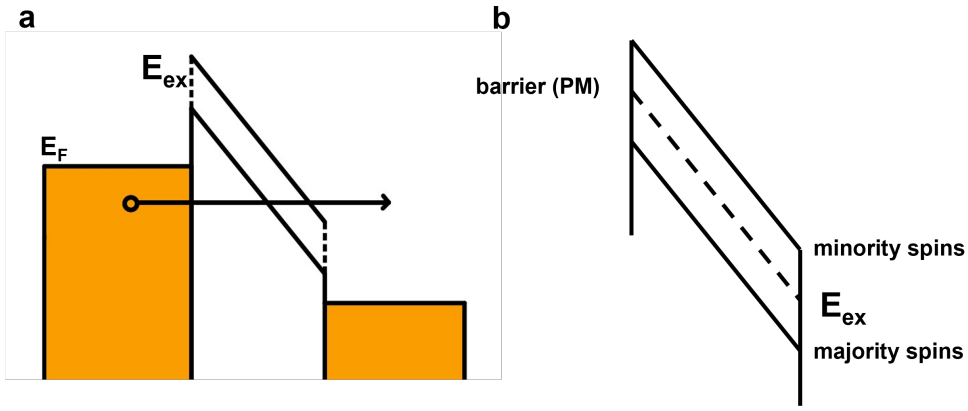


Figure 3.2: Spin-dependent energy barriers for tunneling currents. (a) Ferromagnetic tunneling barrier below Curie temperature. (b) The exchange gap is formed between minority-and majority-spin energy bands. The dashed line represents the barrier height above $T_c$, where the system is in PM state.

Furthermore, the spin-filtering effect can be utilized for achieving large magnetoresistance. An idea of double spin-filering junction was introduced in the early 2000s[92]. The magnetic tunneling barrier is composed of two magnetic layers with unequal coercivities. Above the Curie temperature, both layers behave paramagnetically. Below the Curie temperautre, due to the difference in coercivities, we can achieve two spin configurations: parallel and antiparallel (Figure 3.3). When the two layers' magnetization is parallel, the whole junction behaves as a normal spin-filtering junction, resulting in a rather low resistance and a highly spin-polarized current. When the magnetization is antiparallel, the electron crossing the lower (higher) barrier in the first layer will have to cross the higher (lower) barrier in the second layer, yielding a high resistance and non-polarized current.

This double spin-filtering junction provides a new approach to determine the interlayer ordering between ferromagnetic intralayer (for example, chromium triiodide). If the inter-

layer coupling is ferromagnetic, as temperature decreases across the Curie temperature, since the "parallel" configuration naturally forms, a decrease in resistance is expected and vice versa.

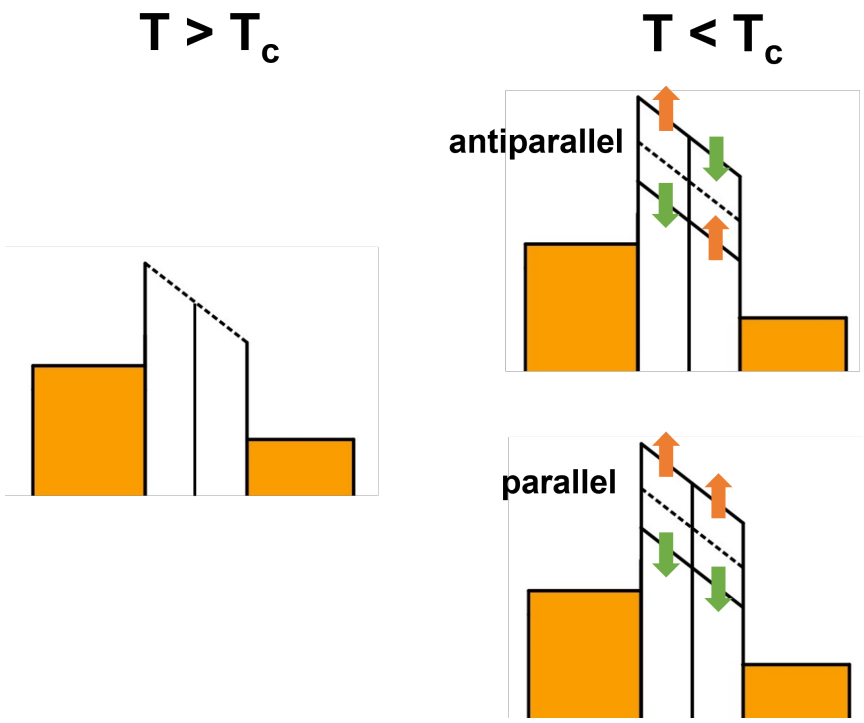


Figure 3.3: Schematic illustration for double spin-filtering junction across the critical temperature. The dashed line represents the barrier height above $T_c$, $\Phi_{PM}$. Reproduced by ref[93].

## 3.2 Intralayer Magnetism: Inelastic Electron Tunneling Spectroscopy

Inelastic electron tunneling spectroscopy (IETS) has been used for probing collective vibration mode (phonons) in molecular junctions[94], and magnons[95]. The first attempt

for 2D magnetic materials was made in 2018[96], inspiring us to explore the magnetic excitations using this technique.

In Section 3.1, we assume that electron tunneling is elastic. This approximation should fail as the sample barrier becomes thinner (tunneling resistance is reduced) and the applied bias is small, since the tunneling electrons might scatter with a quasi-particle excitation in the barrier. Such inelastic tunneling channel could significantly change conductance. When the junction voltage increases above the energy of an inelastic excitation (phonon or magnon), theoretically, the AC conductance ($dI/dV$) will abruptly increase as a new inelastic tunneling channel is opened (Figure 3.4 a). In an idealized scenario, this conductance increase will take the form of a step function, and so the derivative ($d^2I/dV^2$) will exhibit a sharp peak at the excitation energy (Figure 3.4 b).

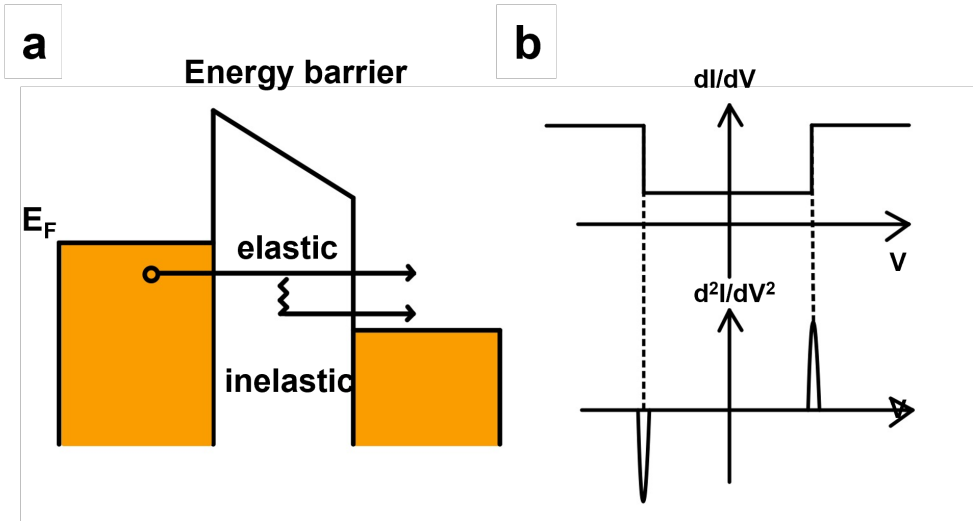


Figure 3.4: Schematic illustration of inelastic electron tunneling spectroscopy. (a) Energy band diagram of a tunnel junction. We can see that with a minute bias applied, Fowler-Nordheim tunneling is not allowed. (b) The corresponding $dI/dV$ and $d^2I/dV^2$ as a function of bias. The position of the symmetric peaks equals to the excitation energy.

Realistically, the conductance contributed by the elastic background cannot be ignored

and completely flat for a tunneling barrier. Additionally, since the excitation is not infinitely sharp due to finite width of density of states, we may simply see a rise in the conductance when the excitation energy is reached, yielding a peak feature in $d^2I/dV^2$.

The peak width is affected by two factors[97]: thermal fluctuation and instrumental broadening, defined as following, respectively:

$$\chi(V) = \frac{1}{kT}\exp(x)\frac{(x-2)\exp(x)+x+2}{(\exp(x)-1)^3} \tag{3.3}$$

$$\phi(V) = \begin{cases} \frac{8}{3\pi}\frac{1}{eV_\omega^4}\left(V_\omega^2 - V^2\right)^{\frac{3}{2}} & |V| < V_\omega \\ 0 & |V| \geq V_\omega \end{cases} \tag{3.4}$$

where $x = eV/KT$ and $V_\omega$ is AC excitation amplitude.

The predicted linewidth of $\chi$ and $\phi$ at half maximum is $5.4kT$ and $1.22eV_\omega$. Hence, the two broadening factor requires the measurement should be performed at cryogenic temperature and low AC excitation. During the measurement, the AC excitation is minimized and thus can be ignored. In the case that we need to explicitly determine the peak width and intrinsic integrated intensity, it is therefore necessary to remove the thermal broadening component to extract the intrinsic IETS peak properties[97]:

$$d^2I/dV^2 = D(V) * \chi(V) \tag{3.5}$$

where $D(V)$ represents the intrinsic IETS signal and $*$ stands for convolution operator. This data analysis is utilized in Chapter 7.

## 3.3 Tunneling Heterostructure Fabrication

Since the discovery of graphene, a few innovative approaches ($Al_2O_3$ method[40], gold method[98], liquid method[99]) for obtaining thin flakes of 2D materials have been developed, some practical problems could be created, limiting the scope of use; for example, the surface of flakes is easily contaminated by polymer residue or degraded in the air, or

the exfoliated flakes can hardly be transferred due to the strong adhesion to substrate. The traditional method, mechanical exfoliation, is adopted for all crystals discussed in this thesis with some variations in details.

With an intact bulk crystal with a clean and smooth surface, we attach the crystal firmly on a Nitto SPV tape for $\alpha$-$RuCl_3$ or Scotch tape for other 2D crystals. In each time of folding the tape, due to the extremely weak van der Waals bonds between layers, each crystal piece is cleaved into two pieces on two sides of the tape. The resulting tape with exfoliated graphite is shown in Figure 3.5 a. Such process typically should be repeated 4-5 times. One thing to be noted is that for the air-sensitive crystals, such as $CrI_3$, the whole exfoliation necessitates the use of glovebox filled with inert gas ($N_2$ or Argon).

Then the next step is to obtain and transfer thin nanoflakes from these thick pieces on tapes to $SiO_2$/Si substrate. Empirically, we have two options, as shown in the Figure 3.5 b, for various crystals we use:

1. For $CrBr_3$ and $CrCl_3$, we exfoliate these thin bulk pieces on a polydimethylsiloxane (PDMS) block and flakes can be obtained on PDMS. Then attach the side with flakes on substrates and slowly peel the PDMS off, during which part of flakes could be transferred.

2. For graphene, h-BN, $CrI_3$, and $\alpha$-$RuCl_3$, we directly attach the tape with crystals on clean $SiO_2$/Si substrates with a gentle press for better contact. Then slowly peel off the tape, at the moment that some flakes are exfoliated from the tape due to the adhesion of the substrate. For $CrI_3$, and $\alpha$-$RuCl_3$, we find that it is more efficient to leave the tape on substrates over 24 hours and then quickly peel off the tape.

Eventually, we obtain flakes on silicon chips with thickness ranging from monolayer to microns. By distinguishing different optical contrast with an optical microscope, we can identify these flakes with different thickness, especially lower than five atomic layers.

To assemble these flakes into a heterostructure, these flakes need to be picked up and stacked together from top to bottom by using a dry method, requiring the use of polycarbonate (PC) film. A piece of 5 mm $\times$ 5 mm PC film is mounted at end of a glass slide with a small PDMS block of $\sim$ 2 mm $\times$ 2 mm $\times$ 1 mm beneath at center. The four edges of the PC film are fixed by Scotch tapes. The inserted PDMS block lifts up the PC film, allowing a uniform contact between flakes and PC film. A schematic picture and an example of the assembly are shown in Figure 3.5 c and d.

Then the prepared "pick-up" tool is mounted on an X-Y-Z motorized translation stage with precision less than 1 um (Figure 3.5 e). Since both PC and PDMS are transparent, we can align the target flake with the next one. During the pick-up process (Figure 3.5 f), the PC film is softened at $\sim$ 90 °C and conform with the target flake on substrate. As cooled to $\sim$ 60 °C, the flake can be easily picked up due to van der Waals forces between the flat surfaces. Once the desired stack is finished, the whole structure is transferred to a pre-patterned electrode by melting the PC film at $\sim$ 150 °C. At such high temperature, the film should be delaminated from the PDMS block, and the device is in contact with the electrodes and $SiO_2$ substrate with the PC film capped on. Lastly, the PC film is supposed to be removed by dipping the substrate in chloroform for 60 seconds.

Compare with wet methods[100], the dry method introduces minor residue at the interface and quality of van der Waals structure is largely improved as surface of each flake only contacts with other 2D material in this process.

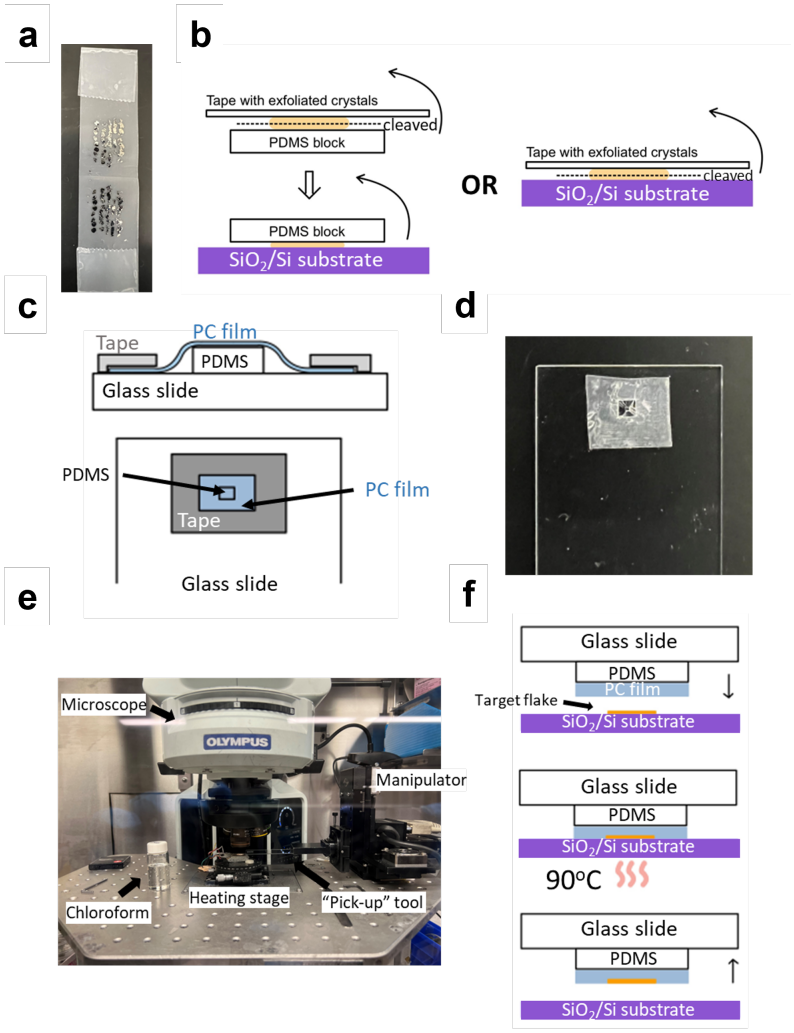


Figure 3.5: Device fabrication. (a) An example exfoliation for graphite. (b) Two ways for exfoliation onto $SiO_2$/Si substrate. (c) "Pick-up" tool. Upper panel: sideview of the "pick-up" tool. The PC film is fixed by a piece of tape with a square hole at center. Lower panel: bird's-eye view of the tool. The PDMS block is beneath the PC film (d) An example of the "pick-up" tool. The PDMS bock is $\sim$ 2 mm by 2 mm, barely seen in the image. (e) The assembly setup consisting of a microscope, a heating stage and a x-y-z controlled motorized manipulator. The "pick-up" tool is fixed on the manipulator. (f) Schematic of the pick-up process.

# Chapter 4

# Large Magnetoresistance in a Magnetic van der Waals Heterostructure

In the above chapters, we briefly describe the unique 2D magnetism for $CrI_3$: antiferromagnetic interlayer coupling and ferromagnetic intralayer conpling with out-of-plane easy axis. In this chapter, relying on the remarked properties, we present new opportunities for spintronics incorporating magnetic 2D materials.

In this work, we demonstrate a tunnel junction heterostructure consisting of magnetic semiconductor, $CrI_3$, sandwiched between few-layer graphene electrodes and sealed with h-BN. Under voltage biasing, we observe a negative magnetoresistance close to one million percent at low temperature under an applied field of $\sim$ 2 T, a value on par with that of colossal magnetoresistance (CMR) in the manganites[101, 102]. We attribute the cause to the spin-filtering effect arising from full polarization of spins in the magnetic semiconductor[103, 93], and experimentally determine the exchange gap through magnetotransport measurements.

This chapter is based on our published work in *Nano Letters*[104] with modifications.

## 4.1 Van der Waals Tunnel Junction

In Figure 4.1 a, we show a schematic illustration of the device. Within a nitrogen-filled glovebox, thin $CrI_3$ was electrically contacted above and below by few-layer graphene and fully encapsulated with h-BN to prevent reactions with the ambient environment. An optical image of the finished device is shown in Figure 4.1 b. We confirmed that our $CrI_3$ bulk crystal has similar properties with previous reports (Figure 4.2)[20, 36]. Figure 4.2 a and b show ferromagnetic behaviour with magnetic anisotropy as large as $\sim 3$ T. The kinks and peaks in the parts c and d correspond to Curie temperature for bulk crystals, $\sim 61$ K. The assembly and fabrication procedure are described in greater detail in Section 3.3.

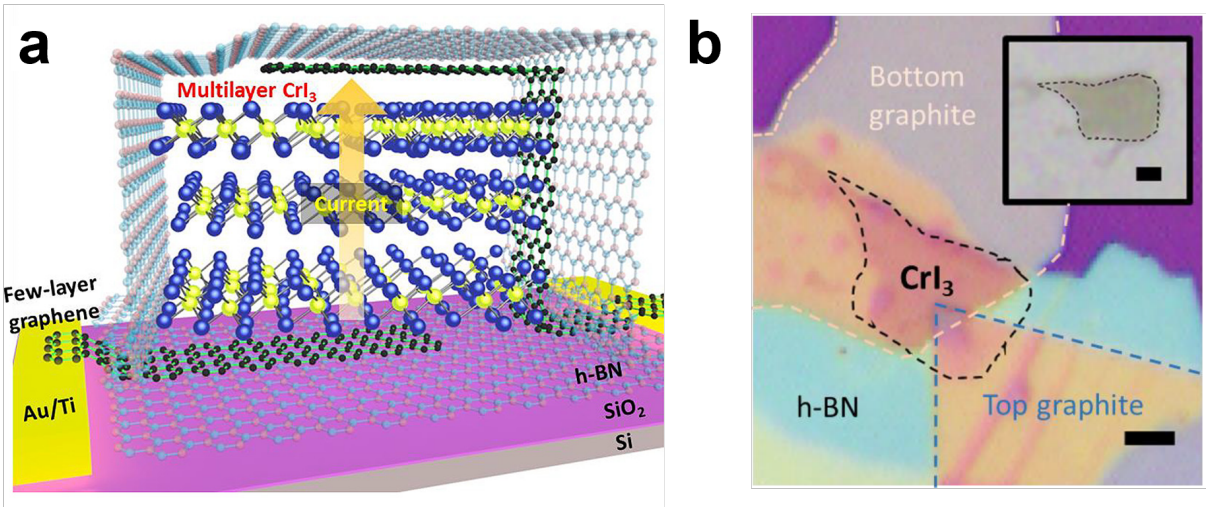


Figure 4.1: Vertical van der Waals heterojunction device incorporating magnetic $CrI_3$. (a) Schematic illustration of the device. (b) Optical image of device with 10-layer-thick $CrI_3$ before covering with top h-BN. Inset shows transmission optical microscope image of $CrI_3$ flake. Scale bars: 5 $\mu$m.

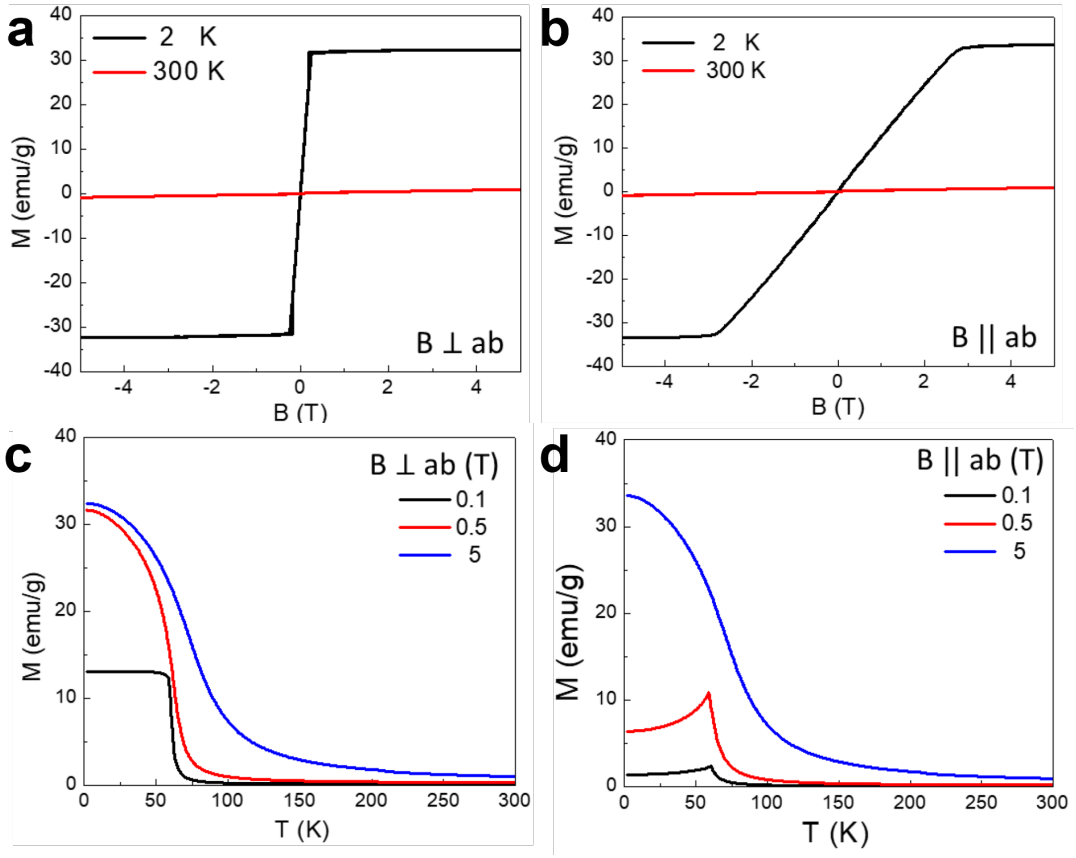


Figure 4.2: Magnetization of bulk crystal vs. magnetic field for (a) B⊥ab and (b) B‖ab. Temperature-dependent magnetization for (c) B⊥ab and (d) B‖ab.

Since $CrI_3$ is an intrinsic semiconductor[105, 89], we expect conduction to occur primarily via tunneling in thin samples. We have measured the resistance-area product at room temperature and low bias ($V_{AC} = 4$ mV) for several such devices consisting of different $CrI_3$ thicknesses and the results are plotted in Figure 4.3 a. The resistance initially increases exponentially with thickness, indicative of quantum tunneling across the $CrI_3$ layers. Most of the following data were taken from the 10-layer-thick sample, although similar features were also seen in other thicknesses (8 layers and 14 layers). The temperature dependence of the low-bias resistance follows Arrhenius behavior down to $\sim 160$ K, yielding a band gap

of 322 meV, below which the current becomes too small to measure with our instruments (Figure 4.4). In Figure 4.3 b, we show full current–voltage characteristics as a function of temperature. Current increases nonlinearly with increasing bias, as expected for a tunnel junction[106]. Overall, the effect of increasing temperature is to lower the voltage needed to achieve a certain current level.

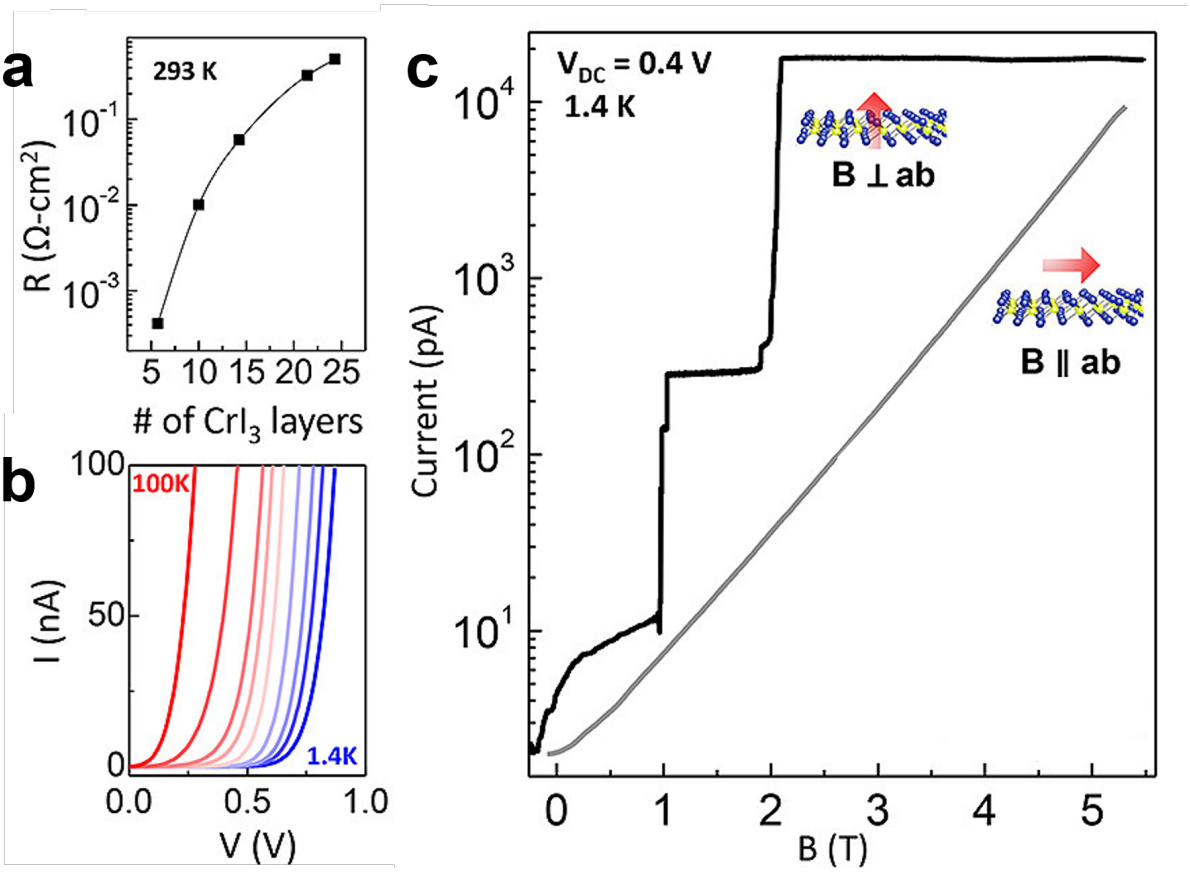


Figure 4.3: Quantum tunneling across the $CrI_3$ layers. (a) A reanormalized junction resistance vs $CrI_3$ thickness at 293 K. (b) Current vs voltage at different temperatures (100, 80, 70, 60, 50, 40, 30, 20, and 1.4 K in sequence from left) of a 10-layer $CrI_3$ junction. (c) Current vs magnetic field at 0.4 V at 1.4 K.

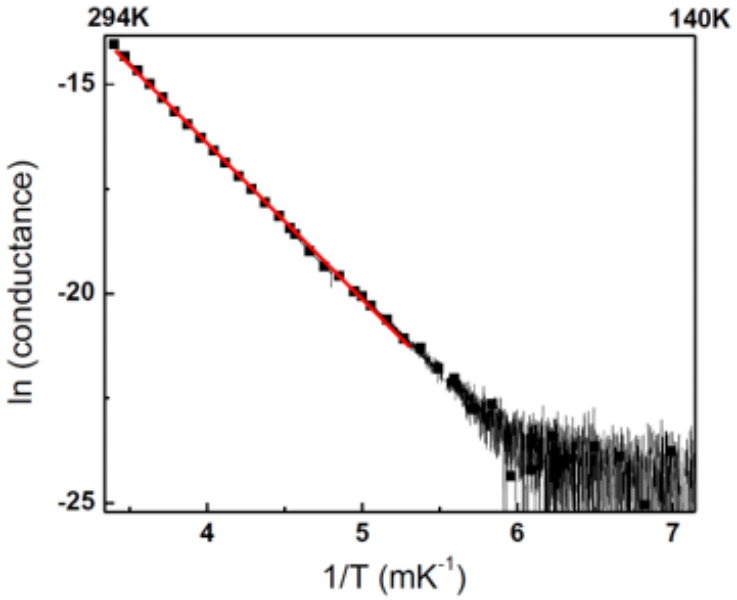


Figure 4.4: ln(conductance) vs. 1/T of 21-layer $CrI_3$ device measured by lock-in with $V_{AC}$ = 4 mV, 17 Hz excitation. The conductance follows an Arrhenius trend from 294 K to 160 K, with gap 322 meV.

The current rises dramatically under a magnetic field at low temperature. In the Figure 4.3 c, we show current as a function of field applied both perpendicular and parallel to the $CrI_3$ layers. For the former, current rises in discrete steps and at $\sim$ 2 T saturates to a value over 4 orders of magnitude larger than that at zero field, while for the latter it increases continuously without saturation up to 5.5 T. This change is remarkable and is the central finding of this work.

Defining the magnetoresistance percentage at constant voltage to be $MR(\%) = \frac{I(B)-I_{min}}{I_{min}} \times 100\%$[93], we find that the effect is 4 orders of magnitude larger than giant magnetoresistance (GMR) observed in Co/Cu magnetic multilayers[107] and on par with CMR in the mixed-valence manganites[108, 30]. Due to the nonlinearity of current–voltage characteristics, MR changes as a function of applied voltage bias. At the bias voltage where MR is maximum, the minimum current measured close to zero field is typically several pA in our

devices, higher than both the noise and zero current level of our instrument. To check this, we measured current at several different voltages, and the results for the 8-layer device are shown below in Figure 4.5 a. At 0.31 V, where MR reaches nearly $10^6$% (Figure 4.5 b), $I_{min}$ is well-defined at $\sim$ 5.5 pA.

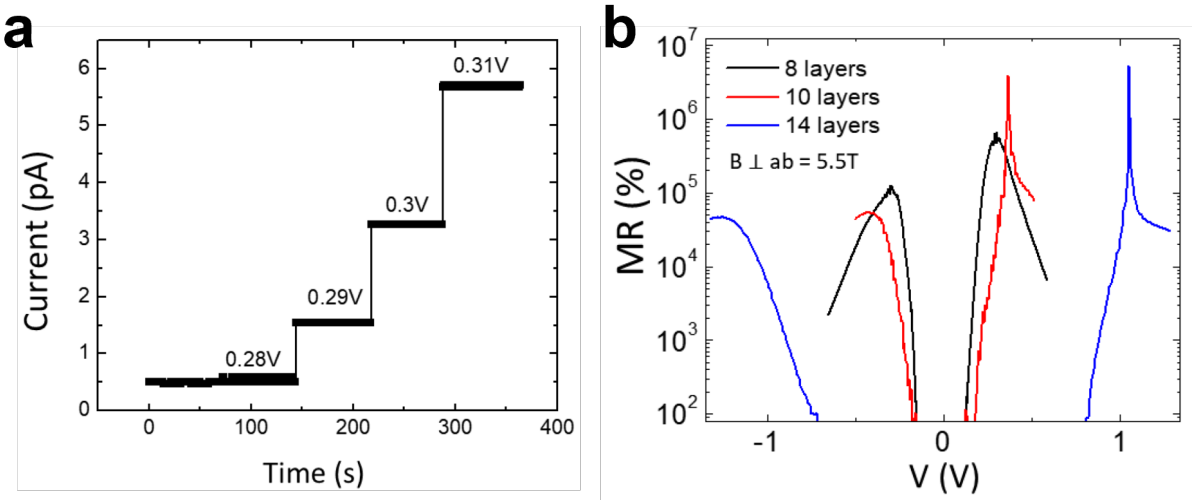


Figure 4.5: Tunneling magnetoresistance of few-layer $CrI_3$. (a) Accuracy of small current measurements of 8-layer $CrI_3$ device at 1.4 K. (b) MR at 5.5 T versus voltage for the three $CrI_3$ devices. The non-monotonic behavior can be understood as follows. At low bias, both I(5.5 T) and $I_{min}$ are below the noise level. Increasing voltage, I(5.5 T) increases above the noise while $I_{min}$ remains at the noise level, giving increasing MR. When both currents exceed the noise, MR decreases with voltage as expected for Fowler-Nordheim tunneling (see discussion below).

In Figure 4.5 b, we show the nonmonotonic dependence of MR on applied voltage for 8-, 10- and 14-layer-thick $CrI_3$. We see that over a broad range, the MR exceeds $10^4$%. In a narrower voltage range, the MR almost reaches $10^6$%. There is also noticeable asymmetry between positive and negative voltage. While we are unclear as to the nature of this effect, we note that there is an inherent asymmetry built into the device geometry as the top and

bottom graphite layers are not identical.

## 4.2 Origin of the Large Magnetoresistance Effect

Our remaining discussion is focused on understanding the origin of this very large magnetoresistance effect as well as its implications on the nature of magnetism in 2D $CrI_3$.

We first measured the current–voltage dependence under different magnetic fields at low temperature, and the results are plotted in the main panels of Figure 4.6 a and b, for perpendicular and parallel field configurations, respectively. We observe that, similar to increasing temperature, in both cases increasing field lowers the voltage necessary to achieve a given current level. The large rise in current thus results from this shift in conjunction with the highly nonlinear current–voltage characteristics of the junction. The difference between the two field orientations is captured in the insets, which show the measured voltage at 100 nA current as a function of field intensity. The voltage decreases discretely (continuously) for perpendicular (parallel) field, consistent with the results of Figure 4.3 c. We note that due to the device nonlinearity, the very large MR values can only be achieved under constant voltage (and not constant current) biasing conditions.

We have performed similar measurements at different temperatures and the results are shown in Figure 4.6 c (perpendicular field) and d (parallel field). At zero field, the temperature-dependent voltage measured for 100 nA current exhibits a marked kink at $T^* \sim 46$ K, below which it rises more steeply. We have observed this kink in other devices as well consisting of 14 and 20 $CrI_3$ layers—the kink temperature increases slightly with thickness (Figure 4.7).

This trend is consistent with the theoretically predicted 3D-to-2D transition for Curie temperature in Ising model, as mentioned in Section 1.2. As discussed later, we assign this temperature to be the onset of in-plane ferromagnetism in thin $CrI_3$, above which the sample behaves as an isotropic spin paramagnet. For the junction device, applying field suppresses the voltage, with the largest effect seen at low temperature. This change

gradually disappears above $T^*$ for either field direction. The very large negative magnetoresistance observed is thus intimately tied to the formation of the 2D magnetic state.

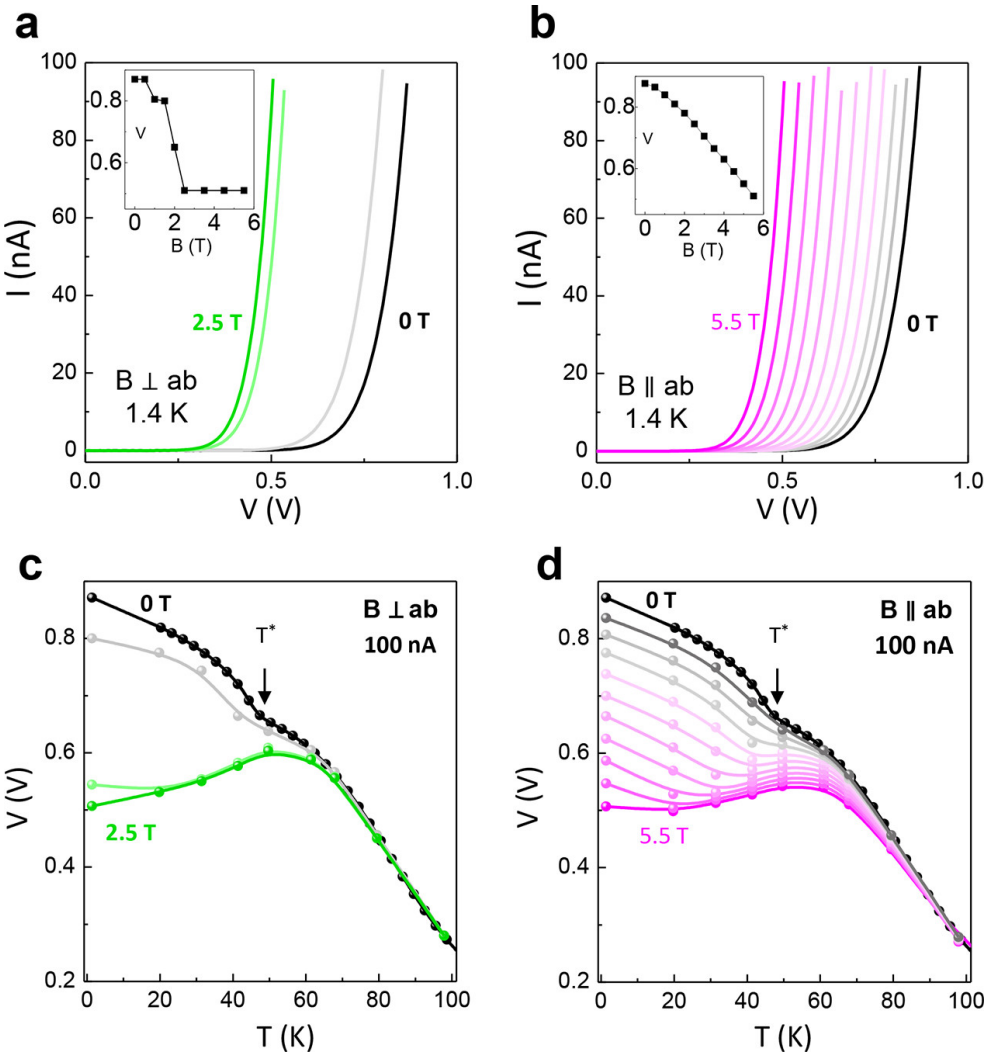


Figure 4.6: Field- and temperature-dependent transport measurements. (a) Current vs voltage at 1.4 K for different B⊥ab (0, 1, 2, and 2.5 T, in sequence from right) (b) Same for B∥ab (from right: 0 and 1 T to 5.5 T with 0.5 T steps). Insets show voltage vs B for the two field orientations at 100 nA. (c) Temperature-dependent voltage (left axis) for same B⊥ab above. (d) Same for B∥ab.

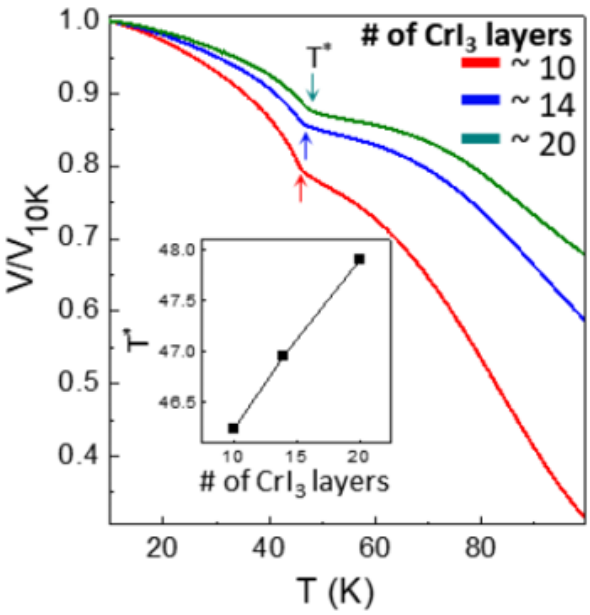


Figure 4.7: Normalized voltage vs. temperature plot of three $CrI_3$ devices taken at zero field and 100 nA current biasing. Inset shows $T^*$ vs. thickness.

## 4.3 Magnetic Anisotropy of Few-Layer $CrI_3$

The key to understanding this phase lies in the field anisotropy of magnetoresistance. In the main panels of Figure 4.8 a and b, we show slow (0.2 T/min) field sweeps of voltage taken at different temperatures for perpendicular and parallel field orientations, respectively. At low temperature, the former shows a series of abrupt jumps at low field as well as marked hysteresis between different sweep directions. The effect of hysteresis is highlighted in the inset of Figure 4.8 a, which shows a zoom-in of the 1.4 K data around zero field. We also observed similar effects in other samples, and the jumps in 14-layer $CrI_3$ device are highlighted in the main panel of Figure 4.8 c. Above $\sim$ 2 T, the voltage saturates to a field independent value of $\sim$ 0.5 V. As the temperature is increased above $T^*$, both the hysteresis and the jumps disappear, while the magnetoresistance decreases substantially.

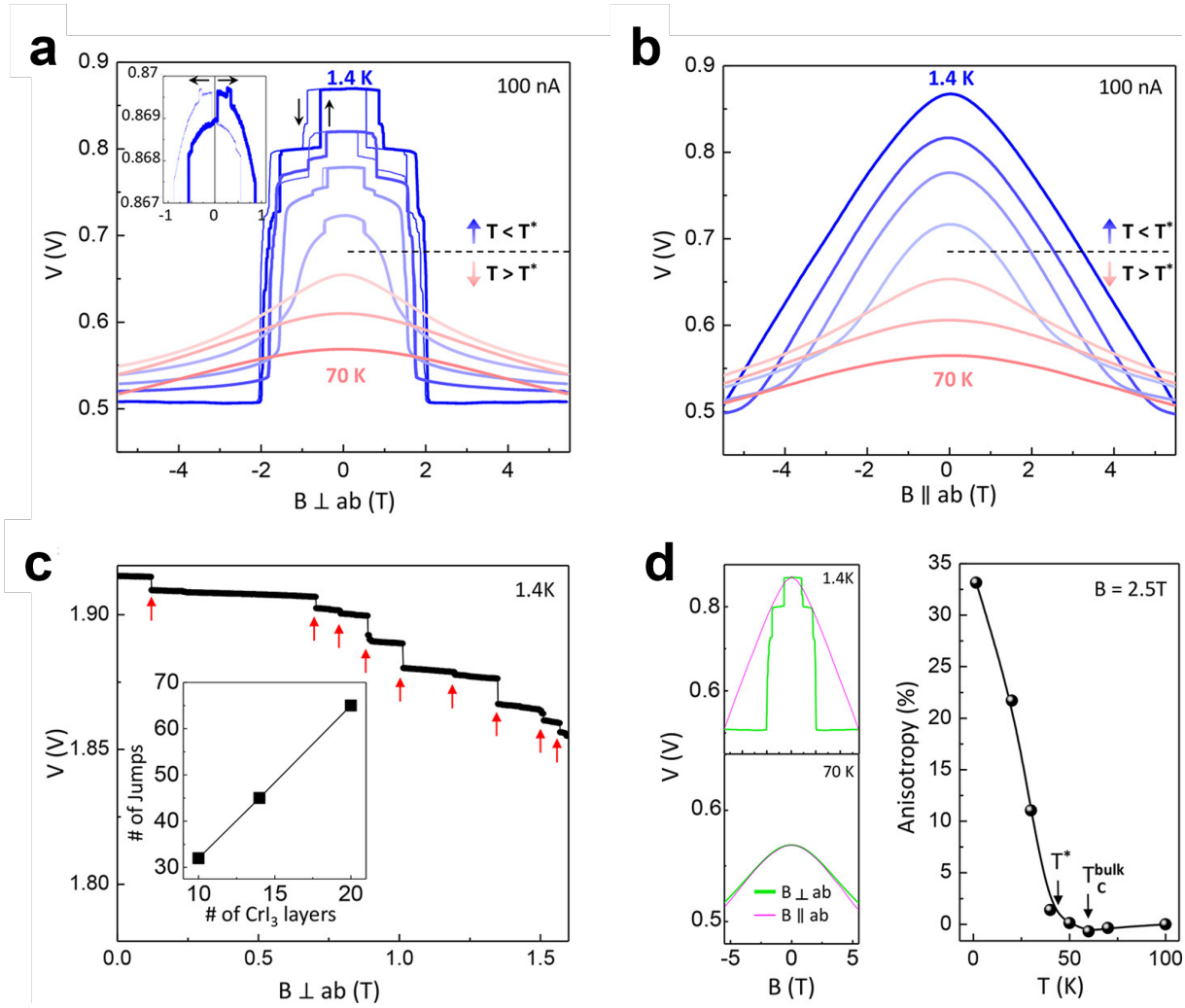


Figure 4.8: Magnetoresistance anisotropy and domain flipping in thin $CrI_3$. (a) Voltage vs B⊥ab sweep for 10-layer $CrI_3$ device at different temperatures (1.4, 20, 30, 40, 50, 60, and 70 K, in sequence from top); (b) Same for B∥ab. Inset in part a shows zoom-in of 1.4 K data. (c) V vs B⊥ab showing many abrupt jumps for 14-layer $CrI_3$ device indicated by red arrows. Insets shows the total number of jumps vs the number of $CrI_3$ layers. (d) Left: comparison of V vs B sweeps at 100 nA for two field orientations at two different temperature conditions (1.4 and 70 K). Right: magnetoresistance anisotropy at 2.5 T vs temperature.

For a given temperature, the overall magnetoresistance change for parallel field is qualitatively similar, except hysteresis and abrupt jumps are never observed. Furthermore, at low temperature, the necessary field in order to achieve the same voltage change is significantly higher ($\sim$ 5.5 T for $\sim$ 0.5 V at 1.4 K). Compared with perpendicular field, the larger saturation field in ab plane displays a rather large magnetic anisotropy in ultrathin $CrI_3$ below $T^*$.

Interestingly, the two voltage curves become nearly identical at high temperature, as evident from the left panel of Figure 4.8 d. In the right panel, we have plotted the temperature-dependent magnetoresistance anisotropy, defined by $\frac{V(B_\parallel)-V(B_\perp)}{(V(B_\parallel)+V(B_\perp))/2} \times 100\%$, evaluated at 100 nA current and 2.5 T field. The anisotropy is nearly zero above $T^*$ and increases considerably below. Taken together, the results from Figure 4.8 indicate that thin $CrI_3$ behaves as an isotropic paramagnet above this critical temperature.

## 4.4 Spin-Filtering Model

The hysteresis and jumps observed below $T^*$ for perpendicular field are suggestive of domain flips analogous to the Barkhausen effect[109]. Indeed, magneto-optical measurements by Zhong et al. on $CrI_3$ flakes of comparable thickness report complex domain dynamics within a similar field range[110]. One possibility is that the different layers are coupled ferromagnetically and all flip spin within a given domain. In this case, lateral transport may be very sensitive to spin flip scattering at the domain walls. Since we measure vertical transport across the $CrI_3$ layers, however, we expect magnetoresistance from this change to be small. Alternatively, it is possible for the spins to flip layer by layer[111]. The resistance of such as state would thus depend sensitively on the relative spin orientation of adjacent layers[93, 107]. We have measured the number of jumps for junctions with different $CrI_3$ thickness, and we observe a larger number of jumps for thicker samples (see Figure 4.8 c, inset), which would further substantiate the latter scenario.

We thus propose the following model to account for the very large tunnel magnetoresis-

tance observed in our devices at low temperature, which is shown schematically in Figure 4.9 a–c. In the paramagnetic phase above $T^*$, carriers encounter a spin-degenerate tunnel barrier, $\Phi_{PM}$ (dotted black line in Figure 4.9 c), from semiconducting $CrI_3$. Below $T^*$, the spins on each layer $CrI_3$ layer spontaneously polarize along the out-of-plane (easy axis) direction. In contrast with bulk crystals, thin $CrI_3$ exhibits antiferromagnetic (AFM) coupling between layers in the absence of field, yielding net zero moment. Such a state has been observed previously for bilayer samples[20, 112]. The result is a spin modulated tunnel barrier, whose relatively large, effective barrier height, $\Phi_{AFM}$, is marked by the dotted blue line in Figure 4.9 c.

Under a perpendicular field, the spins flip layer by layer, causing jumps in the magnetoresistance until an interlayer ferromagnetic (FM) state is reached at $\sim 2$ T. We note that this field is larger than the saturation field in bulk $CrI_3$, possibility due to different interlayer magnetic interactions in the two systems. The FM state has a conduction band that is spin-split by the exchange interaction uniformly across all the layers. This spin-filtering state has the smallest tunnel barrier, $\Phi_{FM}$, compared to both the PM and AFM barriers, and so also shows the smallest resistance. It shares similar properties with FM tunnel barriers EuO and EuS under zero-field conditions[103, 113]. Under an in-plane field, the antiparallel spins in the AFM state cant continuously until a fully in-plane polarized state is reached at $\sim 5.5$ T with similarly low resistance.

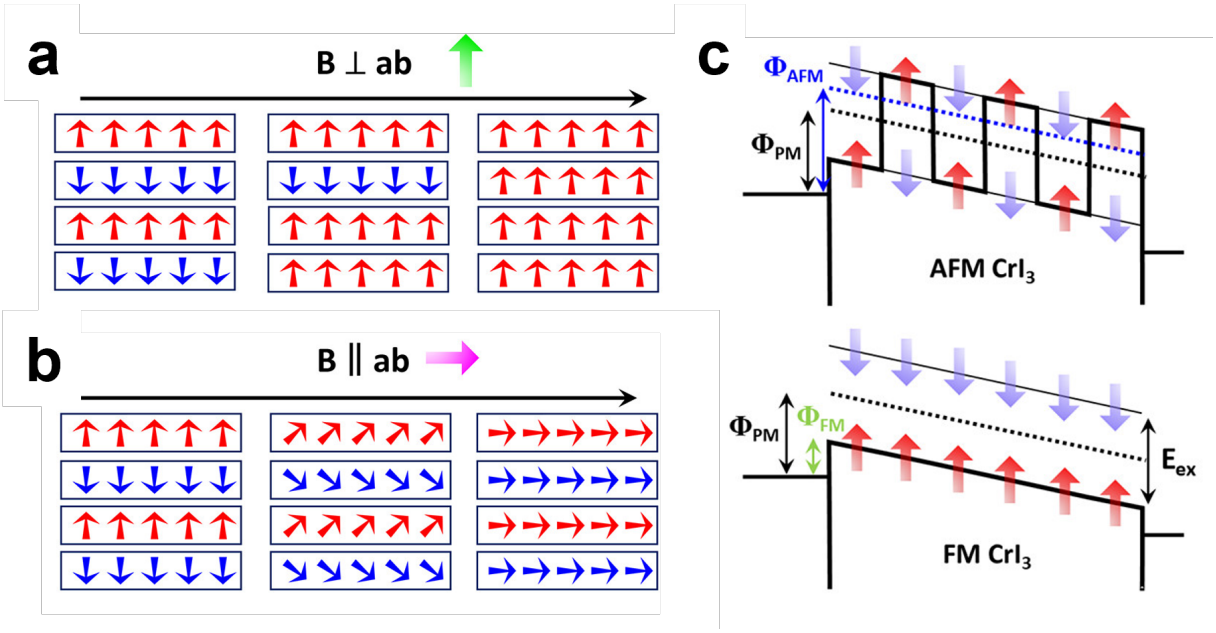


Figure 4.9: Interlayer spin coupling and origin of very large negative magnetoresistance. (a) Proposed transition mechanism from interlayer AFM to FM spin state with B⊥ab and (b) B∥ab. (c) Schematic energy diagrams with AFM barrier (top) and FM barrier (bottom) under Fowler-Nordheim tunneling. PM barrier is shown by black dashed line.

The barrier heights as well as the magnitude of the exchange gap between up and down spins can be approximated by fitting to transport described by Fowler–Nordheim tunneling (Equation 3.2)[113, 114], wherein $\Phi$ is the barrier height between the few-layer graphene injector and $CrI_3$ (averaged over several layers).

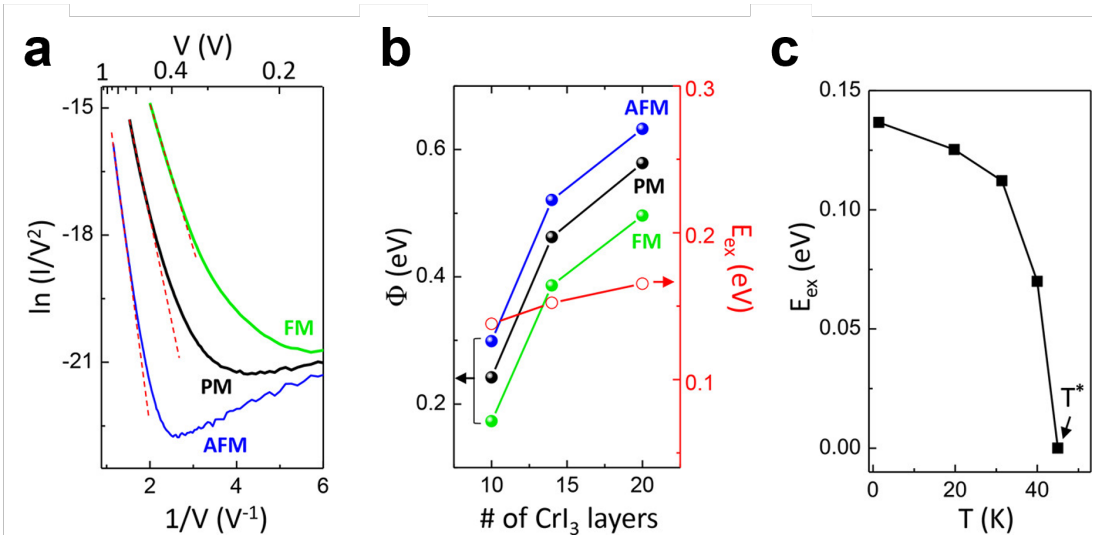


Figure 4.10: Energy barriers and exchange splitting extracted from Fowler–Nordheim tunneling. (a) $\ln \frac{I}{V^2}$ versus $V^{-1}$ plot in three magnetic states and slope (marked by dashed red line) used to extract the height of the tunnel barrier. AFM, PM, and FM states were measured at 0 T at 1.4 K, 0 T at 49 K, and B⊥ab = 2.5 T at 1.4 K, respectively. (b) Thickness dependence of AFM, FM, and PM barrier height values (left axis) and deduced exchange splitting gap (right axis). (c) Exchange gap of 10-layer $CrI_3$ vs temperature.

We have plotted $\ln \frac{I}{V^2}$ vs $V^{-1}$ in Figure 4.10 a and extracted $\Phi$ from the negative linear slope (marked by dashed red line) for the AFM state at zero field (1.4 K), PM state at 49 K (0 T), and FM state at B⊥ab = 2.5 T (1.4 K). $\Phi_{AFM}$ ($\Phi_{FM}$) is larger (smaller) than $\Phi_{PM}$. We then estimate the exchange splitting as $E_{ex} = 2(\Phi_{PM}–\Phi_{FM})$[115]. In Figure 4.10 b, we plotted the different barrier heights and $E_{ex}$ for three devices of different $CrI_3$ thickness. The deduced splitting is comparable to the spin gap value obtained from bandstructure calculations for the conduction band[102, 103, 93], and shows a small decrease with decreasing number of layers, which could explain why $T^*$ is slightly reduced from $T_c^{bulk}$ . We have also measured $\Phi_{FM}$ for several different temperatures, which allows the exchange gap to be determined as a function of temperature. As shown in 4.10 c, $E_{ex}$

decreases sharply when the temperature approaches $T^*$.

# Chapter 5

# Interlayer Magnetism in Few-Layer Chromium Trihalides

Inspired by the results in Chapter 4, we conduct a systematic study on the three chromium trihalides for interlayer magnetism. We find that the interlayer magnetic ordering, exchange gap and magnetic anisotropy evolve systematically with changing halogen atom.

This chapter is based on our published work in *PNAS*[116] with modifications.

## 5.1 Van der Waals Tunnel Junctions

Due to the extreme sensitivity of tunnel magnetoresistance to interlayer magnetic order[117, 96, 104, 118, 119, 115], similar to the design in Figure 4.1, we fabricated graphite/$CrX_3$/graphite tunnel junctions that are fully encapsulated by h-BN for studying the interlayer coupling for three three van der Waals magnetic materials. A schematic illustration and an optical image of our devices are shown in Figure 5.1 a and b, and the detailed fabrication can be found in Section 3.3. In brief, we exfoliated $CrX_3$ within a nitrogen-filled glove box and stacked them between top and bottom graphite electrodes before encapsulation by h-BN on both sides.

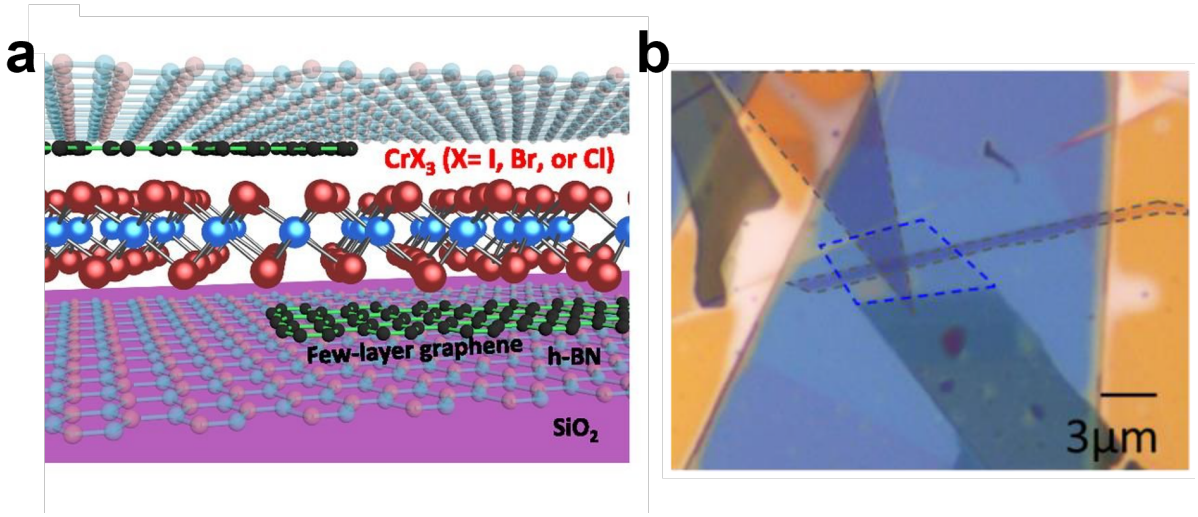


Figure 5.1: Magnetic van der Waals tunnel junction incorporating ultrathin chromium trihalides. (a) Schematic illustration of the device. (b) Optical image of a 2L $CrI_3$ device.

In Figure 5.2, we show nonlinear current-voltage behavior characteristics of few-layer and bilayer $CrX_3$ magnetic tunnel junctions. Bilayer devices exhibit nearly Ohmic behavior in $CrI_3$ and $CrBr_3$, indicating that direct tunneling is dominant rather than Fowler-Nordheim tunneling. Since the bandgap is expected to be large in $CrCl_3$, we could still measure FN tunneling starting from $\sim$ 1 V. Due to this effect, clear spin-filtering can still be observed in 2L $CrCl_3$ devices, but not in 2L $CrI_3$ or 2L $CrBr_3$.

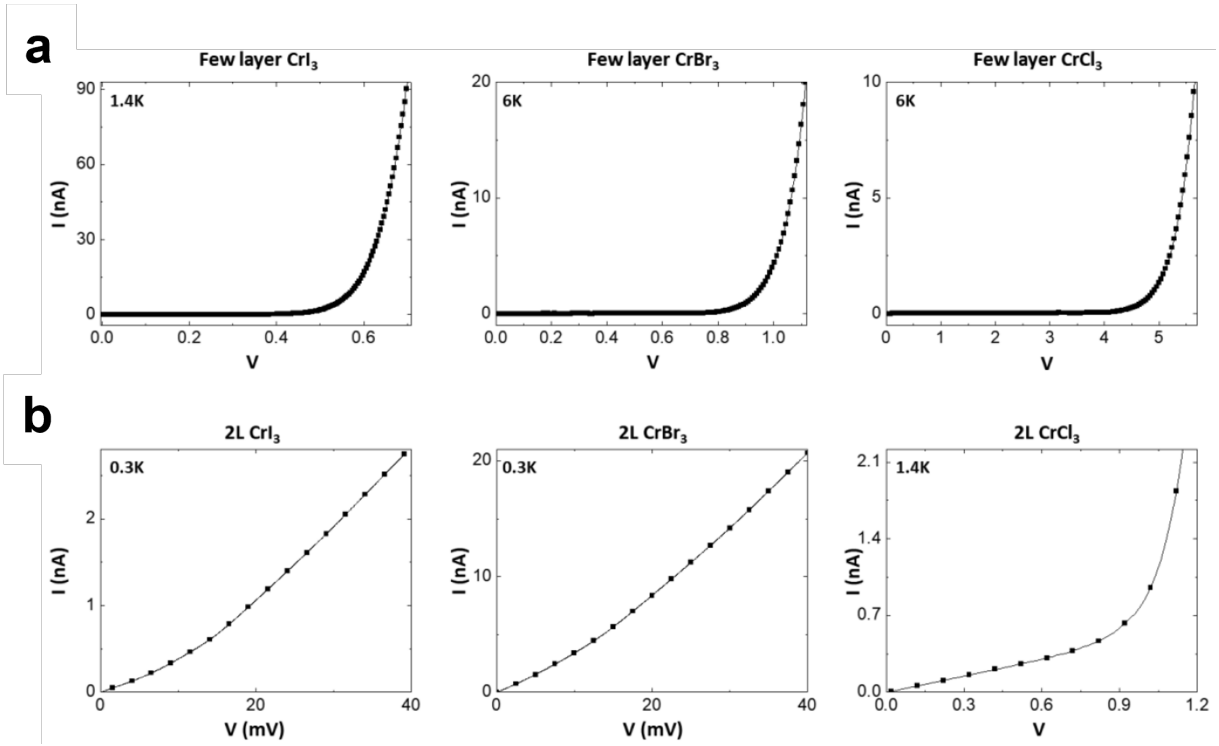


Figure 5.2: Low-temperature I-V measurement of (a) few-layer $CrX_3$ (8L $CrI_3$, 8L $CrBr_3$, and 15L $CrCl_3$) and (b) 2L $CrX_3$.

## 5.2 Interlayer Magnetism

We begin with temperature-dependent transport behavior under zero magnetic field. In Figure 5.2, we show junction resistance vs. temperature upon cooling for three representative devices incorporating the three different trihalides. Their thicknesses measured by atomic force microscopy are $CrI_3$, 5.6 nm; $CrBr_3$, 5.2 nm; and $CrCl_3$, 9 nm. For easy comparison, the resistances have been normalized by their minimum and maximum values and range between 0 and 1. A marked kink is observed in all devices ($CrI_3$, 46 K; $CrBr_3$, 37 K; and $CrCl_3$, 17 K), close to their respective bulk magnetic transition temperatures ($CrI_3$, 61 K[36]; $CrBr_3$, 37 K[52]; and $CrCl_3$, 17 K[53]).

For magnetic tunnel barriers, it has been found that the resistance either decreases or increases abruptly below the critical temperature, depending on whether the magnetic ordering is FM or AFM, respectively[119, 115, 103]. As shown in Chapter 4, this is caused by a spin-filtering effect[119, 93], which effectively lowers (raises) the spin-dependent tunnel barrier upon exchange splitting in the FM (AFM) state. A schematic of this effect is shown in the inset of Figure 5.3. Our devices consist of layered magnetic semiconductors in a vertical transport geometry, and therefore we expect our measurements to be most sensitive to the interlayer magnetic ordering of the few-layer samples. We thus assert that $CrCl_3$ and $CrI_3$ exhibit interlayer AFM coupling in their ground state, while $CrBr_3$ shows interlayer FM coupling. For $CrCl_3$ and $CrBr_3$, this is consistent with measurements of the bulk crystal, while those for $CrI_3$ indicate the opposite (FM coupling)[36].

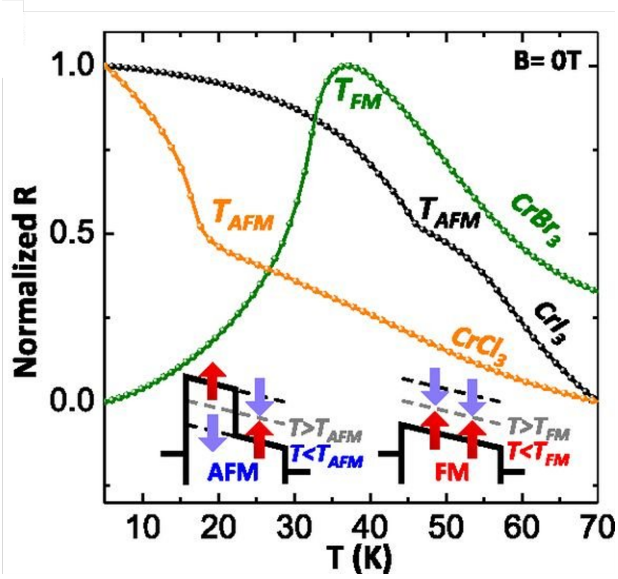


Figure 5.3: Normalized temperature-dependent DC resistance of $CrX_3$ (X = I, Br, and Cl) at constant current of 0.1 nA. Insets show schematics of the spin-dependent tunnel barrier for AFM and FM interlayer coupling. Red and blue arrows indicate spin orientation and are used throughout.

We would like to understand whether the observed interlayer magnetic ordering persists down to the ultimate limit of two atomic layers; however, the resistance kink in the temperature dependence is less apparent for thinner samples, due to a smaller spin-filtering effect.

We therefore turn to the magnetic field dependence. Here, ground-state AFM and FM ordering will yield different magnetoresistance behaviors. In Figure 5.4, we show resistance vs. $B_\perp$ (field perpendicular to the layers) at several different temperatures for the three bilayer (2L) $CrX_3$ devices. In general, the tunneling resistance is smallest when spins in adjacent layers are parallel. First, for 2L $CrI_3$ at low temperature (Figure 5.4 a), the resistance decreases abruptly when the field exceeds $\sim 0.75$ T, indicating a spin-flip transition from the AFM ground state (antiparallel out-of-plane) to a parallel spin state at higher field. This resistance change decreases with increasing temperature until it completely disappears above the magnetic transition temperature. These observations are consistent with previous findings. In comparison, the resistance of 2L $CrCl_3$ also decreases substantially with field (Figure 5.4 c), reflecting that the layers are AFM coupled at zero field. The resistance evolves continuously, however, as spins point in-plane in the ground state and gradually rotate with out-of-plane field. The easy axis of $CrCl_3$ will be characterized and discussed in more detail later. Finally, for 2L $CrBr_3$, the low-temperature resistance is unchanged with field (Figure 5.4 b), since a spin-parallel FM state has naturally formed and states with both layers spin up or down would show no difference in resistance.

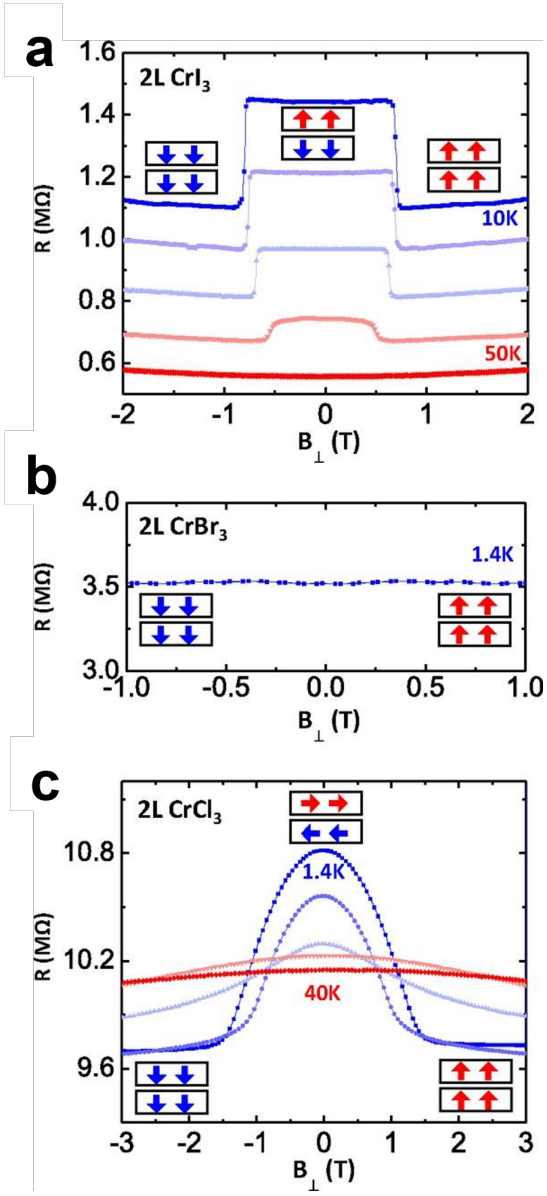


Figure 5.4: Tunneling probe of interlayer magnetic coupling in 2L $CrX_3$. Resistance vs. $B_\perp$ of (a) 2L $CrI_3$ taken at 10, 20, 30, 40, and 50 K, in sequence from blue to red; (b) 2L $CrBr_3$ at 1.4 K; and (c) 2L $CrCl_3$ at 1.4, 10, 20, 30, and 40 K, in sequence from blue to red.

To confirm this scenario, we have further performed magnetic circular dichroism (MCD) measurements[1] on another 2L $CrBr_3$ sample (Figure 5.5). Since the MCD signal is proportional to total out-of-plane magnetization, it can resolve the difference between these two spin states with degenerate resistance. At low temperature, a finite magnetization is observed at zero field with hysteresis between field sweep up or down, corresponding to switching of the total spin direction of the FM coupled layers. In contrast, 2L $CrI_3$ shows no net magnetization at zero field as the layers are AFM coupled[20, 117, 108, 120, 121]. The critical coercive field needed to flip the spin polarization is also much smaller for $CrBr_3$ (10 mT at 5 K).

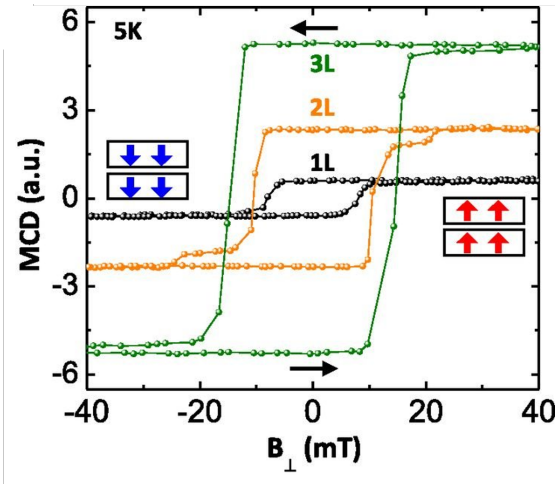


Figure 5.5: Low-temperature MCD vs. $B_\perp$ for 1L, 2L, and 3L $CrBr_3$ at 5K.

[1]The magnetization of h-BN-encapsulated few-layer $CrBr_3$ was characterized by magnetic circular dichroism microscopy in a superconducting magnet He-4 cryostat (AttoDry1000) with out-of-plane magnetic field. A diode laser at 405 nm with an optical power of ~10 $\mu$W was focused onto a submicron spot on the flakes using an objective with numerical aperture 0.8. The optical excitation was modulated by a photoelastic modulator at 50 kHz for left and right circular polarization. The laser reflected from $CrBr_3$ was collected by the same objective and then detected by a photodiode. The MCD signal is defined as the ratio of the modulated signal (measured by a lock-in amplifier) to the total reflected light power (measured by a DC voltmeter).

We have further performed MCD measurements on 1L, 2L and 3L $CrBr_3$ at several different temperatures and observed similar behavior, shown in Figure 5.6. The temperature at which the hysteresis disappears is estimated to be 27, 36, and 37 K for 1L, 2L, and 3L, respectively. Interestingly, this transition temperature is not much decreased down to monolayer, compared to the one for bulk.

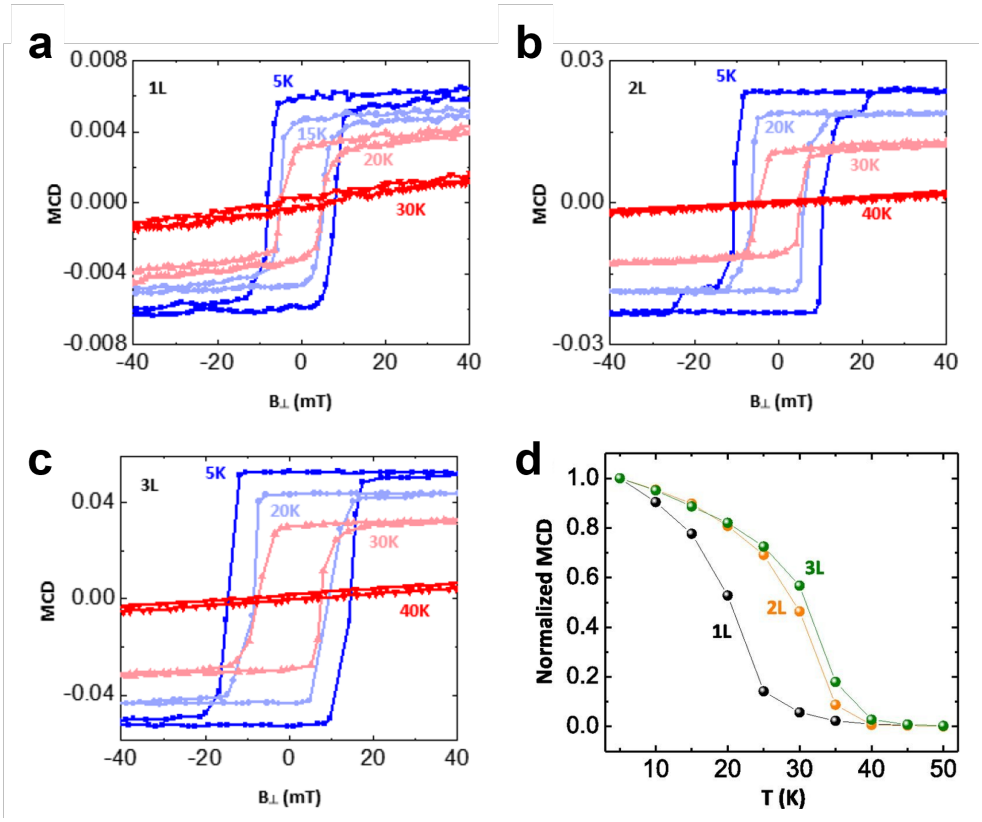


Figure 5.6: MCD measurements on $CrBr_3$ of different thicknesses. (a-c) Magnetic circular dichroism (MCD vs $B_\perp$) measurements on 1L, 2L, and 3L $CrBr_3$. (d) Temperature-dependent normalized MCD at zero field, $MCD_{\uparrow(\downarrow)}(T)/MCD_{\uparrow(\downarrow)}(5K)$, for 1L, 2L, and 3L $CrBr_3$.

## 5.3 In-Plane Magnetic Anisotropy

In addition to interlayer magnetic coupling, we would also like to understand the in-plane magnetic anisotropy of all three 2D compounds in greater detail. We begin with comparing the difference in magnetoresistance behaviors between perpendicular and parallel field configurations for the few-layer devices at low temperature (Figure 5.7 a and c). For $CrI_3$, the critical field needed to fully polarize all of the spins in-plane is 3 times larger than that out-of-plane ($B_{\parallel}^{c} =\sim 6.5$ T $\gg B_{\perp}^{c} =\sim 2$ T). In contrast, the out-of-plane critical field is slightly larger in $CrCl_3$ ($B_{\parallel}^{c} =\sim 2$ T $\lessapprox B_{\perp}^{c} =\sim 2.4$ T). For $CrBr_3$, however, magnetic anisotropy cannot be directly determined by magnetoresistance, since interlayer FM coupling results in nearly constant resistance independent of field orientation. Instead, we compared the MCD response of few-layer $CrBr_3$ for out-of-plane and in-plane field and obtained $B_{\parallel}^{c} =\sim 0.44$ T $\gg B_{\perp}^{c} =\sim 0.004$ T (Figure 5.7 b). The layer dependence of the critical fields is summarized in Figure 5.8. These results clearly indicate that the magnetic anisotropy changes with changing halogen atom.

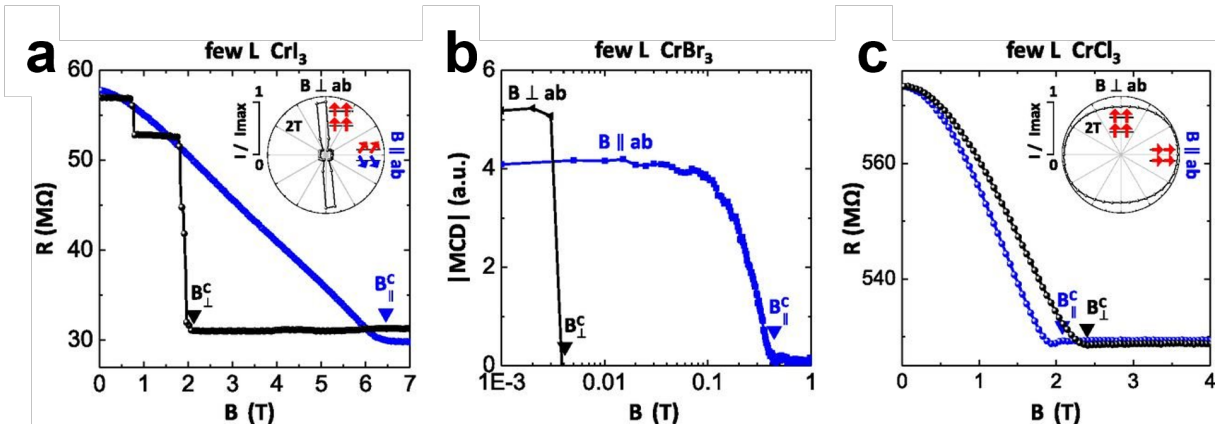


Figure 5.7: Magnetic anisotropy in few-layer $CrX_3$. Comparison of magnetoresistance (1 nA current biasing at 1.4 K) of (a) 8L $CrI_3$ and (c) 15L $CrCl_3$ for perpendicular and parallel magnetic field directions. (b) |MCD| vs. B of 3L $CrBr_3$ at 1.6 K for the two field directions. Insets in (a) and (c) show angle-dependent, normalized tunneling current (voltage biasing, 0.5 V for $CrI_3$, and 5.7 V for $CrCl_3$) at 2 T.

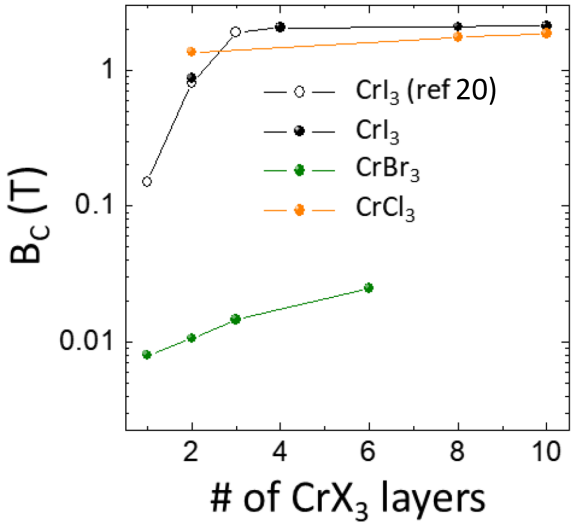


Figure 5.8: Critical field ($B_C$) of $CrX_3$ as a function of the number of layers along with easy axis. $CrI_3$ and $CrBr_3$ were measured with perpendicular field and $CrCl_3$ was measured with parallel field. It is noted that critical fields for $CrI_3$ and $CrCl_3$ above 2L show relatively higher values due to the interlayer AFM coupling.

We have further measured the full angular dependence of the tunneling current at 2 T for few-layer $CrI_3$ and $CrCl_3$ (Figure 5.7, inset). The results show that $CrI_3$ exhibits the behavior of a highly anisotropic, Ising-type spin system with out-of-plane easy axis. A 2 T field applied closely perpendicular to the layers fully polarizes the spins to establish a more conductive state, while the same field applied in-plane only slightly cants the spins to establish a small parallel component. While the easy axis of $CrBr_3$ is also out-of-plane, the system shows reduced anisotropy in comparison and is closer to Heisenberg. Finally, the easy axis of $CrCl_3$ is in-plane with small anisotropy—it requires a slightly smaller field to rotate the spins within the plane than it does to fully cant them perpendicular, which suggests a weak XY spin model.

## 5.4 Exchange Splitting

With the understanding of interlayer coupling, we have measured the low-temperature, exchange gap splitting of the band structure $E_{ex}$ in few-layer samples.

In the top panel of Figure 5.9 a, we show how to deduce the exchange energy gap from the current-voltage characteristics. As described in Chapter 4, the spin-slitting energy gap ($E_{ex}$) can be approximated by taking barrier height difference between fully polarized (P) state and paramagnetic state (PM), $E_{ex} = 2(\Phi_{PM}–\Phi_P)$. Barrier height is calculated in Fowler-Nordheim regime[114] using the current-voltage relation in Equation 3.2.

In the bottom panel of Figure 5.9 a, we plot representative $\ln(J/E^2)$ versus $E^{-1}$ for a representative 10-layer $CrI_3$ in both the PM state (at 49 K with B=0) and fully polarized state (at 1.4 K with $B_\perp = 5.5$ T). We found that the negative slope proportional to $\Phi^{3/2}$ becomes flatter from PM to fully parallel state. As shown in Figure 5.9, the splitting energies of few-layer $CrX_3$ are estimated to be $CrI_3 \sim 136$ meV, $CrBr_3 \sim 122$ meV, and $CrCl_3 \sim 68$ meV. While these values are slightly smaller than those from bandstructure calculations[105], the trend with changing halogen size is consistent. At the same time, we also observed different initial barrier heights in PM state ($\sim 227$ meV in $CrI_3$, $\sim 538$meV in $CrBr_3$, and $\sim 943$ meV in $CrCl_3$), which is consistent with calculations showing increasing bandgap with decreasing halogen atom size[105]. Among the three $CrX_3$, $CrI_3$ exhibits the largest exchange splitting gap, which can be explained by a stronger intralayer Cr-Cr superexchange.

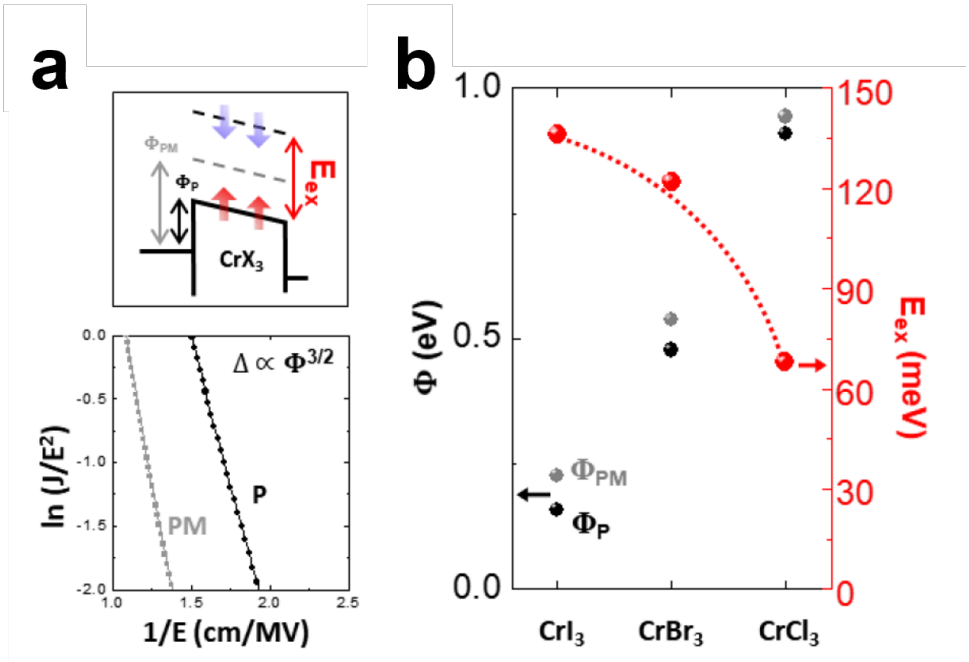


Figure 5.9: Magnetic exchange splitting gap of few-layer $CrX_3$. (a) Top: a schematic illustration of band structure for the calculation of splitting energy gap ($E_{ex} = 2(\Phi_{PM}–\Phi_P)$). Bottom: $\ln(J/E^2)$ versus $E^{-1}$ plot of 10-layer $CrI_3$ at two different conditions (gray: 49 K without field, black: 1.4 K with B $\perp$ ab = 5.5 T). (b) $\Phi_{PM}$ and $\Phi_P$ for 10L $CrI_3$, 10L $CrBr_3$, and 12L $CrCl_3$ and deduced exchange splitting gap at 1.4 K.

# Chapter 6

# Magnetic Excitation in 2D Chromium Trihalides

In Chapter 5, the interalyer couplings for three chromium thihalides have been systematically studied. In this chapter, with the same tunneling structures, we study the magnetic excitations for the three chomium trihalides using inelastic electron tunneling. By fitting to a spin wave theory that accounts for nearest-neighbor exchange interactions, we are able to determine a simple spin Hamiltonian describing all three systems.

This chapter is based on our published work in *PNAS*[116] with modifications.

## 6.1 Microscopic Picture

These observed differences in magnetic properties among the three chromium trihalides in Chapter 5 motivate a detailed microscopic understanding of the spin Hamiltonian for all three 2D systems, which can be extracted through observation of their excitations (magnons) at low junction biases. Toward this end, we have measured the AC conductance ($dI/dV$) vs. DC voltage V of all three 2L devices using standard lock-in methods (Figure

6.1). The conductance abruptly increases when the voltage reaches a magnon energy, due to the opening of an additional inelastic scattering channel[96, 122, 122]. The magnon energies can then be seen as peaks in the $| d^2I/dV^2 |$ spectrum.

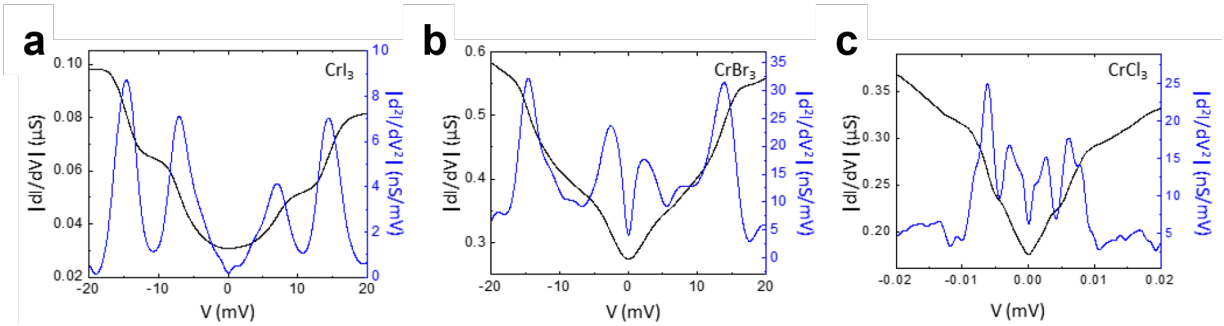


Figure 6.1: IETS for bilayer $CrX_3$ at 2 K. The AC conductance (G, $dI/dV$) vs DC voltage of (a) 2L $CrI_3$, (b) 2L $CrBr_3$, and (c) 2L $CrCl_3$. The derivative $| d^2I/dV^2 |$ is shown in blue solid line. Conductance at each DC voltage is measured with 100 $\mu$V AC excitation voltage.

In Figure 6.2, we show, as a color plot, the evolution of $| d^2I/dV^2 |$ vs. $V$ with magnetic field along the hard axis for all three 2L trihalides, and similar data along the easy axis are shown in Figure 6.3. In each case, at least two magnon modes can be seen dispersing with field. This is consistent with the underlying honeycomb lattice, which gives rise to two magnon energy branches in momentum space[123]. The magnon density is largest at the M point. The observation of additional peaks indicates that we are resolving magnons with different momenta.

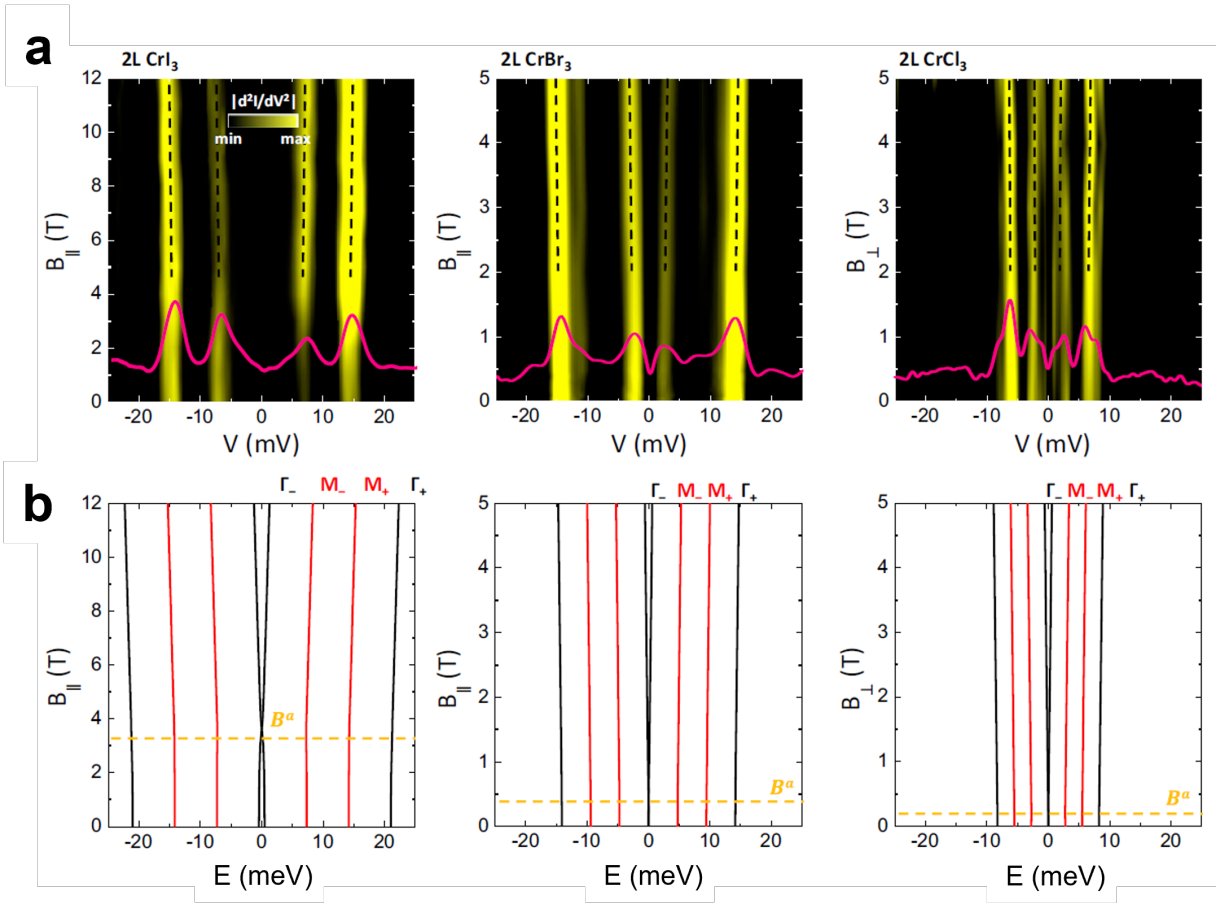


Figure 6.2: Inelastic tunneling spectroscopy of magnons in 2L $CrX_3$ with magnetic field along the hard axis. (a) Field-dependent $| d^2I/dV^2 |$ vs. voltage for 2L $CrX_3$ at 0.3 K and (b) Calculated magnon energies for 1L $CrX_3$ with magnetic field applied along the hard axis. Magnon peaks in a are partially guided by dashed lines.

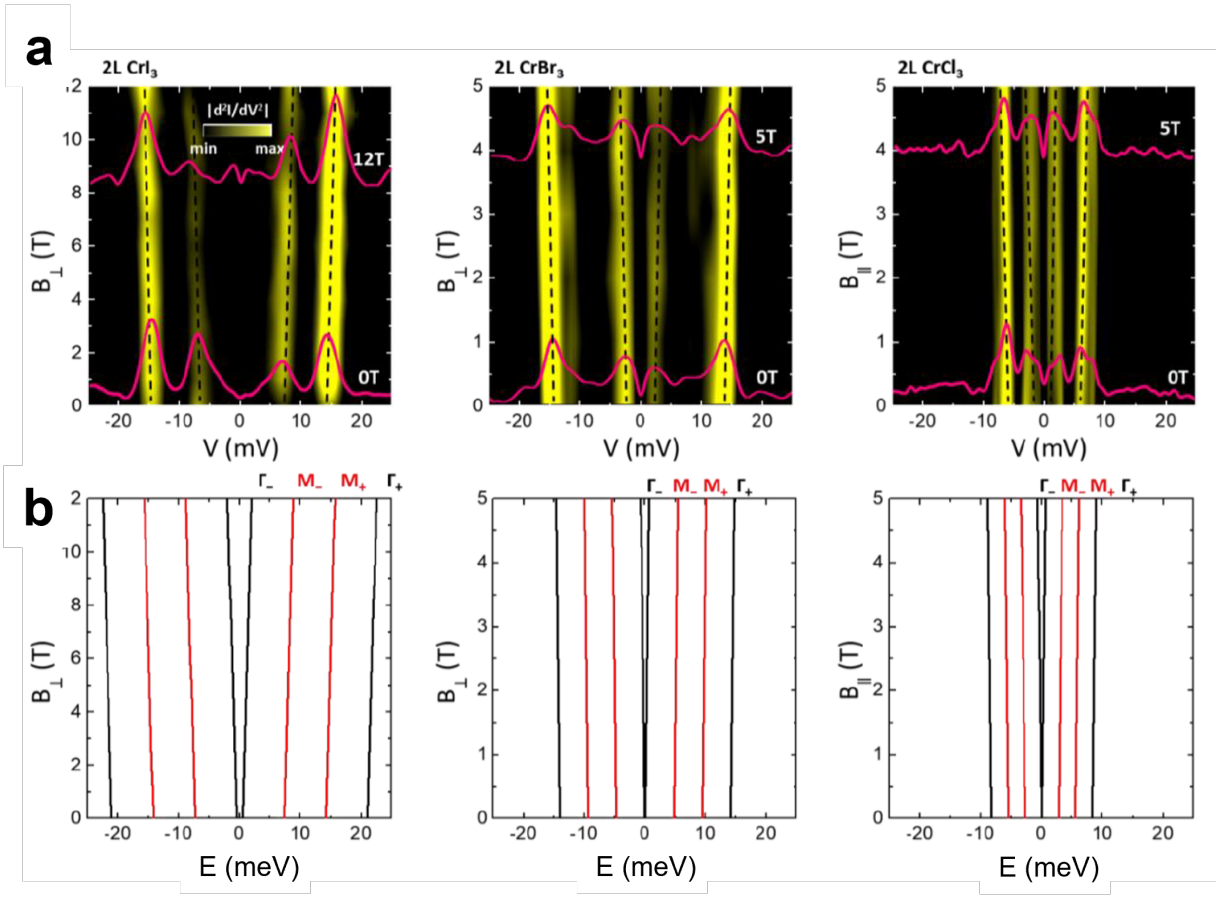


Figure 6.3: Inelastic tunneling spectroscopy of magnons in 2L $CrX_3$ with magnetic field along the easy axis. (a) Field-dependent $| d^2I/dV^2 |$ vs. voltage for 2L $CrX_3$ at 0.3 K and (b) Calculated magnon energies for 1L $CrX_3$ with magnetic field applied along the easy axis. Magnon peaks in a are partially guided by dashed lines.

The observed magnon energies can be largely understood by considering only the intralayer magnetic interaction within a single layer. To estimate the effect of interlayer coupling, we note that the easy axis critical field for both $CrI_3$ and $CrCl_3$ ($\sim$ 2 T for few-layer) decreases substantially with reduced thickness (Figure 5.8). In particular, it is $\sim$ 0.1 T for 1L $CrI_3$[20]. This indicates that 2 T (or 0.2 meV for g factor = 2) is the energy

required to overcome the interlayer AFM coupling for these materials. In contrast, $B_{\perp}^{c}$ maintains a small and nearly thickness-independent value for $CrBr_3$, which shows interlayer FM coupling. This energy scale is an order of magnitude smaller than the observed magnon energies, and so interlayer coupling should only play a perturbative role.

The minimal model to describe ferromagnetism in a single layer of $CrX_3$ is the 2D anisotropic Heisenberg model, described by the Hamiltonian (similar to Equation 2.1)

$$H = -J \sum_{<i,j>} (S_i^x S_i^x + S_i^y S_i^y + \alpha S_i^z S_i^z) \tag{6.1}$$

where $S_{i(j)}^{x(y,z)}$ is the spin operator along the $x(y,z)$ direction at the $Cr^{3+}$ site $i(j)$, $J$ is the exchange coupling constant, $\alpha$ is the exchange anisotropy, and $< i,j >$ denotes the approximation of the nearest-neighbor exchange coupling. By convention, $z$ is chosen as the direction perpendicular to the layers and $J > 0$ for ferromagnetism. The application of a magnetic field contributes an additional Zeeman term $-g\mu_B B \sum_i S_i$ along the same spin direction.

We have performed a full spin wave analysis for monolayer $CrX_3$ based on the above Hamiltonian on the honeycomb lattice (see Section 6.3). The results are shown in Figure 6.2 b and Figure 6.3 b. At zero field, the $\Gamma$ and $M$ point magnons have energies $\Gamma_{\pm} = (9/2)J(\alpha \pm 1)$ and $M_{\pm} = (3/2)J(3\alpha \pm 1)$. For $\alpha$ of order unity, $\Gamma_{-} \approx 0$ and $M_{+} \approx 2M_{-}$, restricting the magnon assignments in our data. For $CrI_3$ and $CrCl_3$, the most intense peaks are $M_{+}$ and $M_{-}$ modes, while the highest energy mode for $CrBr_3$ is assigned to be $\Gamma_{+}$, although $M_{+}$ is also faintly visible for positive voltage. We note that, for $CrI_3$, this magnon assignment is consistent with a recent neutron scattering study of the bulk crystal[124], which shows comparable magnon energies ($\sim 9$ and $\sim 15$ meV) at the M point. At other momenta, it may be important to also consider second and third nearest-neighbor terms in the spin Hamiltonian.

When the field is applied along the easy axis ($B_{\perp}$ for $CrI_3$ and $CrBr_3$, and $B_{\parallel}$ for $CrCl_3$), all magnon energies increase linearly with field with slope $g\mu_B$. We obtain an average $g$ factor of 2.2 between three materials. For field applied in the transverse direction ($B_{\parallel}$ for

$CrI_3$ and $CrBr_3$, and $B_\perp$ for $CrCl_3$), the system undergoes a quantum phase transition as the spins rotate. Here, $\Gamma_+$ and $M_\pm$ modes remain nearly constant up to the anisotropy field, while $\Gamma_-$ gets pushed to zero energy. In Figure 6.2 a, we indeed observe that the $M_\pm$ peak positions for $CrI_3$ do not shift at low fields. To account for the effect of interlayer coupling, we estimate the anisotropy field, $B^a$, for monolayer to be the difference between the critical fields applied along the hard and easy axes for the 2L devices ($B^a = 3.63$ T for $CrI_3$; $B^a = 0.44$ T for $CrBr_3$; and $B^a = 0.23$ T for $CrCl_3$). At high fields, all mode energies again increase by the Zeeman shift. The dashed lines in Figure 6.2 a and Figure 6.3 a guide the eye to see this change. This simple model captures the essential features of the magnon positions and dispersions for all three compounds, indicating that the data can be largely understood by considering only nearest-neighbor interactions within a single layer.

Importantly, our analysis allows us to extract both the exchange energy $J$ and exchange anisotropy $\alpha$ for the 2D trihalides. In Table 6.1, we have summarized these values together with other key properties measured in this work (Chapter 5). The transition temperature $T_c$, $J$, $E_{ex}$, and $\alpha$ all decrease with smaller halogen atom. The evolving anisotropy changes the 2D spin class from Ising ($\alpha > 1$) in $CrI_3$ to anisotropic Heisenberg ($\alpha \gtrapprox 1$) in $CrBr_3$, and to weak XY ($\alpha \lessapprox 1$) in $CrCl_3$. Surprisingly, the transition temperature is not substantially reduced down to 1L for $CrBr_3$ and 2L for $CrCl_3$, despite the low anisotropy in these materials, indicating that strong anisotropy is not necessary to stabilize magnetism in the 2D limit.

| | $CrI_3$ | $CrBr_3$ | $CrCl_3$ |
|---|---|---|---|
| Interlayer magnetic coupling | AFM | FM | AFM |
| $T_c$, K | Few L: 46 (tunneling)<br>2L: 45 (tunneling)<br>1L: 45 (MOKE) | Few L: 37 (tunneling)<br>3L: 37 (MCD)<br>2L: 36 (MCD)<br>1L: 27 (MCD) | Few L: 17 (tunneling)<br>2L: 16 (tunneling) |
| $E_{ex}$, meV | 136 | 122 | 68 |
| $J$, meV | 2.29 | 1.56 | 0.92 |
| $\alpha$ | 1.04(5) | 1.00(8) | 0.99(3) |
| Spin model | Ising | Anisotropic Heisenberg | Weak XY |

Table 6.1: Summary of magnetic properties of 2D $CrX_3$

## 6.2 Discussion

We now end by discussing two interesting implications of these results. First, we notice that the transition temperature for 2L $CrBr_3$ and $CrCl_3$ is already very near that of the bulk crystal, while that for few-layer $CrI_3$ ($\sim 46$ K) is more reduced from the bulk transition temperature of 61 K. It is possible that changing interlayer magnetism from FM to AFM also modifies the transition temperature of this material. In contrast, thin $CrBr_3$ and $CrCl_3$ have similar interlayer coupling with their bulk counterparts. Second, the existence and/or nature of magnetism in monolayer $CrCl_3$ still remains an open question, as the 2D XY model is not expected to show long-range order at finite temperature. It may be possible that interlayer AFM coupling plays a nonnegligible role in stabilizing magnetism in 2Ls, although one cannot strictly rule out other more complex magnetic orders or the importance of additional in-plane exchange interactions beyond the nearest neighbor. Our work here paves the way for future studies on these topics.

## 6.3 Spin Wave Calculations

In the following, we perform calculations of spin wave dispersions under an external magnetic field for monolayer honeycomb magnets $CrX_3$. Our spin Hamiltonian only considers monolayer spin structure instead of the actual bilayer structure, because interlayer interactions are small compared to intralayer exchange interactions. Although bilayer splitting modifies the monolayer spin wave dispersions, it seems unnecessary in evaluating intralayer exchange interactions. We choose the anisotropic Heisenberg spin model below:

$$H = -J \sum_{<i,j>} (S_i^x S_i^x + S_i^y S_i^y + \alpha S_i^z S_i^z) - g\mu_B (B_z \sum_i S_i^z + B_x \sum_i S_i^x) \tag{6.2}$$

where $J$ is the nearest neighbor exchange energy, $i$ and $j$ denote the two inequivalent $Cr^{3+}$ site, and $\alpha$ scales the z-direction exchange strength. In particular, $\alpha$ is greater than, equivalent to, or smaller than 1 for Ising, isotropic Heisenberg, or XY magnets, respectively. $g$ is the $g$-factor for $Cr^{3+}$ magnetic moments, $g\mu_B$ the Bohr magneton, and $\vec{B}$ is external magnetic field. Depending on the experimental geometry, either $B_z$ or $B_x$ is nonzero, representing the magnetic field perpendicular to or parallel to the plane of $CrX_3$ layers.

Without an external magnetic field, the spins in $CrX_3$ align either along the z-axis or in the xy-plane depending on the magnitude of $\alpha$. When an external field is applied perpendicular to the easy axis or easy plane, it tilts the spins off its original direction, to a new direction that minimizes the energy for the Hamiltonian above. To keep it general for all three types of magnets, we characterize the spin orientation by its tilt angle from z axis, $\theta$ For example, $\theta = 0$ corresponds to the spins aligning along the z-axis and $\theta = \pi/2$ spins in the xy-plane. To determine $\theta$ for a given external magnetic field, a rotation transform is applied, where $\vec{\tilde{S}}$ is the spin orientation in the new ground state under the external field:

$$\begin{cases} S^x = \tilde{S}^x \cos(\theta) + \tilde{S}^z \sin(\theta) \\ S^z = -\tilde{S}^x \sin(\theta) + \tilde{S}^z \cos(\theta) \end{cases} \tag{6.3}$$

After applying Holstein-Primakoff transform for both site $i$ and site $j$,

$$\begin{cases} S^z = S - a^\dagger a \\ S^+ = \sqrt{2S}\left(1 - \frac{a^\dagger a}{2S}\right) a \\ S^- = \sqrt{2S} a^\dagger \left(1 - \frac{a^\dagger a}{2S}\right) \end{cases} \tag{6.4}$$

we arrive at the following Hamiltonian where spin wave interactions are ignored:

$$H = H_{const} + H_1 + H_2 \tag{6.5}$$

$$H_{const} = -SN\left(JzS\left(\alpha\cos^2(\theta) + \sin^2(\theta)\right)\right) + 2g\mu_B\left(\sin(\theta)B_x + \cos(\theta)B_z\right) \tag{6.6}$$

$$H_1 = \left(\frac{1}{2}JSz(\alpha-1)\sin(2\theta) + g\mu_B\left(\sin(\theta)B_z - \cos(\theta)B_x\right)\right)\sqrt{S/2}\sum_i\left(a_i^\dagger + a_i\right) \tag{6.7}$$

$$\begin{aligned} H_2 = &-\frac{1}{2}JS\left(\alpha\sin^2(\theta) + \cos^2(\theta) - 1\right)\sum_{<i,j>}\left(a_i^\dagger b_j^\dagger + a_i b_j\right) \\ &-\frac{1}{2}JS\left(\alpha\sin^2(\theta) + \cos^2(\theta) + 1\right)\sum_{<i,j>}\left(a_i^\dagger b_j + a_i b_j^\dagger\right) \\ &+JS(\alpha\cos^2(\theta) + \sin^2)\sum_{<i,j>}\left(a_i^\dagger a_i + b_j b_j^\dagger\right) \\ &+g\mu_B\left(\sin(\theta)B_x + \cos(\theta)B_z\right)\left(\sum_i a_i^\dagger a_i + \sum_j b_j b_j^\dagger\right) \end{aligned} \tag{6.8}$$

where $N$ is the number of sublattices, and $z$ is the number of nearest neighbor spins. Minimizing $H_{const}$ the new spin orientation $\theta$ and eliminates $H_1$ If $\vec{B}$ is parallel to the original spin orientation, the spins remain the same. If $\vec{B}$ is perpendicular, $\theta$ is a function of $\mid \vec{B} \mid$. At low fields,

$$\theta = \arcsin\frac{g\mu_B B_x}{JSz(\alpha-1)}, \quad B_z = 0, \alpha > 1 \tag{6.9}$$

and

$$\theta = \arccos\frac{g\mu_B B_x}{JSz(\alpha-1)}, \quad B_x = 0, \alpha < 1 \tag{6.10}$$

A critical field strength $B_c$ exists above which the spins are completely aligned along the external field direction.

To obtain the spin wave dispersions under external magnetic fields, Fourier and Bogoliubov transforms of spin wave operators are applied to $H_2$. Fourier transform yields

$$H_2 = Q_1 \sum_k \left( a_k^\dagger b_{-k}^\dagger \gamma_{-k} + a_k b_{-k} \gamma_k \right) + Q_2 \sum_k \left( a_k^\dagger b_k \gamma_{-k} + a_k b_k^\dagger \gamma_k \right) + Q_3 \sum_k \left( a_k^\dagger a_k + b_k b_k \right) \tag{6.11}$$

$a_k$ and $b_k$ correspond to the Fourier transformed spin wave operators of real space operators $a_i$ and $b_j$, respectively. Bogoliubov transform for bosonic excitations is then done by

$$\begin{pmatrix} \phi_{-k} \\ \psi_{-k} \\ \phi_k^\dagger \\ \psi_k^\dagger \end{pmatrix} = M \begin{pmatrix} a_{-k} \\ b_{-k} \\ a_k^\dagger \\ b_k^\dagger \end{pmatrix} \tag{6.12}$$

$$M = \begin{pmatrix} \frac{Q_3 - Q_2 P_1 - P_2}{Q_1 \gamma_k} & -\frac{Q_3 - Q_2 P_1 - P_2}{Q_1 P_1} & -\sqrt{\frac{\gamma_{-k}}{\gamma_k}} & 1 \\ \frac{Q_3 + Q_2 P_1 - P_2}{Q_1 \gamma_k} & \frac{Q_3 + Q_2 P_1 - P_2}{Q_1 P_1} & \sqrt{\frac{\gamma_{-k}}{\gamma_k}} & 1 \\ \frac{Q_3 - Q_2 P_1 + P_2}{Q_1 \gamma_k} & -\frac{Q_3 - Q_2 P_1 + P_2}{Q_1 P_1} & -\sqrt{\frac{\gamma_{-k}}{\gamma_k}} & 1 \\ \frac{Q_3 + Q_2 P_1 - P_2}{Q_1 \gamma_k} & \frac{Q_3 + Q_2 P_1 - P_2}{Q_1 P_1} & \sqrt{\frac{\gamma_{-k}}{\gamma_k}} & 1 \end{pmatrix} \tag{6.13}$$

where

$$\begin{aligned} P_1 &= \sqrt{\gamma_k \gamma_{-k}} \\ P_2 &= \sqrt{Q_3^2 - 2 Q_3 Q_2 P_1 + (Q_2^2 - Q_1^2) P_1^2} \\ P_3 &= \sqrt{Q_3^2 + 2 Q_3 Q_2 P_1 + (Q_2^2 - Q_1^2) P_1^2} \end{aligned} \tag{6.14}$$

$M$ is the Bogoliubov transform matrix under which the new operators $\phi_k$ and $\psi_k$ satisfy bosonic commutation relations (up to a normalization factor). Spin wave dispersions as a function of external field strength are obtained as $E_1 = P_2$, and $E_2 = P_3$. If $\vec{B}$ is parallel to the original spin orientation, spin wave energies increase by $g\mu_B|\vec{B}|$. If $\vec{B}$ is perpendicular, spin wave energies show an anomaly at $B_c$, as shown in Figure 6.2.

For $Cr^{3+}$, the spin moment has $S$=3/2. In the honeycomb lattice, the number of nearest neighbors is $z = 3$. At large fields, the spin wave energies increase by $g\mu_B B$. $g$-actor is

then extracted from the slope of the spin wave energies as a function of external field. $g$ is taken to be 2.1788, which is the average of the slopes of all three compounds. The spin wave density of states is high at $\Gamma$ and $M$ point, so that the experimentally observed peaks are related with two $\Gamma$-point excitations and two $M$-point excitations. We use the transition fields $B_c$ from the field dependent tunneling spectroscopy data to find a relation between $J$ and $\alpha$, and identify their values fitting the calculated functional forms to the experimental results.

# Chapter 7

# Thickness-Dependent Magnetic Excitation in $\alpha$-$RuCl_3$

In this chapter, we shift our focus to another van der Waals magnetic material, $\alpha$-$RuCl_3$, which possesses more complicated magnetic interactions: Kitaev interaction. The significant Kitaev interaction makes $\alpha$-$RuCl_3$ a promising candidate to realize Kitaev physics[125, 68, 126]. However, intensive study of 2D magnetism of $\alpha$-$RuCl_3$ is still lacking. To study its exotic intralayer magnetism, IETS, which have been proved to be sensitive to magnon behaviors, is permformed.

As discussed in Chapter 2, while evidence of this exotic state has been reported under a modest in-plane magnetic field, such behavior is largely inconsistent with theoretical expectations of Kitaev phases emerging only in out-of-plane fields. These predicted field-induced states have been mostly out of reach due to the strong easy-plane anisotropy of bulk crystals, however. We use a combination of tunneling spectroscopy, magnetotransport, electron diffraction, and *ab initio* calculations to study the layer-dependent magnons, anisotropy, structure, and exchange coupling in atomically thin samples. Due to structural distortions, the sign of the average off-diagonal exchange changes in monolayer $\alpha$-$RuCl_3$, leading to a reversal of magnetic anisotropy to easy-axis. Our work provides a new avenue

to tune the magnetic interactions in $\alpha$-$RuCl_3$ and allows theoretically predicted quantum spin liquid phases for out-of-plane fields to be more experimentally accessible. This chapter is based on our paper currently under revision in *Nature Materials* with modifications.

## 7.1 Finding Monolayer $\alpha$-$RuCl_3$

We start by exfoliating $\alpha$-$RuCl_3$ crystals on oxidized silicon wafers within a nitrogen-filled glovebox and identifying their thickness by optical reflection contrast. Unlike chromium trihalides, the color contrast for monolayer and few-layer $\alpha$-$RuCl_3$ is rather low. To confirm that the thinnest flakes are indeed monolayers, we pick up these samples, encapsulate them with monolayer graphene, and transfer them to 10-nm-thick silicon nitride membranes for 3D electron diffraction measurements (a type of transmission electron microscopy)[1]. Figure 7.1 a shows an electron diffraction pattern of such a structure. Some of the fundamental Bragg peaks of $\alpha$-$RuCl_3$ used for determining the monolayer structure are circled, although the graphene peaks (along the thick gray circle) can be seen as well. Measuring relative to the graphene peaks, the in-plane lattice constant of our exfoliated $\alpha$-$RuCl_3$ is determined to be 5.9981 – 6.0088 Å, which is consistent with the value for the bulk crystal and thus indicates negligible overall strain[68, 127, 128].

By tilting the sample, our collaborators can measure the diffraction spots as a function of out-of-plane crystal momentum ($k_z$). A sideview schematic of the Bragg rod structure

[1] Acquiring 3D electron diffraction patterns was accomplished by tilting the specimen over a range of angles relative to the incident beam to provide slices through the reciprocal structure. Selected area electron diffraction (SAED) patterns were acquired on the TFS Talos F200X G2 operating at 80 keV with TEM holder tilting the sample from +35° to -35° in 1° increment. An accelerating voltage of 80 keV was chosen to minimize beam induced damage to the 2D material. A 0.75 $\mu$m SAED aperture was centered over the same sample region throughout the tilt series acquisition. Each SAED in the tilt series is first background subtracted and aligned to a common center. Diffraction spots pertaining to $\alpha$-$RuCl_3$ at every specimen tilt were characterized by fitting a four-parameter two-dimensional Gaussian to a windowed region about each peak. The integrated diffraction peak intensity was then calculated and plotted against $k_z$ for curve fitting with the kinematic model.

for several of the 1L $\alpha$-$RuCl_3$ peaks is shown in Figure 7.1 b and the experimental Bragg rod intensities are shown in Figure 7.1 c as discrete points together with their expected values in solid lines. In particular, the $(1\bar{2}10)$ and $(\bar{1}2\bar{1}0)$ peaks exhibit a reduction of symmetry from the ideal crystal. As the $k_z$ dependence for 2L and 3L crystals are markedly different (see Figure 7.2, calculated by our collaborators), we can confirm our ability to exfoliate and encapsulate $\alpha$-$RuCl_3$ crystals down to monolayer thickness.

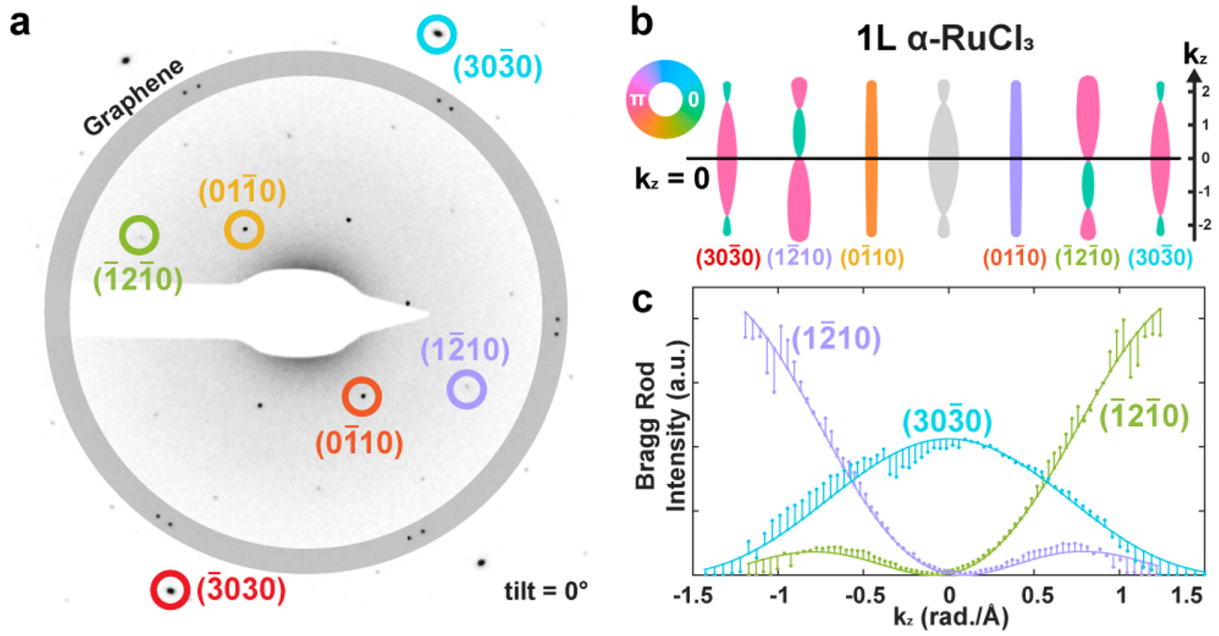


Figure 7.1: 3D electron diffraction on measurements on 1L $\alpha$-$RuCl_3$. (a) Electron diffraction pattern for graphene-encapsulated 1L $\alpha$-$RuCl_3$ at 0° tilt. Bragg peaks for graphene layers are marked by a thick gray circle. Several $\alpha$-$RuCl_3$ Bragg peaks selected for analysis are circled. (b) Schematic of calculated out-of-plane momentum ($k_z$) dependence for the various Bragg rods of 1L $\alpha$-$RuCl_3$ chosen in (a). The thickness and color indicate the complex magnitude and phase of the structure factor, respectively. (c) Experimental Bragg intensities (scatter points) for $(1\bar{2}10)$, $(\bar{1}2\bar{1}0)$, and $(30\bar{3}0)$ peaks, plotted as function of $k_z$, show great agreement with fitted kinematic model (lines) of 1L $\alpha$-$RuCl_3$.

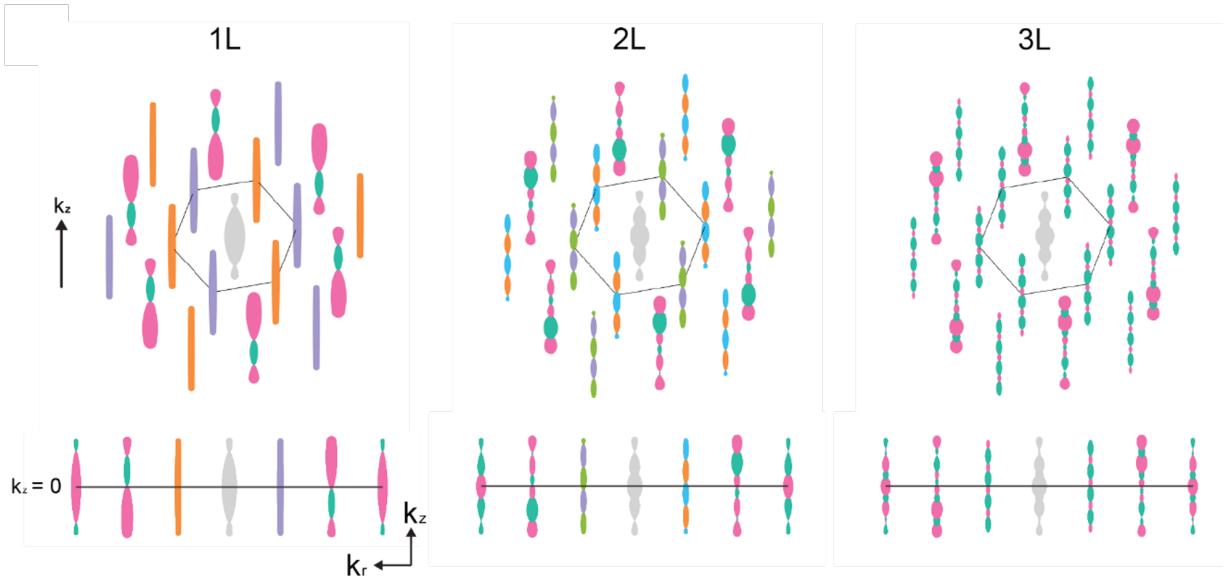


Figure 7.2: 3D reciprocal structure of 1L, 2L, 3L $\alpha$-$RuCl_3$. Bragg rods occupying the reciprocal space of $\alpha$-$RuCl_3$ are illustrated for the first two orders. Bottom panel shows Bragg rods up to the third order in side view. Thickness and color of Bragg rods represent the complex amplitude and phase respectively.

## 7.2 Inelastic Electron Tunneling Spectroscopy

It has been demonstrated that IETS is a powerful tool to probe for spin waves in ultrathin insulating magnets in the $\sim$ 1-10 meV range[96, 116, 122], the same energy window where various magnetic excitations have been observed in bulk $\alpha$-$RuCl_3$[71, 72, 128, 129, 73, 130, 74, 77, 76, 131, 132, 133, 76, 134, 135, 136]. We thus fabricate a series of metal/$\alpha$-$RuCl_3$/metal tunnel junctions in inert atmosphere to carry out temperature- and magnetic-field-dependent IETS on 1L, 2L, and 3L $\alpha$-$RuCl_3$ samples. To maximize inelastic electron tunneling, the metal should possess a sizeable Fermi surface with substantial density of states[137]. We mostly use ultrathin ($<$ 10 nm) $T_d$-$MoTe_2$ as our metal electrode. A

sideview illustration of our device and measurement geometry is shown in Figure 7.3 a and a colorized optical image of a representative device is shown in Figure 7.3 b. Hexagonal boron nitride flakes are used as encapsulation layers for protection.

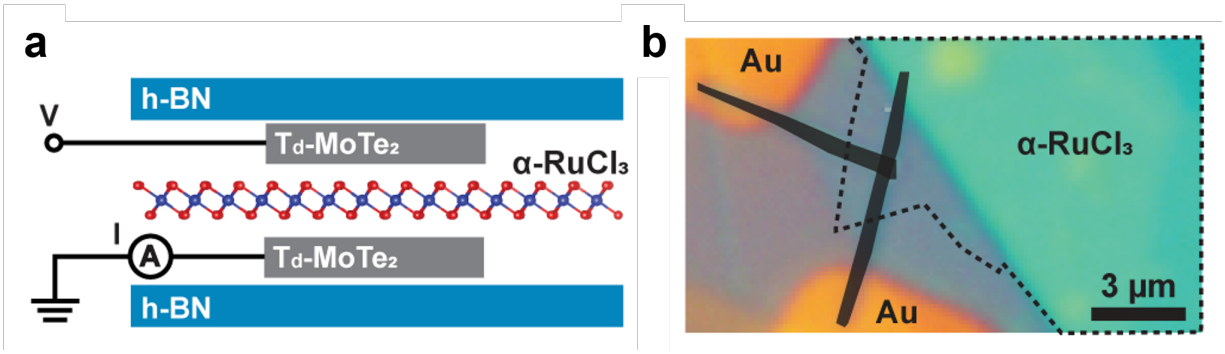


Figure 7.3: IETS device for 1L $\alpha$-$RuCl_3$. (a) Sideview schematic of an IETS device with vertical $T_d$-$MoTe_2$ contacts to few-layer $\alpha$-$RuCl_3$. (b) Colorized optical image of a 1L $\alpha$-$RuCl_3$ device. Black shaded areas represent $T_d$-$MoTe_2$ and dashed lines outline $\alpha$-$RuCl_3$ flake.

The upper panel of Figure 7.4 shows the measured AC conductance ($dI/dV$) of a 1L tunnel junction at 2 K as a function of the DC voltage. Subtle steps in the curve can be seen centered at $\sim \pm 1$ mV, which can be interpreted as increases in the tunneling conductance when the potential difference across the electrodes reaches the energy of a particular inelastic excitation in $\alpha$-$RuCl_3$[138, 95, 96, 116]. These can be seen more clearly as peaks in the numerical derivative ($d^2I/dV^2$) shown in the lower panel of the Figure 7.4. To extract the position and shape of the peaks, we fit them to a pair of Lorentzians (blue) on top of a background (gray)[139]. The resultant fitting is shown in red, which closely traces the experimental result.

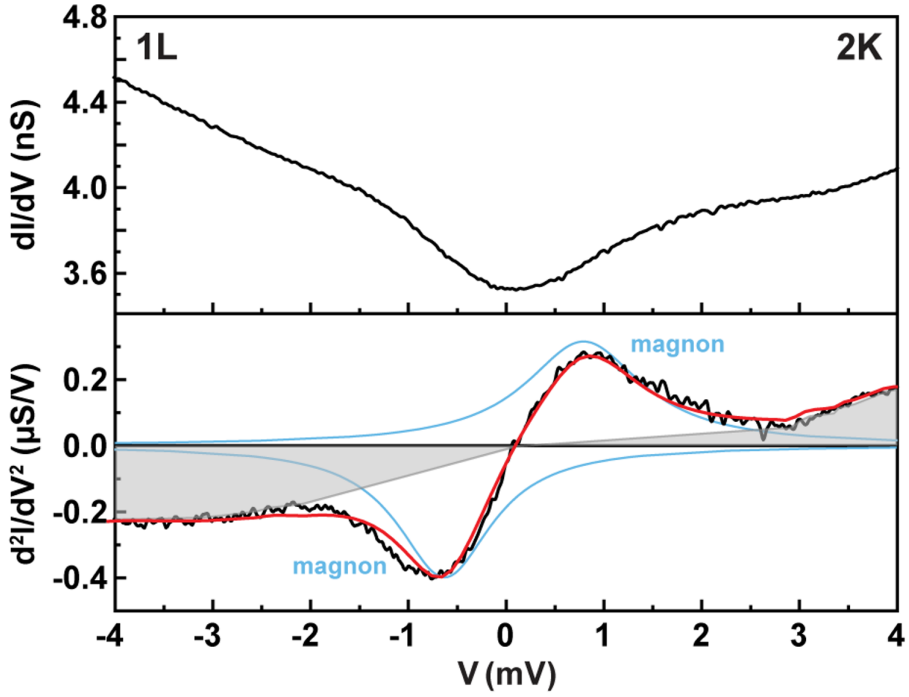


Figure 7.4: Representative IETS results for 1L $\alpha$-$RuCl_3$ taken at 2 K. Upper panel: AC tunneling conductance $dI/dV$ as a function of applied DC voltage showing subtle steps due to magnon excitations at both positive and negative voltage. Lower panel: Numerical derivative (black trace) of experimental $dI/dV$ curve, $d^2I/dV^2$, together with results from fitting (gray: background; blue lines: Lorentzian fits to magnon peaks; red: overall fit).

It is worth to note that to rule out the possibility that the IETS response may arise from $MoTe_2$, we used graphene electrodes, but found that the intensity of the IETS spectra varied from sample to sample. Ref[137] points out that it is important to have large and matched metal Fermi surfaces to gain efficient and consistent scattering. Nevertheless, some samples with graphene electrodes did show the same response at the same voltage bias (Figure 7.5).

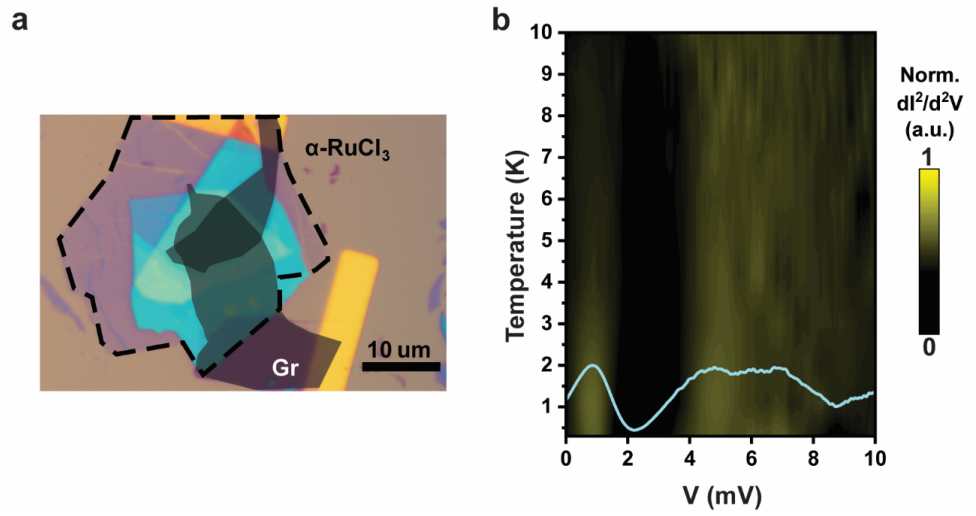


Figure 7.5: IETS sample with few-layer graphene contacts. (a) Colorized optical image of the sample. The IETS sample is fabricated in the same geometry as shown in Figure 7.3, except the $T_d$-$MoTe_2$ is replaced by few-layer graphene and the thickness of $\alpha$-$RuCl_3$ is 5-6 layers. (b) False-color 2D plot of background-subtracted $d^2I/dV^2$ spectrum taken from 0.3 K to 10 K for positive bias. The trace at 0.3 K is overlaid in blue. The low-energy peak at 1 meV is reproduced in this sample, which gradually disappears above $\sim$ 8 K, and the continuum between 4-10 meV is reproduced as well (See Section 7.2.1).

We next investigate the dependence of these excitation peaks on temperature across different thickness samples to understand whether they are of magnetic or phononic nature.

### 7.2.1 Temperature dependence

Figure 7.6 shows the normalized and background-subtracted $d^2I/dV^2$ spectrum for 1L, 2L, and 3L devices from 2 K to 10 K in a 2D false-color plot for positive bias. The mode at $\sim$ 1 meV appears in all three devices at low temperature and disappears above $\sim$ 8 K. This is near $T_N$ for the bulk crystal[128, 87, 140], which suggests a magnetic origin. Indeed, phonon features have been observed in this energy range[141], but they persist up to room

temperature. Linear spin wave and exact diagonalization calculations based on *ab initio* studies show a large magnon scattering intensity near 1 meV at the Y and M points[142], while several experiments have reported bulk magnons near this energy[74, 131, 132, 135]. We have further integrated the previous bulk magnon intensity calculations across the Brillouin zone (see Figure 7.7, produced by our collaborators), and the resultant spectrum indeed exhibits a peak at $\sim$ 1 meV. Our observed mode can thus be attributed to the lowest-energy excitation of the ZZ AFM order.

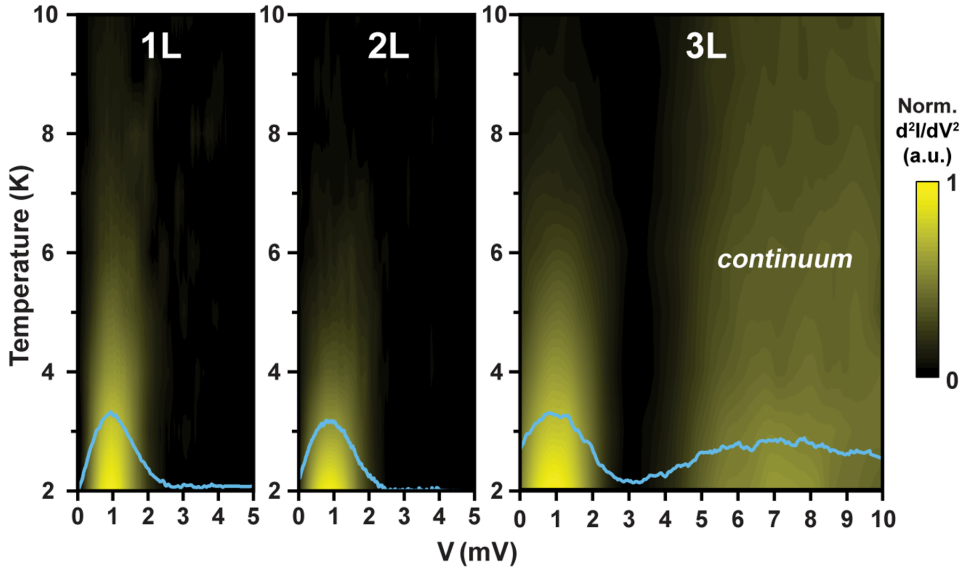


Figure 7.6: False-color plot of normalized and background-subtracted $d^2I/dV^2$ spectra for 1L, 2L, and 3L $\alpha$-$RuCl_3$ from 2 K to 10 K at positive DC bias. The trace at 2 K for each thickness is overlaid in blue. A broad excitation between $\sim$ 5 meV to $\sim$ 10 meV is observed for 3L and attributed to the magnon continuum.

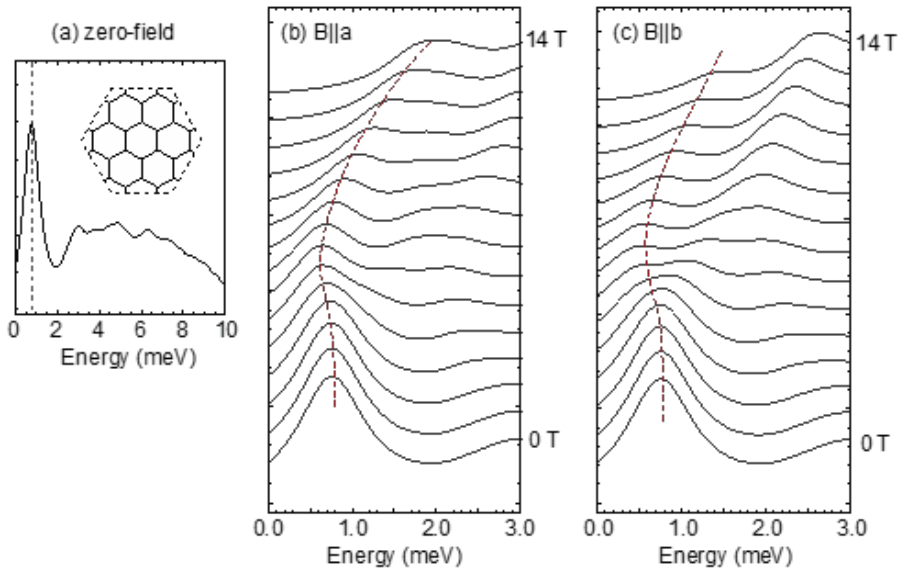


Figure 7.7: Local dynamical spin structure factor for bulk model from ref[142] computed via exact diagonalization. (a) Zero-field result showing peak at lowest (Y/M-point) magnon and higher energy continuum. (b,c) Evolution of low-energy response under in-plane magnetic field.

The smaller overall conductance of the thicker 3L device allows us to probe IETS to higher voltages. Between $\sim$ 5-10 meV, a broad excitation spectrum is observed that persists up to the highest temperature measured with no apparent discontinuity at $T_N$. This is consistent with the continuum excitations identified in bulk crystals by Raman and neutron scattering, which have been discussed to be connected to fractionalized and/or incoherent excitations[71, 72, 74, 77]. Our results thus show that such unconventional magnetic signatures persist down to at least 3L samples.

To determine $T_N$ more precisely for different thicknesses, we start by fitting Lorentzians to the low-energy mode in the manner described above. This function is known to be a convolution (see Equation 3.5) of the intrinsic spectral weight with a temperature-dependent thermal broadening function and a temperature-independent instrument broadening func-

tion (Equation 3.3 and 3.4)[138]. The latter is negligible for our measurement conditions. We thus extract the intrinsic peak by deconvolving the fitted experimental curve with the thermal broadening function and integrating the resultant intensity. The comparison between the broadening effects and raw/intrinsic IETS is shown in Figure 7.8.

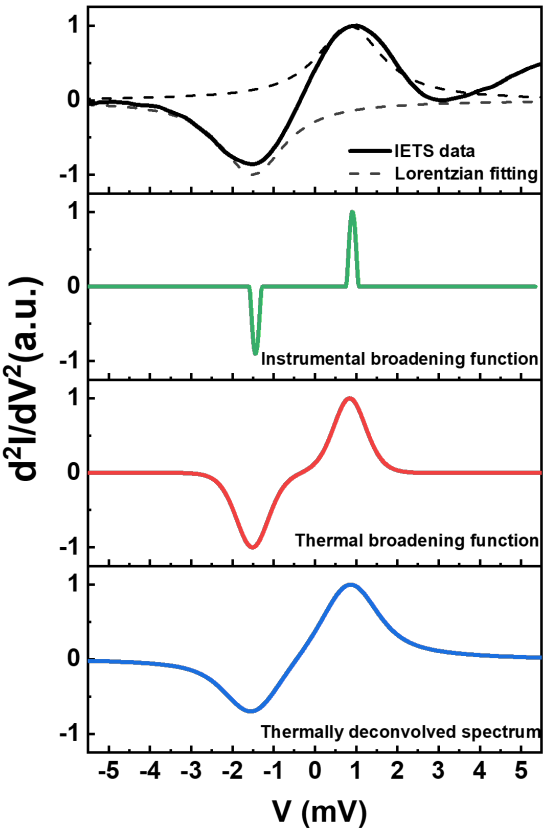


Figure 7.8: Comparison of $d^2I/dV^2$ spectrum at 2 K from a 3L sample (including Lorentzian fitting), thermal broadening function at 2 K, instrumental broadening function, and the thermally deconvolved spectrum.

These values are plotted as a function of temperature in Figure 7.9 a for the three samples. The intercept of a linear fit applied to the data at low temperature yields $T_N$,

values for which are explicitly shown in Figure 7.9 b as a function sample thickness. The range of $T_N$ measured for high-quality bulk crystals is marked by the gray band. Unlike most 2D magnetic materials (for example, $CrI_3$ and $CrBr_3$ in Chapter 5), the critical temperature for $\alpha$-$RuCl_3$ remains essentially unchanged down to monolayer.

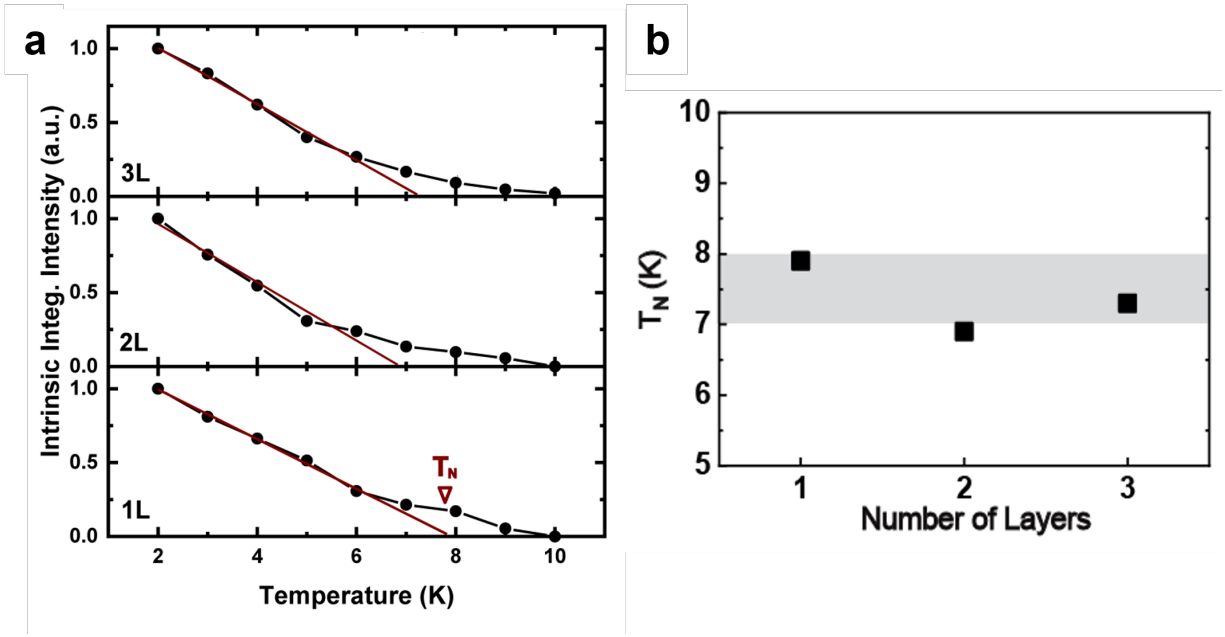


Figure 7.9: Temperature-dependent integrated intensity extracted from IETS for few-layer $\alpha$-$RuCl_3$. (a) Intrinsic integrated intensity of $\sim$ 1 meV magnon for 1L, 2L, and 3L $\alpha$-$RuCl_3$ at each temperature. The data points from 2 K to 6 K are utilized for linear fitting (red lines), whose x-intercepts yield $T_N$. (b) Thickness-dependent $T_N$ for 1L, 2L, and 3L $\alpha$-$RuCl_3$, all of which fall in the range of 7 K-8 K (gray band), which corresponds to the range reported for high-quality bulk crystals.

### 7.2.2 Magnetic field dependence

In bulk $\alpha$-$RuCl_3$, magnons can evolve nonmonotonically with the application of an in-plane magnetic field[73, 77, 76, 135]. For example, the magnons at the $\Gamma$ point first shift down

to lower energies with increasing field, reaching a minimum at $\sim$ 6-8 T before shifting up. This critical field has been suggested to host an intermediate QSL region (between the ZZ ground state and high-field paramagnetic state)[69, 70], which remains controversial, in part because theoretical studies have only identified models with QSL phases induced by out-of-plane fields[61, 78, 82, 80, 81]. Due to the easy-plane anisotropy of bulk crystals, however, an out-of-plane field of $\gtrapprox$ 30T is needed to change the magnetic state, rendering such predicted QSLs largely inaccessible[68, 78, 82, 83, 84, 142, 143]. We thus proceed to measure the low-energy magnon for all three sample thicknesses with changing magnetic field.

In Figure 7.10, we show 1L, 2L, and 3L IETS spectra taken at 2K for $B_{\parallel}$ between 0 and 14 T (in 1 T increments) with the traces background-subtracted and offset for clarity. To determine the magnon energies more quantitatively, we have performed a Lorentzian fit for each trace and the extracted peak positions are marked by the inverted gray triangle in Figure 7.10 a and plotted explicitly in Figure 7.10 b with changing $B_{\parallel}$. The 2L and 3L samples show qualitatively similar characteristics—with increasing field, the magnon energy first decreases and then increases, although the field at which the minimum energy occurs appears to be slightly larger for 2L. These results can be compared with calculations for the momentum-integrated bulk magnon intensity with changing in-plane magnetic field (see Figure 7.7). In addition, we observe that the high-energy continuum feature for 3L also changes with in-plane field (Figure 7.11), which is consistent with its magnetic origin.

In contrast, the magnon for 1L is essentially unchanged with magnetic field up to 14 T, which suggests that the critical in-plane field necessary to drive the monolayer out of the ZZ state is pushed to a substantially higher value. This trend is captured by the thick blue line.

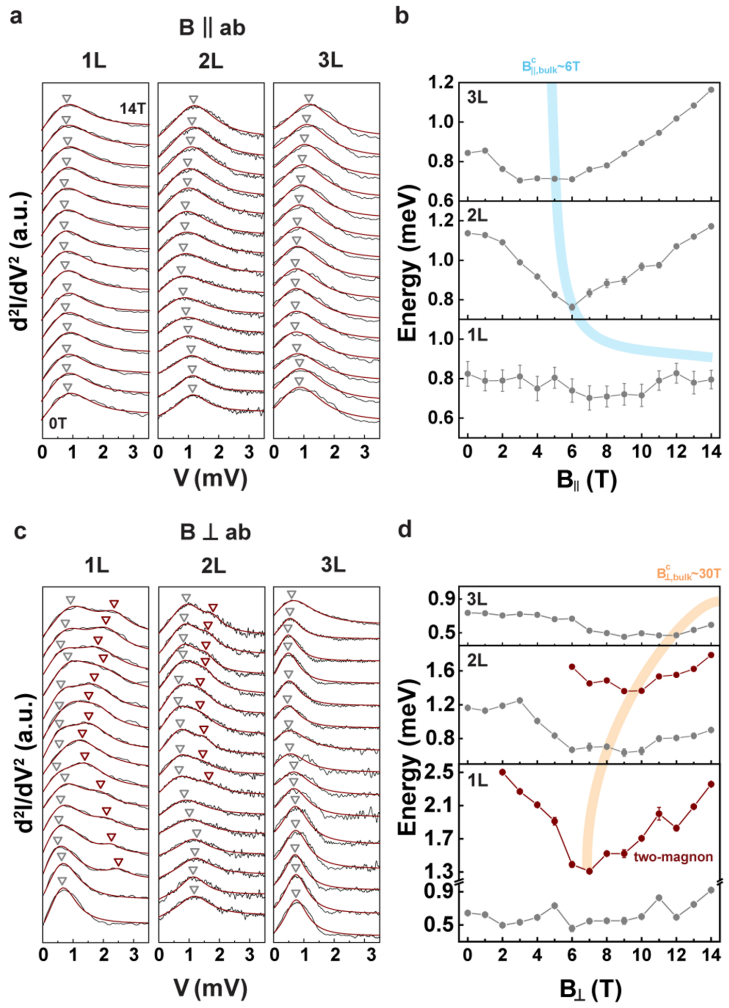


Figure 7.10: Magnetic-field-dependent IETS on few-layer $\alpha$-$RuCl_3$. 1L, 2L, and 3L $\alpha$-$RuCl_3$ spectra (black lines) with changing $B_{\parallel}$ (a) and $B_{\perp}$ (c) from 0 T to 14 T in 1 T increments and offset for clarity. Lorentzian fitting and background subtraction is performed for each $d^2I/dV^2$ trace (red lines). The extracted peak positions are marked by the inverted gray and magenta triangles and plotted explicitly as function of $B_{\parallel}$ (b) and $B_{\perp}$ (d). Gray points are results for low-energy magnon and magenta points are for two-magnon scattering. Thick blue and orange lines capture trends in changing critical field with thickness for $B_{\parallel}$ and $B_{\perp}$, respectively.

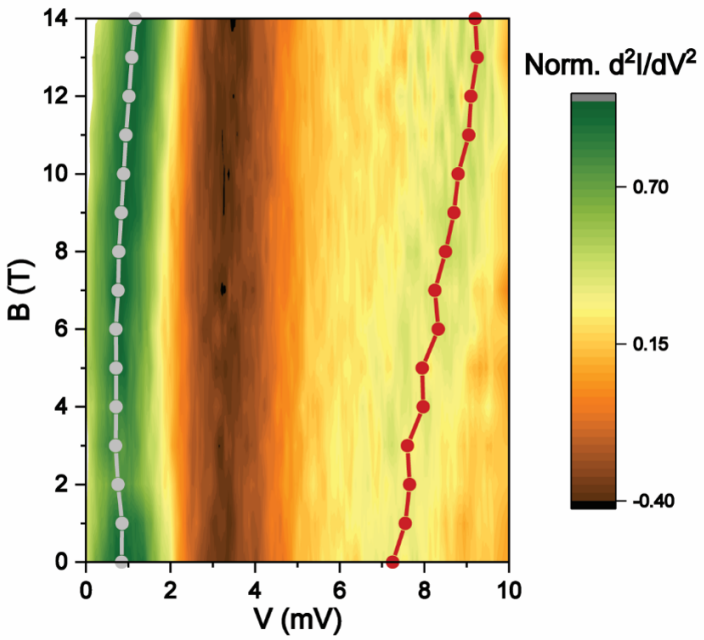


Figure 7.11: False-color plot of normalized IETS spectra without background subtraction for 3L $\alpha$-$RuCl_3$ from 0 T to 14 T. Evolution of the low-energy magnon peak and the maximum position of the magnon continuum is overlaid in gray and red, respectively.

Figure 7.10 c shows the out-of-plane field dependence of the IETS spectra. Here, an opposite trend is observed with changing thickness. The 3L has the stiffest response, consistent with the result for bulk crystals[129], while the low-energy peak position for both 2L and 1L exhibit more curvature with field. Interestingly, a secondary peak at higher energy also develops for the latter samples at finite fields. We have fit all the observed peaks to Lorentzians, and the positions are marked in Figure 7.10 c by gray and magenta inverted triangles and plotted explicitly in Figure 7.10 d as a function of $B_\perp$. At high fields, the secondary peaks appear to shift with field at roughly twice the rate compared with the low-energy magnon, suggesting that they may originate from two-magnon excitation[74, 75, 77, 142]. The larger curvature exhibited by this higher energy mode also allows us to clearly identify the critical field for which the energy is minimum—it

shifts to higher values with increasing thickness. This trend is captured by the thick orange line and is consistent with the extremely large out-of-plane critical field expected for the bulk crystal.

We further note that the observed magnon stiffening for 1L $\alpha$-$RuCl_3$ with in-plane field appears to be independent of whether the field is directed along either of the two in-plane crystalline axes, where the axes are confirmed by Raman spectroscopy on the attached thick flake.

### 7.2.3 Independence of magnons on in-plane field direction for monolayer $\alpha$-$RuCl_3$

Various vibration modes are seen in the Raman spectrum[2] of $\alpha$-$RuCl_3$[144]. In particular, $A_g^4$, $B_g^4$, $A_g^5$ and $B_g^5$ phonon modes have four-fold angular symmetry in their Raman intensity when the light polarization is rotated within the plane[144]. Moreover, in the parallel polarization configuration, the Raman intensity of $A_g^5$ along the b-axis is noticeably larger than along with a-axis, which can be used to determine the crystalline axes of thin flakes[144].

However, the Raman signal from monolayer is significantly weaker than in thicker flakes. Therefore, during sample fabrication, we have chosen an intact flake having both monolayer and a thick area, as shown in the inset of Figure 7.12 a. Because the two areas are attached, it is reasonable to assume that they have the same lattice orientation. Our samples are mounted on a rotatable stage for angle-resolved Raman measurements. Our collaborators first perform polarized Raman spectroscopy (in both crossed and parallel polarization configuration) for the thick area at 0°, where 0° is defined as incident polarization parallel

[2]Raman spectroscopy was carried out at room temperature using a 532 nm excitation laser in backscattering geometry with a beam spot size of ~1 $\mu$m. The laser power was kept at ~0.1 $\mu$W, to minimize the local heating effect. The scattered light was dispersed by a Horiba LabRAM HR Evolution Raman Microscope system and detected by a thermoelectric cooled CCD camera. The h-BN-encapsulated $\alpha$-$RuCl_3$ flakes were mounted on a rotatable stage and measured at every 10°.

to the sharp edge of the thick area (see Figure 7.12 a, main panel). The various peaks observed are assigned based on ref[144]. In particular, $A_g^5$ and $B_g^5$ are relatively strong and close in energy. We then rotate sample in the x-y plane in 10° increments. $A_g^5$ ($B_g^5$) peaks are maximized at 0°, 90°, 180°, and 270° (40°, 130°, 220°, and 310°) in parallel configuration and 40°, 130°, 220°, and 310° (0°, 90°, 180°, and 270°) in crossed configuration (see representative angle-dependent parallel polarization spectra in Figure 7.12 b). We extract the peak properties through Lorentzian fitting and the angle-dependent intensities of $A_g^5$ and $B_g^5$ in parallel configuration are shown in Figure 7.12 c. We then fit the angle dependence according to the expressions taken from ref[144].

We can clearly see that in parallel configuration $A_g^5$ is minimized at $\sim 0°$ and maximized at $\sim 90°$, corresponding to a and b axis, respectively.

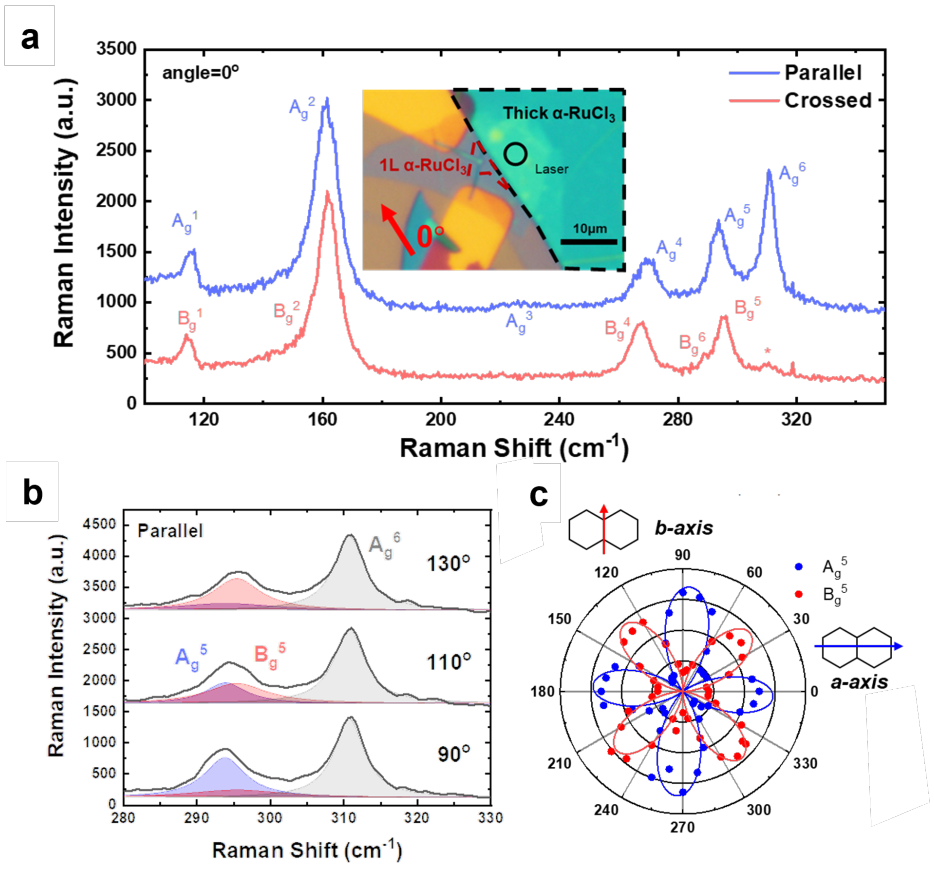


Figure 7.12: Determination of in-plane crystalline axes of 1L $\alpha$-$RuCl_3$ (a) Inset: Optical image of tunneling device showing 1L $\alpha$-$RuCl_3$ connected to a thicker area. Main panel: parallel and cross-polarized Raman spectra taken on thicker $\alpha$-$RuCl_3$. (b) Zoom-in of $A_g^5$, $B_g^5$, and $A_g^6$ phonon modes for various polarization angles in parallel configuration and peak fitting. (c) Polar plot of Raman intensity (in dots) as a function of polarization angle in parallel configuration for $A_g^5$ and $B_g^5$ together with fitting (in lines).

After the a and b axes are determined, a magnetic field is applied along those two directions in IETS measurements. The field-dependent spectra are shown in Figure 7.13 together with their fittings in dark red, and the lower panel plots the fitted peak positions explicitly as a function of magnetic field. Data for both field directions show that the 1

meV magnon has very little change up to 14 T.

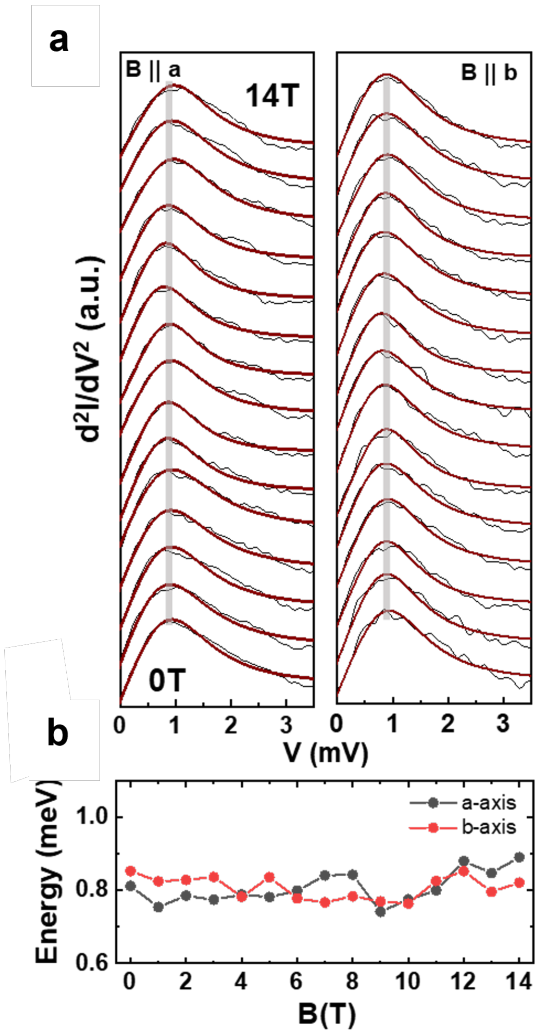


Figure 7.13: Independence of magnons on in-plane field direction. (a) Field dependence of the 1 meV magnon for field along a and b axis. (b) Extracted magnon energy from fitting as a function of magnetic field.

Taken together, the results of Figure 7.10 and Figure 7.13 suggest that the magnetic anisotropy is reversed from easy-plane for bulk crystals to easy-axis (out-of-plane) for 1L

$\alpha$-$RuCl_3$. Such a change is striking; however, we must ascertain whether it is intrinsic to monolayer samples or a result of proximity to the $T_d$-$MoTe_2$, a system with strong spin-orbit coupling.

## 7.3 Lateral Transport Measurement

To address this issue, we have fabricated an ultrashort two-terminal device for 1L $\alpha$-$RuCl_3$ with both few-layer graphene electrodes and top and bottom gates to investigate the field dependence of lateral transport. A colorized scanning electron microscope image and sideview schematic of the device are shown in Figure 7.14 a. The sample is only in contact with h-BN across the channel (length $\sim$ 300 nm). Figure 7.14 b shows the DC current-voltage dependence at base temperature for different gate values. Due to the insulating nature of $\alpha$-$RuCl_3$, the sample only shows measurable current at low bias when large positive gate voltages are applied (electron doping).

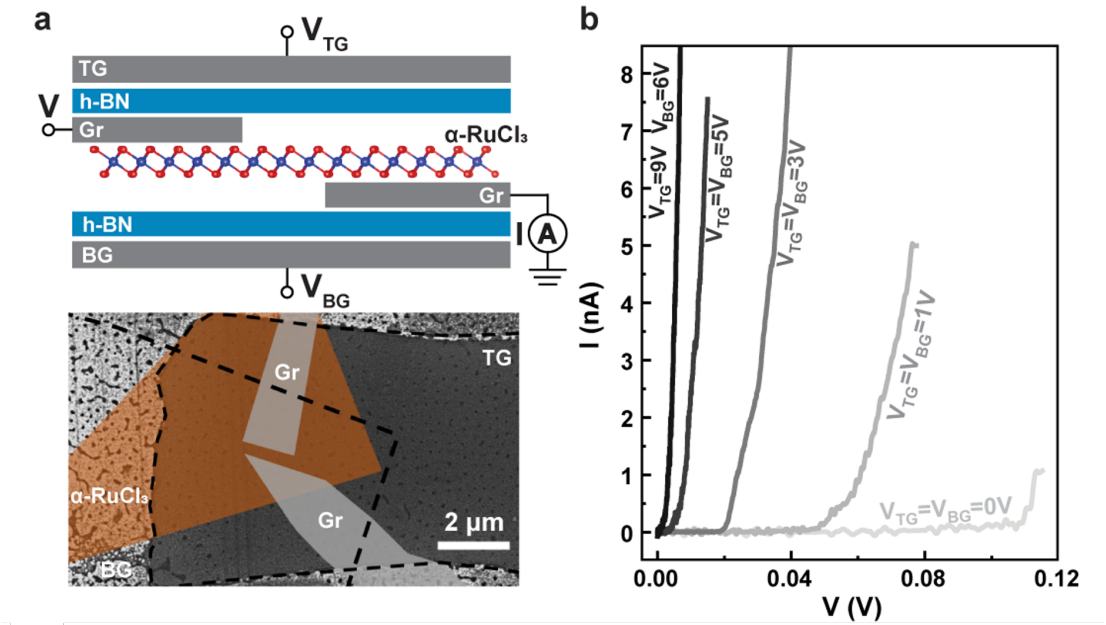


Figure 7.14: Lateral magnetotransport measurement on 1L $\alpha$-$RuCl_3$ with dual gates. (a) Sideview schematic (upper) and colorized scanning electron microscopy image (lower) of device with channel length of $\sim$ 300 nm. (b) DC current-voltage characteristics curves at 2 K taken with various gate voltages.

In the most conductive state ($V_{TG}$ = 9 V, $V_{BG}$ = 6 V), we have measured the AC conductance upon sweeping the magnetic field (both in-plane and out-of-plane) continuously, and the results are plotted in Figure 7.15 for several different temperatures. Overall, there is very little change with in-plane field, consistent with this field direction being along the hard axis. In contrast, there is larger change when the field is applied along the easy axis out of plane. Moreover, a marked kink can be seen in the magnetoconductance at $B_\perp \sim 6.5$ T at low temperatures. This coincides with the critical field for the two-magnon feature measured by IETS. Upon raising the temperature, the kink gradually disappears above $T_N$. These results indicate that the magnetic anisotropy reversal in monolayer $\alpha$-$RuCl_3$ is likely of intrinsic origin as opposed to proximal contact with $T_d$-$MoTe_2$.

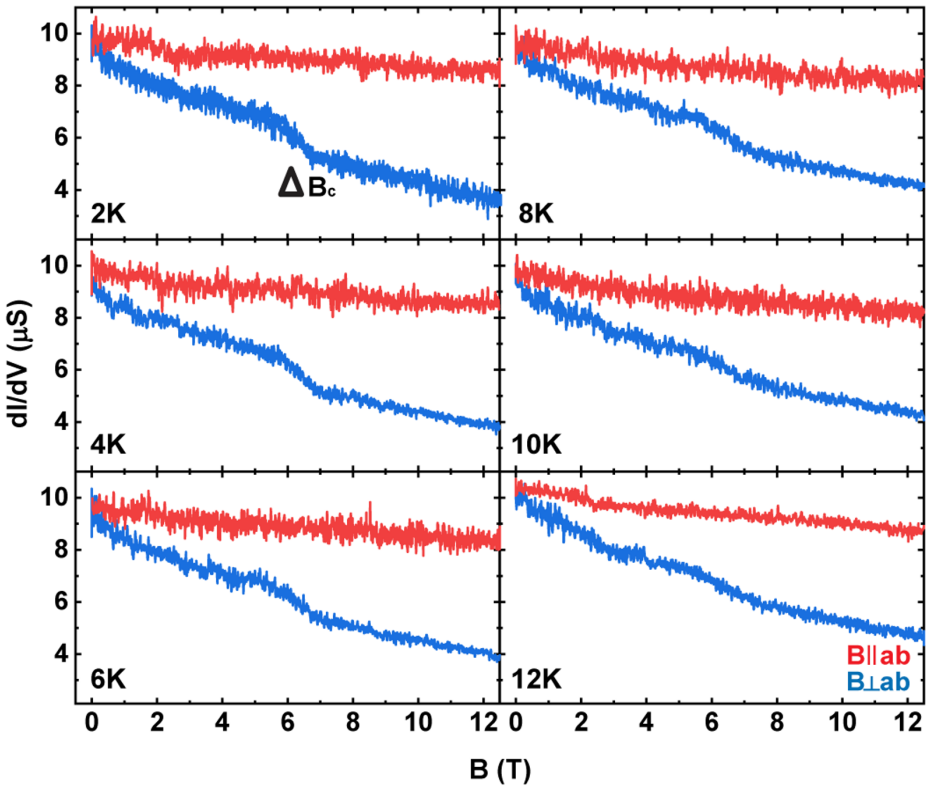


Figure 7.15: AC conductance at 20 mV DC bias, 9 V top gate, and 6 V back gate with changing with $B_{\parallel}$ (red) and $B_{\perp}$ (blue) from 2 K to 12 K. The magnetoconductance has larger change overall with $B_{\perp}$ and a marked kink at $B_{\perp} \sim 6.5$ T that gradually disappears above $T_N \sim 8$ K.

## 7.4 Origin of Magnetic Anisotropy Reversal

### 7.4.1 Electron diffraction measurement

It is well-understood that spin moments in $\alpha$-$RuCl_3$ are strongly coupled to the charge and lattice degrees of freedom[64, 145, 146, 147, 148]. In particular, electron transfer effects have been previously observed in various 2D heterostructures incorporating $\alpha$-$RuCl_3$[149, 150].

Theoretical analysis shows that the magnetic anisotropy is unlikely to be affected by doping, however[151]. Thus, a more probable cause is that the structure of 1L $\alpha$-$RuCl_3$ deviates from that of the bulk crystal.

To investigate whether this is the case, we again turn to electron diffraction measurements performed on the monolayer sample. By carefully fitting the $k_z$ dependence for the various Bragg peaks, we observe three primary distortions of the honeycomb lattice of edge-sharing $RuCl_6$ octahedra, which are illustrated in Figure 7.16 a. First, there is an out-of-plane buckling of the Ru atoms, $\Delta\zeta_{Ru}$, discernable from the asymmetric $(01\bar{1}0)$ and $(0\bar{1}10)$ Bragg rods shown in Figure 7.16 b. Due to negligible overall strain in the lattice (see discussion of Figure 7.1 a), the in-plane distortion of Ru should be insignificant. Second, there is a change in the c-axis position Cl atoms relative to the Ru atoms, $\lambda_{Cl}$, as well as a third in-plane distortion of the Cl atoms that are opposite for the top and bottom sublayers, $\Delta r_{Cl}$. A table summarizing the experimentally bounded values for these three distortions are shown in Figure 7.16 a. Some of these distortions have been previously observed on the surfaces of exfoliated $\alpha$-$RuCl_3$ flakes and have been attributed to Cl vacancies despite preparation in inert atmosphere[152]. Here, diffraction provides a precise measure of the average crystal structure and distortions but is much less sensitive to real-space fluctuations.

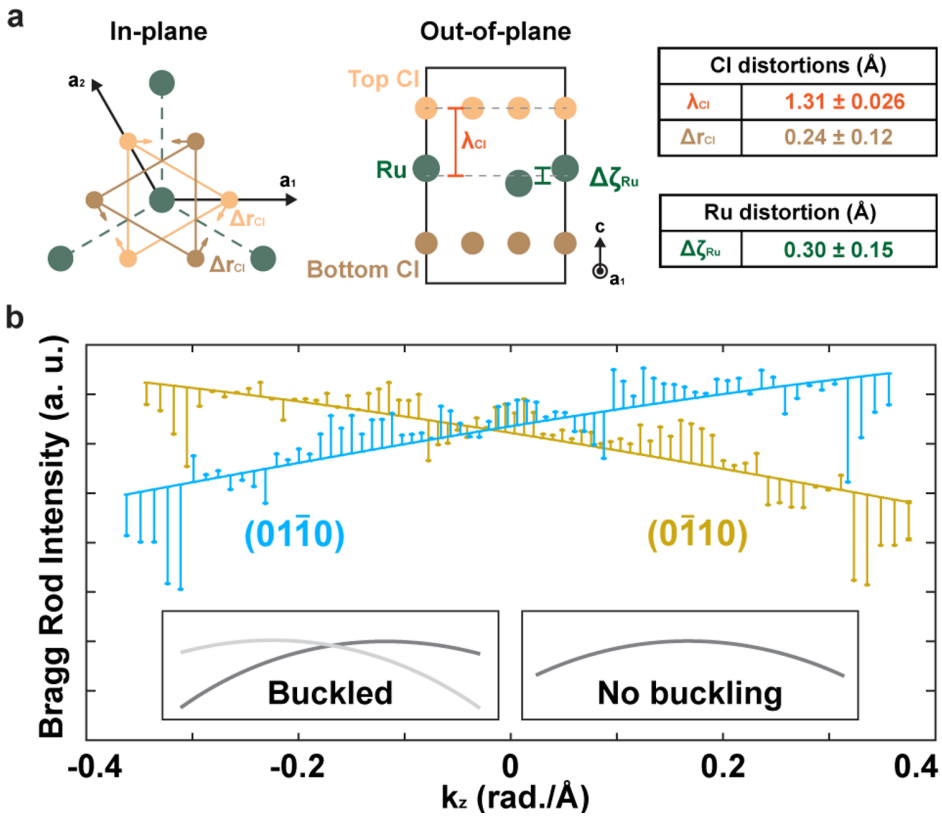


Figure 7.16: Three primary distortions of 1L $\alpha$-$RuCl_3$ identified by our collaborators. (a) Schematic illustration of three distortions (left) and summary of the values determined by 3D electron diffraction measurements (right). (b) Asymmetric $(01\bar{1}0)$ and $(0\bar{1}10)$ Bragg rod intensities vs $k_z$ indicate out-of-plane Ru buckling. Inset: schematic for the two Bragg rods with and without Ru buckling.

### 7.4.2 Ab initio calculation

The reversal of magnetic anisotropy for 1L $\alpha$-$RuCl_3$ signifies modification of the spin Hamiltonian $H = \sum_{<i,j>} \vec{S}_i \cdot \mathbf{M}_{ij} \cdot \vec{S}_j$ due to the observed distortions. For co-planar Ru, the matrix

$\mathbf{M}$ (for the z bond) can be expressed as $\begin{pmatrix} J & \Gamma & \Gamma' \\ \Gamma & J & \Gamma' \\ \Gamma' & \Gamma' & J+K \end{pmatrix}$ for nearest-neighbor interactions, where $J$, $K$, and $\Gamma$ ($\Gamma'$) refer to the Heisenberg, Kitaev, and off-diagonal coupling terms, respectively, although a third neighbor Heisenberg term $J_3$ is expected to contribute as well. With Ru buckling, the symmetry of $\mathbf{M}$ is lowered to $\begin{pmatrix} J_x & \Gamma_{xy} & \Gamma_{xz} \\ \Gamma_{xy} & J_y & \Gamma_{yz} \\ \Gamma_{xz} & \Gamma_{yz} & J_z \end{pmatrix}$, where the Kitaev coupling is now defined by $K = J_z - (J_x + J_y)/2$. The sense of the exchange anisotropy is determined by the sum of the off-diagonal couplings $\sum\Gamma = \Gamma_{xy} + \Gamma_{xz} + \Gamma_{yz}$ with positive (negative) values indicative of easy-plane (easy-axis). In the bulk, the large out-of-plane critical field stems primarily from the large off-diagonal $\Gamma > 0$ term, which is the main competitor to the Kitaev interaction.

To correlate the distortions with microscopic interactions, we have performed *ab initio* calculations of the spin Hamiltonian for a range of distortions and evaluated the classical ground state magnetic order, schematics of which are shown in Figure 7.17 a. The results are shown in the lower panels of Figure 7.17 b as two sets of false-color plots for $\sum\Gamma$ as a function of the Cl distortions. The left (right) panel is calculated without (with) Ru buckling. The plots also map out a phase diagram for the magnetic ordering. Regions where classical stripy (Str), ZZ, and ferromagnetic (FM) phases compete have been theorized to realize a QSL state in the bulk[66, 78]. The position of bulk $\alpha$-$RuCl_3$ is marked by the black circle in the left panel[127, 128], while the dashed rectangle in the right panel outlines our 1L $\alpha$-$RuCl_3$ within the error limits of electron diffraction.

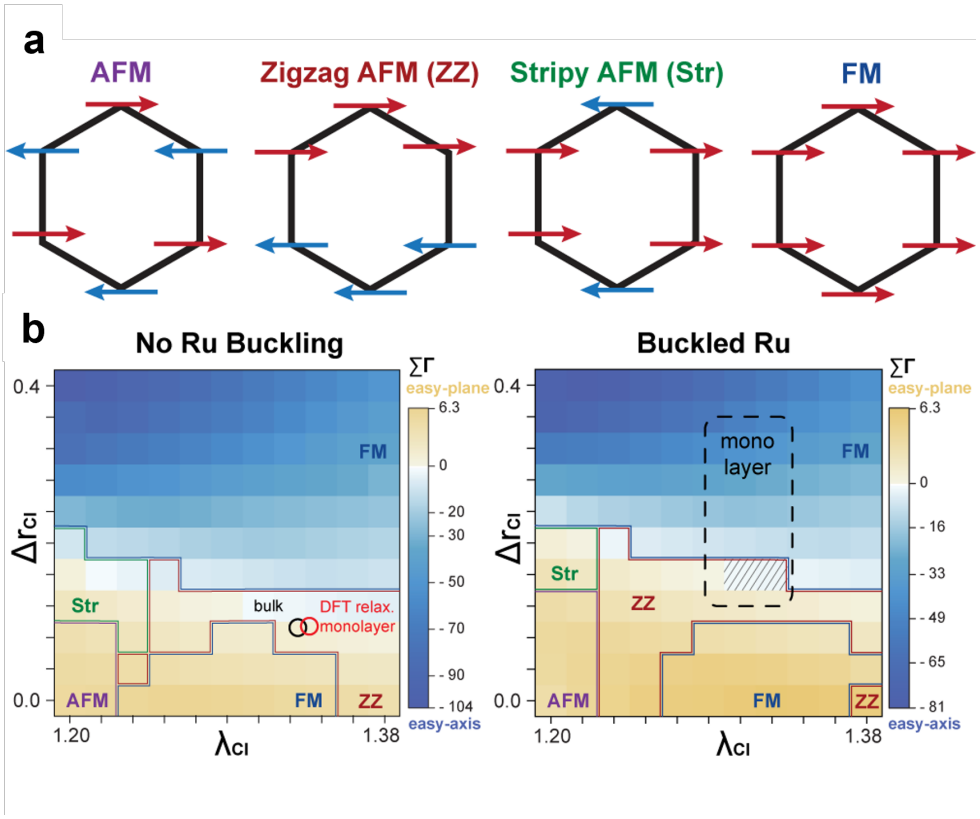


Figure 7.17: Magnetic phase diagram based on *ab initio* study. (a) Schematics of various classical magnetic orders in phase diagram. (b) Magnetic phase diagram determined by *ab initio* calculations of $\sum \Gamma$ as a function of the Cl distortions without Ru buckling ($\Delta\zeta_{Ru} = 0$ Å, left) and with Ru buckling ($\Delta\zeta_{Ru} = 0.3$ Å, right). Yellow (blue) regions correspond to easy-plane (easy-axis) magnetic anisotropy. Positions for the experimental bulk structure and DFT-relaxed monolayer are circled in the case of no buckling. The dashed rectangle in the right panel outlines our 1L $\alpha$-$RuCl_3$ within the error limits of electron diffraction. Hashed areas mark regions within the rectangle where the ZZ magnetic anisotropy has flipped to out-of-plane (easy-axis).

We have also used density functional theory to calculate the relaxed structure of the freestanding monolayer, which appears near that of the experimental bulk structure and

does not exhibit Ru buckling (see red circle, left panel). According to our collaborators' DFT calculation, while the modulation of the Ru heights can be induced by Cl vacancies on average, the distortion rapidly decays away from the Cl vacancy location and a very high density of vacancies ($> 10\%$, on the scale of one vacancy per unit cell) would be required to yield the experimentally observed degree of buckling, which is inconsistent with our electron diffraction measurements. Additionally, DFT calculation on monolayer $RuCl_3$ sandwiched between two layers of h-BN does not show a significant buckling of the Ru atoms. Therefore, while the precise microscopic origin of the observed buckling is left as an open question, we can effectively rule out the effect of the substrate as well as a high density of Cl vacancies.

Hashed areas in the phase diagram on the right of Figure 7.17 b mark regions of within the ZZ state within the dashed rectangle where the magnetic anisotropy has flipped to out-of-plane, which all lie on the border to FM order. To narrow the 1L phase boundary further, we have performed MCD measurements[3] on 1L $\alpha$-$RuCl_3$ to measure the out-of-plane magnetization and the results are inconsistent with a ferromagnetic (FM) phase with easy axis anisotropy (Figure 7.18), indicating that our monolayers most likely retain the ZZ configuration and possess a value of $\sum \Gamma$ that is small and negative (hence reside in the hashed region.

[3]The experimental details can be found in Section 5.2.

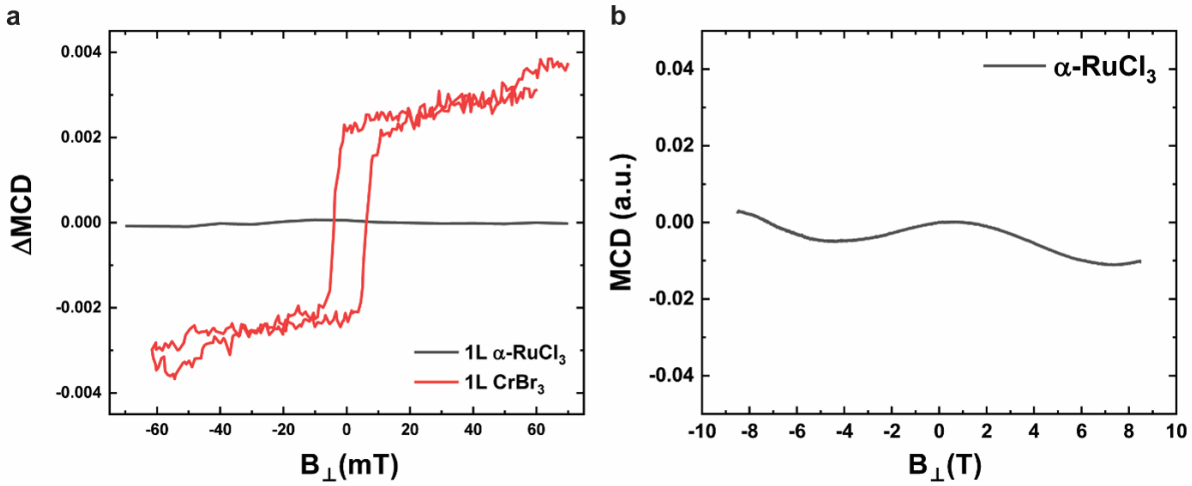


Figure 7.18: MCD measurements comparing 1L $\alpha$-$RuCl_3$ and 1L $CrBr_3$. (a) $\Delta MCD = MCD - MCD(0T)$ for 1L $\alpha$-$RuCl_3$ at 3.5 K and 1L $CrBr_3$ at 5 K between ±70 mT. The data for 1L $CrBr_3$ is reproduced from Figure 5.5. (b): MCD data for 1L $\alpha$-$RuCl_3$ at 3.5 K between ±8 T.

The various exchange terms estimated for this region as well as for the bulk structure are summarized below in Table 7.1. We thus see that the anisotropy reversal in monolayer samples is largely driven by the in-plane Cl distortion, which suppresses and reverses the off-diagonal exchange. 1L $\alpha$-$RuCl_3$ appears to be near a transition to out-of-plane FM ordering as a result. Proximity to this phase boundary necessarily leads to greater spin frustration and an enhanced Kitaev interaction. Specifically, we calculate $K = J_z - (J_x + J_y)/2 =$ -8.25 meV for the hashed region, larger than that for the bulk. Due to out-of-plane Cl compression relative to the bulk structure, 1L $\alpha$-$RuCl_3$ also lies closer to the region where Str, ZZ, and out-of-plane FM phases compete.

| | $J$ | | $K$ | $\Gamma$ | $\Gamma'$ | |
|---|---|---|---|---|---|---|
| No buckling (bulk $\alpha$-$RuCl_3$) | -3.3 | | -6.4 | 3.6 | -0.7 | |
| | $J_x$ | $J_y$ | $J_z$ | $\Gamma_{xy}$ | $\Gamma_{yz}$ | $\Gamma_{xz}$ |
| Ru buckling (1L $\alpha$-$RuCl_3$ ) | -3.1 | -4 | -11.8 | 2.3 | -4.5 | 1.4 |

Table 7.1: Summary of the estimated exchange couplings (meV) for 1L and bulk $\alpha$-$RuCl_3$.

## 7.5 Conclusion

In conclusion, our tunneling measurements on 2D $\alpha$-$RuCl_3$ reveal the presence of single- and two-magnons down to the monolayer limit and a magnon continuum in 3L. The evolution of magnons with magnetic field indicates a clear change in the magnetic anisotropy from easy-plane to easy-axis in monolayer form that is supported by magnetotransport measurements in a gated lateral geometry. 3D electron diffraction shows that 1L $\alpha$-$RuCl_3$ possesses several structural distortions, among which an in-plane Cl distortion predominantly drives the anisotropy reversal. This is supported by *ab initio* calculations, which are also used to extract a microscopic spin Hamiltonian and distortion-dependent magnetic phase diagram.

Relative to the bulk, the ground state of monolayer $\alpha$-$RuCl_3$ has a larger Kitaev interaction and lies in closer proximity to the intersection of several competing spin orders. Furthermore, while a field-induced QSL for in-plane fields in bulk $\alpha$-$RuCl_3$ remains a subject of intense debate, a variety of theoretical works have predicted QSL phases for out-of-plane fields that have hitherto been inaccessible due to the large easy-plane anisotropy[61, 78, 79, 80, 81]. Such states may now be potentially realized for monolayer samples. Our results demonstrate the importance of dimensionality in tuning magnetism in strongly correlated spin systems and pave the way for versatile experimental knobs used for 2D materials (electric field, doping, strain etc.) to further modify the magnetic order in atomically thin $\alpha$-$RuCl_3$.

# Chapter 8

# Summary and Outlook

## 8.1 Summary

This thesis is aimed at exploring potential application of 2D magnetic materials and investigating 2D magnetism in different systems. To start, we gave a brief summary of current progress in theory and experiments of 2D materials and 2D magnetic materials, among which two types of van der Waals magnetic materials attract our attention: chromium trihalides and $\alpha$-$RuCl_3$. In the next chapter, we summarize their magnetic properties for bulk crystals, along with a brief description of a generalized spin Hamiltonian. In particular, a simple summary of the Kitaev model and its materialization, is presented. Chapter 3 describes a powerful tool, tunneling heterostructure, for probing interlayer magnetism and magnetic excitations.

The following four chapters are based on three separate projects, two of which have been published. In Chapter 4, we report a very large magnetoresistance in a tunnel heterostructure incorporating few-layer $CrI_3$. Thanks to its antiferromagnetic interlayer coupling, the magnetoresistance can rise up to one million percent at a certain condition. This work not only shows the potential opportunities in spintronics, but also demonstrates the ability of tunneling heterostructures for probing 2D magnetism.

In Chapter 5 and 6, we comprehensively investigate the 2D magnetism for the three chromium trihalides compounds. The interlayer and intralayer magnetism are systematically studied and summarized, wherein a new measuring technique is adopted, IETS. Magnon excitations are clearly extracted from the plots of IETS vs magnetic field for the three materials, showing the sensitivity of IETS to quasi-particle excitation in 2D materials.

Lastly, we present our results on 2D $\alpha$-$RuCl_3$. Surprisingly, we find the strong easy-plane anisotropy is completely reversed into easy-axis in monolayer, with a critical field close to 6-7 T. The former causes a tremendous difficulty to realize the predicted spin liquid state. This observation shows the feasibility of realizing spin liquid state in monolayer $\alpha$-$RuCl_3$ with an intermediate magnetic out-of-plane field.

## 8.2 Outlook: Controlling 2D Magnetism

Various knobs (pressure[153], strain[154], electrostatic doping[108], electric field[120], etc.) have been experimentally demonstrated to effectively control the 2D magnetism. Since the discovery of the exotic properties of twisted bilayer graphene[155], twisting becomes a unique controlling knob to induce quantum phase transition in 2D materials. As discussed in Chapter 2, the reason why the 2D magnetism of $CrI_3$ is distinct from 3D one is the change in layer stacking, which is exactly where the interlayer magnetism is sensitive to. Some theoretical simulations have illustrated that by twisting, various stacking can coexist, hosting different types of interlayer magnetism (AFM or FM)[47]. Recently, several groups have published results on twisted bilayer or double-bilayer $CrI_3$[156, 157], claiming the existence of noncolinear magnetic states and coexistence of AFM and FM coupling by optical approaches, whereas the transport results are still lacking.

Currently, we are implementing this idea and already have some preliminary data. We are able to fabricate a tunnel junction incorporating with twisted double bilayer $CrI_3$ at nearly 1°. Figure 8.1 shows that the comparison of tunneling magnetoresistance normalized by junction area as function of out-of-plane magnetic field. Instead of a plateau between

1 and 2 T, we observe a continuous change in magnetoresistance. This means that 1. The original AFM interlayer coupling is destroyed; 2. Noncollinear spins may exist, whose constant canting as function of field might be related to the continuous behaviour. Furthermore, the amplitude of magnetoresistance for the twisted sample is largely reduced, which may relate to the formation of FM interlayer coupling. The ongoing study might open a new page for the 2D magnetism study.

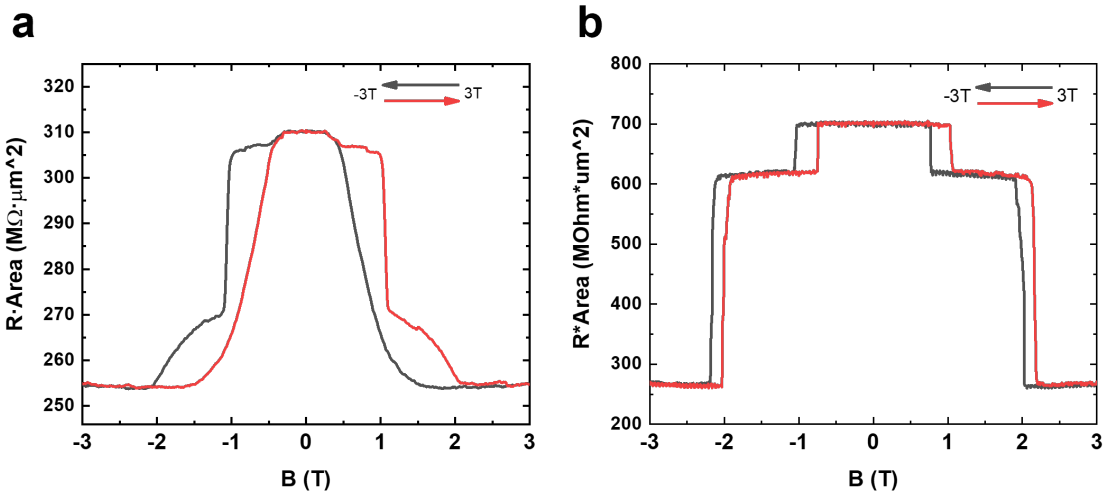


Figure 8.1: Preliminary data for normalized magnetoresistance of (a) twisted double-bilayer $CrI_3$ and (b) regular four-layer $CrI_3$ as a function of out-of-plane magnetic field.

# References


[1] M Ali Omar. *Elementary solid state physics: principles and applications*. Pearson Education India, 1975.

[2] Neil W Ashcroft and N David Mermin. Solid state physics, college edn. *Thomson Learning Inc*, 1976.

[3] Cheng Gong and Xiang Zhang. Two-dimensional magnetic crystals and emergent heterostructure devices. *Science*, 363(6428):eaav4450, 2019.

[4] Po W Anderson. Antiferromagnetism. theory of superexchange interaction. *Physical Review*, 79(2):350, 1950.

[5] John B Goodenough. An interpretation of the magnetic properties of the perovskite-type mixed crystals la1- xsrxcoo3- $\lambda$. *Journal of Physics and Chemistry of Solids*, 6(2-3):287–297, 1958.

[6] Junjiro Kanamori. Superexchange interaction and symmetry properties of electron orbitals. *Journal of Physics and Chemistry of Solids*, 10(2-3):87–98, 1959.

[7] Xueyang Li, Hongyu Yu, Feng Lou, Junsheng Feng, Myung-Hwan Whangbo, and Hongjun Xiang. Spin hamiltonians in magnets: Theories and computations. *Molecules*, 26(4):803, 2021.

[8] Anjan Soumyanarayanan, Nicolas Reyren, Albert Fert, and Christos Panagopoulos. Emergent phenomena induced by spin–orbit coupling at surfaces and interfaces. *Nature*, 539(7630):509–517, 2016.

[9] G De Vries, DJ Breed, EP Maarschall, and AR Miedema. Experiments on two-dimensional heisenberg systems. *Journal of Applied Physics*, 39(2):1207–1208, 1968.

[10] JF Gregg, W Allen, K Ounadjela, M Viret, M Hehn, SM Thompson, and JMD Coey. Giant magnetoresistive effects in a single element magnetic thin film. *Physical Review Letters*, 77(8):1580, 1996.

[11] N David Mermin and Herbert Wagner. Absence of ferromagnetism or antiferromagnetism in one-or two-dimensional isotropic heisenberg models. *Physical Review Letters*, 17(22):1133, 1966.

[12] Pierre C Hohenberg. Existence of long-range order in one and two dimensions. *Physical Review*, 158(2):383, 1967.

[13] P Bruno. Magnetization and curie temperature of ferromagnetic ultrathin films: The influence of magnetic anisotropy and dipolar interactions. *MRS Online Proceedings Library (OPL)*, 231, 1991.

[14] Cheng Gong, Lin Li, Zhenglu Li, Huiwen Ji, Alex Stern, Yang Xia, Ting Cao, Wei Bao, Chenzhe Wang, Yuan Wang, et al. Discovery of intrinsic ferromagnetism in two-dimensional van der waals crystals. *Nature*, 546(7657):265–269, 2017.

[15] Lars Onsager. Crystal statistics. i. a two-dimensional model with an order-disorder transition. *Physical Review*, 65(3-4):117, 1944.

[16] Magnetic Gibertini, Maciej Koperski, Alberto F Morpurgo, and Konstantin S Novoselov. Magnetic 2d materials and heterostructures. *Nature nanotechnology*, 14(5):408–419, 2019.

[17] VL314399 Berezinskii. Destruction of long-range order in one-dimensional and two-dimensional systems having a continuous symmetry group i. classical systems. *Sov. Phys. JETP*, 32(3):493–500, 1971.

[18] John Michael Kosterlitz and David James Thouless. Ordering, metastability and phase transitions in two-dimensional systems. *Journal of Physics C: Solid State Physics*, 6(7):1181, 1973.

[19] Kostya S Novoselov, Andre K Geim, Sergei V Morozov, De-eng Jiang, Yanshui Zhang, Sergey V Dubonos, Irina V Grigorieva, and Alexandr A Firsov. Electric field effect in atomically thin carbon films. *science*, 306(5696):666–669, 2004.

[20] Bevin Huang, Genevieve Clark, Efrén Navarro-Moratalla, Dahlia R Klein, Ran Cheng, Kyle L Seyler, Ding Zhong, Emma Schmidgall, Michael A McGuire, David H Cobden, et al. Layer-dependent ferromagnetism in a van der waals crystal down to the monolayer limit. *Nature*, 546(7657):270–273, 2017.

[21] Sheneve Z Butler, Shawna M Hollen, Linyou Cao, Yi Cui, Jay A Gupta, Humberto R Gutiérrez, Tony F Heinz, Seung Sae Hong, Jiaxing Huang, Ariel F Ismach, et al. Progress, challenges, and opportunities in two-dimensional materials beyond graphene. *ACS nano*, 7(4):2898–2926, 2013.

[22] Rai Moriya, Takehiro Yamaguchi, Yoshihisa Inoue, Yohta Sata, Sei Morikawa, Satoru Masubuchi, and Tomoki Machida. Vertical field effect transistor based on graphene/transition metal dichalcogenide van der waals heterostructure. *ECS Transactions*, 69(5):357, 2015.

[23] Qing Hua Wang, Kourosh Kalantar-Zadeh, Andras Kis, Jonathan N Coleman, and Michael S Strano. Electronics and optoelectronics of two-dimensional transition metal dichalcogenides. *Nature nanotechnology*, 7(11):699–712, 2012.

[24] Ming Liu, Xiaobo Yin, Erick Ulin-Avila, Baisong Geng, Thomas Zentgraf, Long Ju, Feng Wang, and Xiang Zhang. A graphene-based broadband optical modulator. *Nature*, 474(7349):64–67, 2011.

[25] Yuanbo Zhang, Yan-Wen Tan, Horst L Stormer, and Philip Kim. Experimental observation of the quantum hall effect and berry's phase in graphene. *nature*, 438(7065):201–204, 2005.

[26] Kirill I Bolotin, Fereshte Ghahari, Michael D Shulman, Horst L Stormer, and Philip Kim. Observation of the fractional quantum hall effect in graphene. *Nature*, 462(7270):196–199, 2009.

[27] VP Gusynin and SG Sharapov. Unconventional integer quantum hall effect in graphene. *Physical review letters*, 95(14):146801, 2005.

[28] Yuanbo Zhang, Tsung-Ta Tang, Caglar Girit, Zhao Hao, Michael C Martin, Alex Zettl, Michael F Crommie, Y Ron Shen, and Feng Wang. Direct observation of a widely tunable bandgap in bilayer graphene. *Nature*, 459(7248):820–823, 2009.

[29] Kin Fai Mak, Changgu Lee, James Hone, Jie Shan, and Tony F Heinz. Atomically thin mos 2: a new direct-gap semiconductor. *Physical review letters*, 105(13):136805, 2010.

[30] Yuan Liu, Nathan O Weiss, Xidong Duan, Hung-Chieh Cheng, Yu Huang, and Xiangfeng Duan. Van der waals heterostructures and devices. *Nature Reviews Materials*, 1(9):1–17, 2016.

[31] Akash Laturia, Maarten L Van de Put, and William G Vandenberghe. Dielectric properties of hexagonal boron nitride and transition metal dichalcogenides: from monolayer to bulk. *npj 2D Materials and Applications*, 2(1):1–7, 2018.

[32] Cory R Dean, Andrea F Young, Inanc Meric, Chris Lee, Lei Wang, Sebastian Sorgenfrei, Kenji Watanabe, Takashi Taniguchi, Phillip Kim, Kenneth L Shepard, et al.

Boron nitride substrates for high-quality graphene electronics. *Nature nanotechnology*, 5(10):722–726, 2010.

[33] L Britnell, RV Gorbachev, R Jalil, BD Belle, F Schedin, A Mishchenko, T Georgiou, MI Katsnelson, L Eaves, SV Morozov, et al. Field-effect tunneling transistor based on vertical graphene heterostructures. *Science*, 335(6071):947–950, 2012.

[34] Miguel M Ugeda, Iván Brihuega, Francisco Guinea, and José M Gómez-Rodríguez. Missing atom as a source of carbon magnetism. *Physical Review Letters*, 104(9):096804, 2010.

[35] Zhiyong Wang, Chi Tang, Raymond Sachs, Yafis Barlas, and Jing Shi. Proximity-induced ferromagnetism in graphene revealed by the anomalous hall effect. *Physical review letters*, 114(1):016603, 2015.

[36] Michael A McGuire, Hemant Dixit, Valentino R Cooper, and Brian C Sales. Coupling of crystal structure and magnetism in the layered, ferromagnetic insulator cri3. *Chemistry of Materials*, 27(2):612–620, 2015.

[37] V Carteaux, D Brunet, G Ouvrard, and G Andre. Crystallographic, magnetic and electronic structures of a new layered ferromagnetic compound cr2ge2te6. *Journal of Physics: Condensed Matter*, 7(1):69, 1995.

[38] Dahlia R Klein, David MacNeill, Qian Song, Daniel T Larson, Shiang Fang, Mingyu Xu, Raquel A Ribeiro, Paul C Canfield, Efthimios Kaxiras, Riccardo Comin, et al. Enhancement of interlayer exchange in an ultrathin two-dimensional magnet. *Nature Physics*, 15(12):1255–1260, 2019.

[39] Jae-Ung Lee, Sungmin Lee, Ji Hoon Ryoo, Soonmin Kang, Tae Yun Kim, Pilkwang Kim, Cheol-Hwan Park, Je-Geun Park, and Hyeonsik Cheong. Ising-type magnetic ordering in atomically thin feps3. *Nano letters*, 16(12):7433–7438, 2016.

[40] Yujun Deng, Yijun Yu, Yichen Song, Jingzhao Zhang, Nai Zhou Wang, Zeyuan Sun, Yangfan Yi, Yi Zheng Wu, Shiwei Wu, Junyi Zhu, et al. Gate-tunable room-temperature ferromagnetism in two-dimensional fe3gete2. *Nature*, 563(7729):94–99, 2018.

[41] Wei He, Lingling Kong, Weina Zhao, and Peng Yu. Atomically thin 2d van der waals magnetic materials: Fabrications, structure, magnetic properties and applications. *Coatings*, 12(2):122, 2022.

[42] Michael Freedman, Alexei Kitaev, Michael Larsen, and Zhenghan Wang. Topological quantum computation. *Bulletin of the American Mathematical Society*, 40(1):31–38, 2003.

[43] Jose L Lado and Joaquín Fernández-Rossier. On the origin of magnetic anisotropy in two dimensional cri3. *2D Materials*, 4(3):035002, 2017.

[44] Tula R Paudel and Evgeny Y Tsymbal. Spin filtering in cri3 tunnel junctions. *ACS applied materials & interfaces*, 11(17):15781–15787, 2019.

[45] Tôru Moriya. Anisotropic superexchange interaction and weak ferromagnetism. *Physical review*, 120(1):91, 1960.

[46] Rodrigo Jaeschke-Ubiergo, E Suárez Morell, and Alvaro Sebastian Nunez. Theory of magnetism in the van der waals magnet cri 3. *Physical Review B*, 103(17):174410, 2021.

[47] Muhammad Akram, Harrison LaBollita, Dibyendu Dey, Jesse Kapeghian, Onur Erten, and Antia S Botana. Moiré skyrmions and chiral magnetic phases in twisted crx3 (x= i, br, and cl) bilayers. *Nano Letters*, 21(15):6633–6639, 2021.

[48] Nikhil Sivadas, Satoshi Okamoto, Xiaodong Xu, Craig J Fennie, and Di Xiao. Stacking-dependent magnetism in bilayer cri3. *Nano letters*, 18(12):7658–7664, 2018.

[49] Peiheng Jiang, Cong Wang, Dachuan Chen, Zhicheng Zhong, Zhe Yuan, Zhong-Yi Lu, and Wei Ji. Stacking tunable interlayer magnetism in bilayer cri 3. *Physical Review B*, 99(14):144401, 2019.

[50] Zeyuan Sun, Yangfan Yi, Tiancheng Song, Genevieve Clark, Bevin Huang, Yuwei Shan, Shuang Wu, Di Huang, Chunlei Gao, Zhanghai Chen, et al. Giant nonreciprocal second-harmonic generation from antiferromagnetic bilayer cri3. *Nature*, 572(7770):497–501, 2019.

[51] Tiancheng Song, Zaiyao Fei, Matthew Yankowitz, Zhong Lin, Qianni Jiang, Kyle Hwangbo, Qi Zhang, Bosong Sun, Takashi Taniguchi, Kenji Watanabe, et al. Switching 2d magnetic states via pressure tuning of layer stacking. *Nature materials*, 18(12):1298–1302, 2019.

[52] Ichiro Tsubokawa. On the magnetic properties of a crbr3 single crystal. *Journal of the Physical Society of Japan*, 15(9):1664–1668, 1960.

[53] Michael A McGuire, Genevieve Clark, KC Santosh, W Michael Chance, Gerald E Jellison Jr, Valentino R Cooper, Xiaodong Xu, and Brian C Sales. Magnetic behavior and spin-lattice coupling in cleavable van der waals layered crcl 3 crystals. *Physical Review Materials*, 1(1):014001, 2017.

[54] Weijong Chen, Zeyuan Sun, Zhongjie Wang, Lehua Gu, Xiaodong Xu, Shiwei Wu, and Chunlei Gao. Direct observation of van der waals stacking–dependent interlayer magnetism. *Science*, 366(6468):983–987, 2019.

[55] Michael A McGuire. Crystal and magnetic structures in layered, transition metal dihalides and trihalides. *Crystals*, 7(5):121, 2017.

[56] Alexei Kitaev. Anyons in an exactly solved model and beyond. *Annals of Physics*, 321(1):2–111, 2006.

[57] Zheng Zhu, Itamar Kimchi, DN Sheng, and Liang Fu. Robust non-abelian spin liquid and a possible intermediate phase in the antiferromagnetic kitaev model with magnetic field. *Physical Review B*, 97(24):241110, 2018.

[58] Matthias Gohlke, Roderich Moessner, and Frank Pollmann. Dynamical and topological properties of the kitaev model in a [111] magnetic field. *Physical Review B*, 98(1):014418, 2018.

[59] Niravkumar D Patel and Nandini Trivedi. Magnetic field-induced intermediate quantum spin liquid with a spinon fermi surface. *Proceedings of the National Academy of Sciences*, 116(25):12199–12203, 2019.

[60] Ciarán Hickey and Simon Trebst. Emergence of a field-driven u (1) spin liquid in the kitaev honeycomb model. *Nature communications*, 10(1):1–10, 2019.

[61] David AS Kaib, Stephen M Winter, and Roser Valenti. Kitaev honeycomb models in magnetic fields: Dynamical response and dual models. *Physical Review B*, 100(14):144445, 2019.

[62] Jacob S Gordon and Hae-Young Kee. Testing topological phase transitions in kitaev materials under in-plane magnetic fields: Application to $\alpha$- rucl 3. *Physical Review Research*, 3(1):013179, 2021.

[63] George Jackeli and Giniyat Khaliullin. Mott insulators in the strong spin-orbit coupling limit: from heisenberg to a quantum compass and kitaev models. *Physical review letters*, 102(1):017205, 2009.

[64] Stephen M Winter, Alexander A Tsirlin, Maria Daghofer, Jeroen van den Brink, Yogesh Singh, Philipp Gegenwart, and Roser Valenti. Models and materials for generalized kitaev magnetism. *Journal of Physics: Condensed Matter*, 29(49):493002, 2017.

[65] Jiří Chaloupka, George Jackeli, and Giniyat Khaliullin. Zigzag magnetic order in the iridium oxide na 2 iro 3. *Physical review letters*, 110(9):097204, 2013.

[66] Jeffrey G Rau, Eric Kin-Ho Lee, and Hae-Young Kee. Generic spin model for the honeycomb iridates beyond the kitaev limit. *Physical review letters*, 112(7):077204, 2014.

[67] Stephen M Winter, Ying Li, Harald O Jeschke, and Roser Valentí. Challenges in design of kitaev materials: Magnetic interactions from competing energy scales. *Physical Review B*, 93(21):214431, 2016.

[68] Roger D Johnson, SC Williams, AA Haghighirad, J Singleton, V Zapf, P Manuel, II Mazin, Y Li, Harald Olaf Jeschke, R Valentí, et al. Monoclinic crystal structure of $\alpha$- rucl 3 and the zigzag antiferromagnetic ground state. *Physical Review B*, 92(23):235119, 2015.

[69] Y Kasahara, T Ohnishi, Y Mizukami, O Tanaka, Sixiao Ma, K Sugii, N Kurita, H Tanaka, J Nasu, Y Motome, et al. Majorana quantization and half-integer thermal quantum hall effect in a kitaev spin liquid. *Nature*, 559(7713):227–231, 2018.

[70] T Yokoi, S Ma, Y Kasahara, S Kasahara, T Shibauchi, N Kurita, H Tanaka, J Nasu, Y Motome, C Hickey, et al. Half-integer quantized anomalous thermal hall effect in the kitaev material candidate $\alpha$-rucl3. *Science*, 373(6554):568–572, 2021.

[71] Luke J Sandilands, Yao Tian, Kemp W Plumb, Young-June Kim, and Kenneth S Burch. Scattering continuum and possible fractionalized excitations in $\alpha$- rucl 3. *Physical review letters*, 114(14):147201, 2015.

[72] Arnab Banerjee, Jiaqiang Yan, Johannes Knolle, Craig A Bridges, Matthew B Stone, Mark D Lumsden, David G Mandrus, David A Tennant, Roderich Moessner, and Stephen E Nagler. Neutron scattering in the proximate quantum spin liquid $\alpha$-rucl3. *Science*, 356(6342):1055–1059, 2017.

[73] Christian Balz, Paula Lampen-Kelley, Arnab Banerjee, Jiaqiang Yan, Zhilun Lu, Xinzhe Hu, Swapnil M Yadav, Yasu Takano, Yaohua Liu, D Alan Tennant, et al.

Finite field regime for a quantum spin liquid in $\alpha$- rucl 3. *Physical Review B*, 100(6):060405, 2019.

[74] Dirk Wulferding, Youngsu Choi, Seung-Hwan Do, Chan Hyeon Lee, Peter Lemmens, Clément Faugeras, Yann Gallais, and Kwang-Yong Choi. Magnon bound states versus anyonic majorana excitations in the kitaev honeycomb magnet $\alpha$-rucl3. *Nature communications*, 11(1):1–7, 2020.

[75] AN Ponomaryov, L Zviagina, J Wosnitza, P Lampen-Kelley, A Banerjee, J-Q Yan, CA Bridges, DG Mandrus, SE Nagler, and SA Zvyagin. Nature of magnetic excitations in the high-field phase of $\alpha$- rucl 3. *Physical Review Letters*, 125(3):037202, 2020.

[76] AN Ponomaryov, E Schulze, J Wosnitza, P Lampen-Kelley, A Banerjee, J-Q Yan, CA Bridges, DG Mandrus, SE Nagler, AK Kolezhuk, et al. Unconventional spin dynamics in the honeycomb-lattice material $\alpha$- rucl 3: High-field electron spin resonance studies. *Physical Review B*, 96(24):241107, 2017.

[77] A Sahasrabudhe, DAS Kaib, Stephan Reschke, R German, TC Koethe, J Buhot, Dmytro Kamenskyi, C Hickey, P Becker, Vladimir Tsurkan, et al. High-field quantum disordered state in $\alpha$- rucl 3: Spin flips, bound states, and multiparticle continuum. *Physical Review B*, 101(14):140410, 2020.

[78] Ravi Yadav, Nikolay A Bogdanov, Vamshi M Katukuri, Satoshi Nishimoto, Jeroen Van Den Brink, and Liviu Hozoi. Kitaev exchange and field-induced quantum spin-liquid states in honeycomb $\alpha$-rucl3. *Scientific reports*, 6(1):1–16, 2016.

[79] Yi-Fan Jiang, Thomas P Devereaux, and Hong-Chen Jiang. Field-induced quantum spin liquid in the kitaev-heisenberg model and its relation to $\alpha$- rucl 3. *Physical Review B*, 100(16):165123, 2019.

[80] Li Ern Chern, Ryui Kaneko, Hyun-Yong Lee, and Yong Baek Kim. Magnetic field induced competing phases in spin-orbital entangled kitaev magnets. *Physical Review Research*, 2(1):013014, 2020.

[81] Shang-Shun Zhang, Gábor B Halász, and Cristian D Batista. Theory of the kitaev model in a [111] magnetic field. *Nature Communications*, 13(1):1–7, 2022.

[82] Han Li, Hao-Kai Zhang, Jiucai Wang, Han-Qing Wu, Yuan Gao, Dai-Wei Qu, Zheng-Xin Liu, Shou-Shu Gong, and Wei Li. Identification of magnetic interactions and high-field quantum spin liquid in $\alpha$-rucl3. *Nature Communications*, 12(1):1–11, 2021.

[83] Kimberly A Modic, Ross D McDonald, JPC Ruff, Maja D Bachmann, You Lai, Johanna C Palmstrom, David Graf, Mun K Chan, FF Balakirev, JB Betts, et al. Scale-invariant magnetic anisotropy in rucl3 at high magnetic fields. *Nature Physics*, 17(2):240–244, 2021.

[84] Xu-Guang Zhou, Han Li, Yasuhiro H Matsuda, Akira Matsuo, Wei Li, Nobuyuki Kurita, Koichi Kindo, and Hidekazu Tanaka. Intermediate quantum spin liquid phase in the kitaev material $\alpha$-rucl _3 under high magnetic fields up to 100 t. *arXiv preprint arXiv:2201.04597*, 2022.

[85] Christian Balz, Lukas Janssen, Paige Lampen-Kelley, Arnab Banerjee, YH Liu, J-Q Yan, DG Mandrus, Matthias Vojta, and Stephen E Nagler. Field-induced intermediate ordered phase and anisotropic interlayer interactions in $\alpha$- rucl 3. *Physical Review B*, 103(17):174417, 2021.

[86] Heung-Sik Kim and Hae-Young Kee. Crystal structure and magnetism in $\alpha$- rucl 3: An ab initio study. *Physical Review B*, 93(15):155143, 2016.

[87] Jennifer A Sears, M Songvilay, KW Plumb, JP Clancy, Yiming Qiu, Yang Zhao, D Parshall, and Young-June Kim. Magnetic order in $\alpha$- rucl 3: A honeycomb-lattice quantum magnet with strong spin-orbit coupling. *Physical Review B*, 91(14):144420, 2015.

[88] JF Dillon Jr, H Kamimura, and JP Remeika. Magneto-optical properties of ferromagnetic chromium trihalides. *Journal of Physics and Chemistry of Solids*, 27(9):1531–1549, 1966.

[89] Hao Wang, Volker Eyert, and Udo Schwingenschlögl. Electronic structure and magnetic ordering of the semiconducting chromium trihalides crcl3, crbr3, and cri3. *Journal of Physics: Condensed Matter*, 23(11):116003, 2011.

[90] Soobin Sinn, Choong Hyun Kim, Beom Hyun Kim, Kyung Dong Lee, Choong Jae Won, Ji Seop Oh, Moonsup Han, Young Jun Chang, Namjung Hur, Hitoshi Sato, et al. Electronic structure of the kitaev material $\alpha$-rucl3 probed by photoemission and inverse photoemission spectroscopies. *Scientific reports*, 6(1):1–7, 2016.

[91] John G Simmons. Generalized formula for the electric tunnel effect between similar electrodes separated by a thin insulating film. *Journal of applied physics*, 34(6):1793–1803, 1963.

[92] Zheng-Wei Xie and Bo-Zang Li. Bias dependence of the tunneling magnetoresistance in double spin-filter junctions. *Journal of applied physics*, 93(11):9111–9115, 2003.

[93] Guo-Xing Miao, Martina Müller, and Jagadeesh S Moodera. Magnetoresistance in double spin filter tunnel junctions with nonmagnetic electrodes and its unconventional bias dependence. *Physical review letters*, 102(7):076601, 2009.

[94] Michael Galperin, Mark A Ratner, and Abraham Nitzan. Inelastic electron tunneling spectroscopy in molecular junctions: Peaks and dips. *The Journal of chemical physics*, 121(23):11965–11979, 2004.

[95] DC Tsui, RE Dietz, and LR Walker. Multiple magnon excitation in nio by electron tunneling. *Physical Review Letters*, 27(25):1729, 1971.

[96] Dahlia R Klein, David MacNeill, Jose L Lado, David Soriano, Efrén Navarro-Moratalla, Kenji Watanabe, Takashi Taniguchi, Soham Manni, Paul Canfield,

Joaquín Fernández-Rossier, et al. Probing magnetism in 2d van der waals crystalline insulators via electron tunneling. *Science*, 360(6394):1218–1222, 2018.

[97] J Klein, A Léger, M Belin, D Défourneau, and MJL Sangster. Inelastic-electron-tunneling spectroscopy of metal-insulator-metal junctions. *Physical Review B*, 7(6):2336, 1973.

[98] Matej Velicky, Gavin E Donnelly, William R Hendren, Stephen McFarland, Declan Scullion, William JI DeBenedetti, Gabriela Calinao Correa, Yimo Han, Andrew J Wain, Melissa A Hines, et al. Mechanism of gold-assisted exfoliation of centimeter-sized transition-metal dichalcogenide monolayers. *ACS nano*, 12(10):10463–10472, 2018.

[99] Fuad Indra Alzakia and Swee Ching Tan. Liquid-exfoliated 2d materials for optoelectronic applications. *Advanced Science*, 8(11):2003864, 2021.

[100] Riccardo Frisenda, Efrén Navarro-Moratalla, Patricia Gant, David Pérez De Lara, Pablo Jarillo-Herrero, Roman V Gorbachev, and Andres Castellanos-Gomez. Recent progress in the assembly of nanodevices and van der waals heterostructures by deterministic placement of 2d materials. *Chemical Society Reviews*, 47(1):53–68, 2018.

[101] B Raveau, A Maignan, C Martin, and M Hervieu. Colossal magnetoresistance manganite perovskites: relations between crystal chemistry and properties. *Chemistry of materials*, 10(10):2641–2652, 1998.

[102] AP Ramirez. Colossal magnetoresistance. *Journal of Physics: Condensed Matter*, 9(39):8171, 1997.

[103] L Esaki, PJ Stiles, and S Von Molnar. Magnetointernal field emission in junctions of magnetic insulators. *Physical Review Letters*, 19(15):852, 1967.

[104] Hyun Ho Kim, Bowen Yang, Tarun Patel, Francois Sfigakis, Chenghe Li, Shangjie Tian, Hechang Lei, and Adam W Tsen. One million percent tunnel magnetoresistance in a magnetic van der waals heterostructure. *Nano Letters*, 18(8):4885–4890, 2018.

[105] Wei-Bing Zhang, Qian Qu, Peng Zhu, and Chi-Hang Lam. Robust intrinsic ferromagnetism and half semiconductivity in stable two-dimensional single-layer chromium trihalides. *Journal of Materials Chemistry C*, 3(48):12457–12468, 2015.

[106] Liam Britnell, Roman V Gorbachev, Rashid Jalil, Branson D Belle, Fred Schedin, Mikhail I Katsnelson, Laurence Eaves, Sergey V Morozov, Alexander S Mayorov, Nuno MR Peres, et al. Electron tunneling through ultrathin boron nitride crystalline barriers. *Nano letters*, 12(3):1707–1710, 2012.

[107] Evgeny Y Tsymbal and David G Pettifor. Perspectives of giant magnetoresistance. In *Solid state physics*, volume 56, pages 113–237. Elsevier, 2001.

[108] Shengwei Jiang, Lizhong Li, Zefang Wang, Kin Fai Mak, and Jie Shan. Controlling magnetism in 2d cri3 by electrostatic doping. *Nature nanotechnology*, 13(7):549–553, 2018.

[109] RS Tebble. The barkhausen effect. *Proceedings of the Physical Society. Section B*, 68(12):1017, 1955.

[110] Ding Zhong, Kyle L Seyler, Xiayu Linpeng, Ran Cheng, Nikhil Sivadas, Bevin Huang, Emma Schmidgall, Takashi Taniguchi, Kenji Watanabe, Michael A McGuire, et al. Van der waals engineering of ferromagnetic semiconductor heterostructures for spin and valleytronics. *Science advances*, 3(5):e1603113, 2017.

[111] Olav Hellwig, Taryl L Kirk, Jeffrey B Kortright, Andreas Berger, and Eric E Fullerton. A new phase diagram for layered antiferromagnetic films. *Nature materials*, 2(2):112–116, 2003.

[112] Kyle L Seyler, Ding Zhong, Dahlia R Klein, Shiyuan Gao, Xiaoou Zhang, Bevin Huang, Efrén Navarro-Moratalla, Li Yang, David H Cobden, Michael A McGuire, et al. Ligand-field helical luminescence in a 2d ferromagnetic insulator. *Nature Physics*, 14(3):277–281, 2018.

[113] Martina Müller, Guo-Xing Miao, and Jagadeesh S Moodera. Exchange splitting and bias-dependent transport in euo spin filter tunnel barriers. *EPL (Europhysics Letters)*, 88(4):47006, 2009.

[114] M Lenzlinger and EH Snow. Fowler-nordheim tunneling into thermally grown sio2. *Journal of Applied physics*, 40(1):278–283, 1969.

[115] TS Santos, JS Moodera, KV Raman, E Negusse, J Holroyd, J Dvorak, M Liberati, YU Idzerda, and E Arenholz. Determining exchange splitting in a magnetic semiconductor by spin-filter tunneling. *Physical review letters*, 101(14):147201, 2008.

[116] Hyun Ho Kim, Bowen Yang, Siwen Li, Shengwei Jiang, Chenhao Jin, Zui Tao, George Nichols, Francois Sfigakis, Shazhou Zhong, Chenghe Li, et al. Evolution of interlayer and intralayer magnetism in three atomically thin chromium trihalides. *Proceedings of the National Academy of Sciences*, 116(23):11131–11136, 2019.

[117] Tiancheng Song, Xinghan Cai, Matisse Wei-Yuan Tu, Xiaoou Zhang, Bevin Huang, Nathan P Wilson, Kyle L Seyler, Lin Zhu, Takashi Taniguchi, Kenji Watanabe, et al. Giant tunneling magnetoresistance in spin-filter van der waals heterostructures. *Science*, 360(6394):1214–1218, 2018.

[118] Zhe Wang, Ignacio Gutiérrez-Lezama, Nicolas Ubrig, Martin Kroner, Marco Gibertini, Takashi Taniguchi, Kenji Watanabe, Ataç Imamoğlu, Enrico Giannini, and Alberto F Morpurgo. Very large tunneling magnetoresistance in layered magnetic semiconductor cri3. *Nature communications*, 9(1):1–8, 2018.

[119] X Hao, JS Moodera, and R Meservey. Spin-filter effect of ferromagnetic europium sulfide tunnel barriers. *Physical review B*, 42(13):8235, 1990.

[120] Bevin Huang, Genevieve Clark, Dahlia R Klein, David MacNeill, Efrén Navarro-Moratalla, Kyle L Seyler, Nathan Wilson, Michael A McGuire, David H Cobden, Di Xiao, et al. Electrical control of 2d magnetism in bilayer cri3. *Nature nanotechnology*, 13(7):544–548, 2018.

[121] Shengwei Jiang, Jie Shan, and Kin Fai Mak. Electric-field switching of two-dimensional van der waals magnets. *Nature materials*, 17(5):406–410, 2018.

[122] Davit Ghazaryan, Mark T Greenaway, Zihao Wang, Victor H Guarochico-Moreira, Ivan J Vera-Marun, Jun Yin, Yuanxun Liao, Serge V Morozov, Oleg Kristanovski, Alexander I Lichtenstein, et al. Magnon-assisted tunnelling in van der waals heterostructures based on crbr3. *Nature Electronics*, 1(6):344–349, 2018.

[123] Wencan Jin, Hyun Ho Kim, Zhipeng Ye, Siwen Li, Pouyan Rezaie, Fabian Diaz, Saad Siddiq, Eric Wauer, Bowen Yang, Chenghe Li, et al. Raman fingerprint of two terahertz spin wave branches in a two-dimensional honeycomb ising ferromagnet. *Nature communications*, 9(1):1–7, 2018.

[124] Lebing Chen, Jae-Ho Chung, Bin Gao, Tong Chen, Matthew B Stone, Alexander I Kolesnikov, Qingzhen Huang, and Pengcheng Dai. Topological spin excitations in honeycomb ferromagnet cri 3. *Physical Review X*, 8(4):041028, 2018.

[125] KW Plumb, JP Clancy, LJ Sandilands, V Vijay Shankar, YF Hu, KS Burch, Hae-Young Kee, and Young-June Kim. $\alpha$- rucl 3: A spin-orbit assisted mott insulator on a honeycomb lattice. *Physical Review B*, 90(4):041112, 2014.

[126] Hidenori Takagi, Tomohiro Takayama, George Jackeli, Giniyat Khaliullin, and Stephen E Nagler. Concept and realization of kitaev quantum spin liquids. *Nature Reviews Physics*, 1(4):264–280, 2019.

[127] S-Y Park, S-H Do, K-Y Choi, D Jang, T-H Jang, J Schefer, C-M Wu, JS Gardner, JMS Park, J-H Park, et al. Emergence of the isotropic kitaev honeycomb lattice with two-dimensional ising universality in $\alpha$-rucl$_3$. *arXiv preprint arXiv:1609.05690*, 2016.

[128] Huibo B Cao, A Banerjee, J-Q Yan, CA Bridges, MD Lumsden, DG Mandrus, DA Tennant, BC Chakoumakos, and SE Nagler. Low-temperature crystal and magnetic structure of $\alpha$- rucl 3. *Physical Review B*, 93(13):134423, 2016.

[129] LY Shi, YQ Liu, T Lin, MY Zhang, SJ Zhang, L Wang, YG Shi, T Dong, and NL Wang. Field-induced magnon excitation and in-gap absorption in the kitaev candidate rucl 3. *Physical Review B*, 98(9):094414, 2018.

[130] Ilkem Ozge Ozel, Carina A Belvin, Edoardo Baldini, Itamar Kimchi, Seunghwan Do, Kwang-Yong Choi, and Nuh Gedik. Magnetic field-dependent low-energy magnon dynamics in $\alpha$–rucl 3. *Physical Review B*, 100(8):085108, 2019.

[131] A Banerjee, CA Bridges, J-Q Yan, AA Aczel, L Li, MB Stone, GE Granroth, MD Lumsden, Y Yiu, Johannes Knolle, et al. Proximate kitaev quantum spin liquid behaviour in a honeycomb magnet. *Nature materials*, 15(7):733–740, 2016.

[132] Kejing Ran, Jinghui Wang, Wei Wang, Zhao-Yang Dong, Xiao Ren, Song Bao, Shichao Li, Zhen Ma, Yuan Gan, Youtian Zhang, et al. Spin-wave excitations evidencing the kitaev interaction in single crystalline $\alpha$- rucl 3. *Physical review letters*, 118(10):107203, 2017.

[133] Arielle Little, Liang Wu, Paula Lampen-Kelley, Arnab Banerjee, Shreyas Patankar, Dylan Rees, CA Bridges, J-Q Yan, David Mandrus, SE Nagler, et al. Antiferromagnetic resonance and terahertz continuum in $\alpha$- rucl 3. *Physical review letters*, 119(22):227201, 2017.

[134] Zhe Wang, Stephan Reschke, D Hüvonen, S-H Do, K-Y Choi, M Gensch, U Nagel, T Rõõm, and Alois Loidl. Magnetic excitations and continuum of a possibly field-induced quantum spin liquid in $\alpha$- rucl 3. *Physical review letters*, 119(22):227202, 2017.

[135] Arnab Banerjee, Paula Lampen-Kelley, Johannes Knolle, Christian Balz, Adam Anthony Aczel, Barry Winn, Yaohua Liu, Daniel Pajerowski, Jiaqiang Yan, Craig A Bridges, et al. Excitations in the field-induced quantum spin liquid state of $\alpha$-rucl3. *npj Quantum Materials*, 3(1):1–7, 2018.

[136] Liang Wu, Arielle Little, Erik E Aldape, Dylan Rees, Eric Thewalt, Paula Lampen-Kelley, Arnab Banerjee, Craig A Bridges, J-Q Yan, Derrick Boone, et al. Field evolution of magnons in $\alpha$- rucl 3 by high-resolution polarized terahertz spectroscopy. *Physical Review B*, 98(9):094425, 2018.

[137] T Harada, I Ohkubo, M Lippmaa, Y Sakurai, Y Matsumoto, S Muto, H Koinuma, and M Oshima. Spin-filter tunnel junction with matched fermi surfaces. *Physical review letters*, 109(7):076602, 2012.

[138] John Lambe and RC Jaklevic. Molecular vibration spectra by inelastic electron tunneling. *Physical Review*, 165(3):821, 1968.

[139] Fabian Donat Natterer, François Patthey, and Harald Brune. Distinction of nuclear spin states with the scanning tunneling microscope. *Physical review letters*, 111(17):175303, 2013.

[140] Xinrun Mi, Xiao Wang, Hengrui Gui, Maocai Pi, Tingting Zheng, Kunya Yang, Yuhan Gan, Peipei Wang, Alei Li, Aifeng Wang, et al. Stacking faults in $\alpha$- rucl 3 revealed by local electric polarization. *Physical Review B*, 103(17):174413, 2021.

[141] Haoxiang Li, TT Zhang, A Said, Gilberto Fabbris, Daniel G Mazzone, JQ Yan, David Mandrus, Gábor B Halász, Satoshi Okamoto, S Murakami, et al. Giant phonon anomalies in the proximate kitaev quantum spin liquid $\alpha$-rucl3. *Nature communications*, 12(1):1–7, 2021.

[142] Stephen M Winter, Kira Riedl, Pavel A Maksimov, Alexander L Chernyshev, Andreas Honecker, and Roser Valentí. Breakdown of magnons in a strongly spin-orbital coupled magnet. *Nature communications*, 8(1):1–8, 2017.

[143] Jiří Chaloupka and Giniyat Khaliullin. Magnetic anisotropy in the kitaev model systems na 2 iro 3 and rucl 3. *Physical Review B*, 94(6):064435, 2016.

[144] Thuc T Mai, Amber McCreary, Paige Lampen-Kelley, Nicholas Butch, Jeffrey R Simpson, J-Q Yan, Stephen E Nagler, David Mandrus, AR Hight Walker, and R Valdés Aguilar. Polarization-resolved raman spectroscopy of $\alpha$- rucl 3 and evidence of room-temperature two-dimensional magnetic scattering. *Physical Review B*, 100(13):134419, 2019.

[145] David AS Kaib, Sananda Biswas, Kira Riedl, Stephen M Winter, and Roser Valentí. Magnetoelastic coupling and effects of uniaxial strain in $\alpha$- rucl 3 from first principles. *Physical Review B*, 103(14):L140402, 2021.

[146] Ravi Yadav, Stephan Rachel, Liviu Hozoi, Jeroen van den Brink, and George Jackeli. Strain-and pressure-tuned magnetic interactions in honeycomb kitaev materials. *Physical Review B*, 98(12):121107, 2018.

[147] Sebastian Bachus, David AS Kaib, Yoshifumi Tokiwa, Anton Jesche, Vladimir Tsurkan, Alois Loidl, Stephen M Winter, Alexander A Tsirlin, Roser Valenti, and Philipp Gegenwart. Thermodynamic perspective on field-induced behavior of $\alpha$- rucl 3. *Physical Review Letters*, 125(9):097203, 2020.

[148] PA Maksimov and AL Chernyshev. Rethinking $\alpha$- rucl 3. *Physical Review Research*, 2(3):033011, 2020.

[149] Boyi Zhou, J Balgley, Paula Lampen-Kelley, J-Q Yan, David G Mandrus, and Erik A Henriksen. Evidence for charge transfer and proximate magnetism in graphene–$\alpha$-rucl 3 heterostructures. *Physical Review B*, 100(16):165426, 2019.

[150] Yiping Wang, Jesse Balgley, Eli Gerber, Mason Gray, Narendra Kumar, Xiaobo Lu, Jia-Qiang Yan, Arash Fereidouni, Rabindra Basnet, Seok Joon Yun, et al. Modulation doping via a two-dimensional atomic crystalline acceptor. *Nano letters*, 20(12):8446–8452, 2020.

[151] Sananda Biswas, Ying Li, Stephen M Winter, Johannes Knolle, and Roser Valentí. Electronic properties of $\alpha$- rucl 3 in proximity to graphene. *Physical Review Letters*, 123(23):237201, 2019.

[152] Zhongwei Dai, Jie-Xiang Yu, Boyi Zhou, Samuel A Tenney, Paula Lampen-Kelley, Jiaqiang Yan, David Mandrus, Erik A Henriksen, Jiadong Zang, Karsten Pohl, et al. Crystal structure reconstruction in the surface monolayer of the quantum spin liquid candidate $\alpha$-rucl3. *2D Materials*, 7(3):035004, 2020.

[153] Tingxin Li, Shengwei Jiang, Nikhil Sivadas, Zefang Wang, Yang Xu, Daniel Weber, Joshua E Goldberger, Kenji Watanabe, Takashi Taniguchi, Craig J Fennie, et al. Pressure-controlled interlayer magnetism in atomically thin cri3. *Nature materials*, 18(12):1303–1308, 2019.

[154] Lucas Webster and Jia-An Yan. Strain-tunable magnetic anisotropy in monolayer crcl 3, crbr 3, and cri 3. *Physical Review B*, 98(14):144411, 2018.

[155] Yuan Cao, Valla Fatemi, Shiang Fang, Kenji Watanabe, Takashi Taniguchi, Efthimios Kaxiras, and Pablo Jarillo-Herrero. Unconventional superconductivity in magic-angle graphene superlattices. *Nature*, 556(7699):43–50, 2018.

[156] Yang Xu, Ariana Ray, Yu-Tsun Shao, Shengwei Jiang, Kihong Lee, Daniel Weber, Joshua E Goldberger, Kenji Watanabe, Takashi Taniguchi, David A Muller, et al. Coexisting ferromagnetic–antiferromagnetic state in twisted bilayer cri3. *Nature Nanotechnology*, 17(2):143–147, 2022.

[157] Hongchao Xie, Xiangpeng Luo, Gaihua Ye, Zhipeng Ye, Haiwen Ge, Suk Hyun Sung, Emily Rennich, Shaohua Yan, Yang Fu, Shangjie Tian, et al. Twist engineering of the two-dimensional magnetism in double bilayer chromium triiodide homostructures. *Nature Physics*, 18(1):30–36, 2022.

# APPENDICES

# Appendix A

# Cryogenic Setup

Magnetotransport measurements were performed in an He-4 cryostat (base temperature 1.4 K, magnetic field limit 14 T) and an He-3 cryostat (base temperature 0.3 K, magnetic field limit 12 T) with superconducting magnets (Figure A.1). The superconducting magnet He-3 cryostat was used for IETS devices ($CrX_3$ and $\alpha$-$RuCl_3$ with Gr contacts). Both setups have a single-axis rotator for the sample stage. PID control loops were used for precisely stabilizing sample temperature in the two crystats.

## A.1 He-4 Cryogenic System

The superconducting magnet is immersed in liquid He-4 below 4K. The temperature is maintained by the cold head. A controllable valve connects the sample chamber with the He-4 reservoir. As the chamber is pumped from the top, liquid He-4 is transferred into the chamber through the valve and vaporized. At low pressure, the He-4 vapour could reach as low as 1.4 K near the sample space. The pumped He-4 gas is recycled back to the He-4 reservoir.

## A.2 He-3 Cryogenic System

The 1K pot contains vapor-liquid He-4 mixture. Similar to the He-4 system, as the He-4 is pumped out, the 1K pot could remain nearly 1 K for cooling and condensing He-3. To cool the sample down to 0.3 K, first of all, we need to warm the charcoal to release the adsorbed He-3 gas. As it go through the 1K pot, it is condensed and the liquid He-3 will be collected at the bottom of the probe, which is attached with the sample holder. Then we lower the charcoal temperature to 4 K, which cryopumps the liquid He-3 and reaches 0.3 K. As the liquid He-3 is evaporating, the gas returns to the sorb and is recollected for the next cooling.

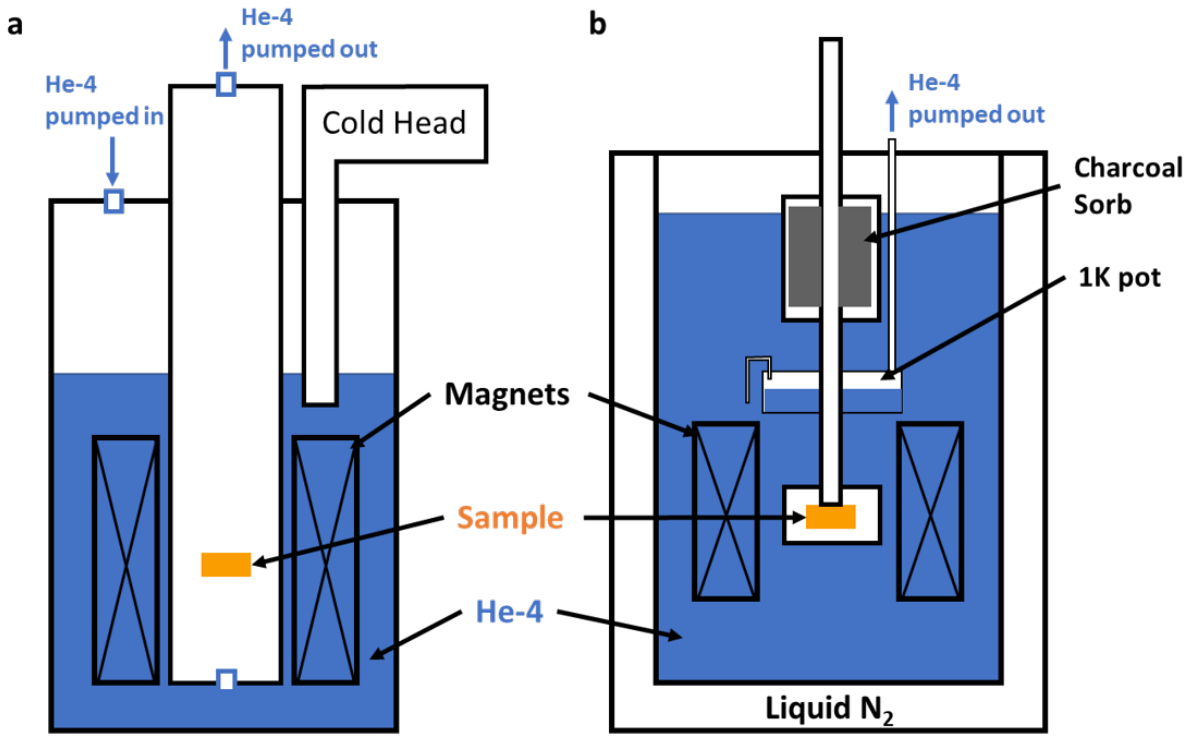


Figure A.1: Schematic for (a) the He-4 cryostat and (b) the He-3 cryostat.

# Appendix B

# Tunneling and Lateral Transport Measurements

We applied a current/voltage bias with Keithley 2450 in order to measure tunneling magnetoresistance for $CrX_3$ (Figure B.1 a). The voltage was applied between the top and bottom graphite electrodes and the value of tunneling current was captured by Keithley simultaneously. Typically, the upper limit for tunneling current was set to be 10 nA in case of electrical breakdown.

In Chapter 7, we performed a lateral transport measurement for $\alpha$-$RuCl_3$ with dual gate voltages (Figure B.1 b). To apply gate voltages, here few-layer h-BN was used as dielectric layers. In case of electrical breakdown, the leakage currents limit for both gates was set to be 0.1 nA. As we measured IV characteristic curves, a third Keithley unit was used to apply source-drain voltage (not shown in Figure B.1 b). With the optimized settings for gate voltages, we measured AC lateral conductance for electron-doped $\alpha$-$RuCl_3$ with Stanford Research SRS860 lock-in amplifier. Compared with SRS830, SRS860 is able to add a DC bias with AC output. Benefiting from this feature, we added 20 mV to the output for enhancing signal-to-noise ratio.

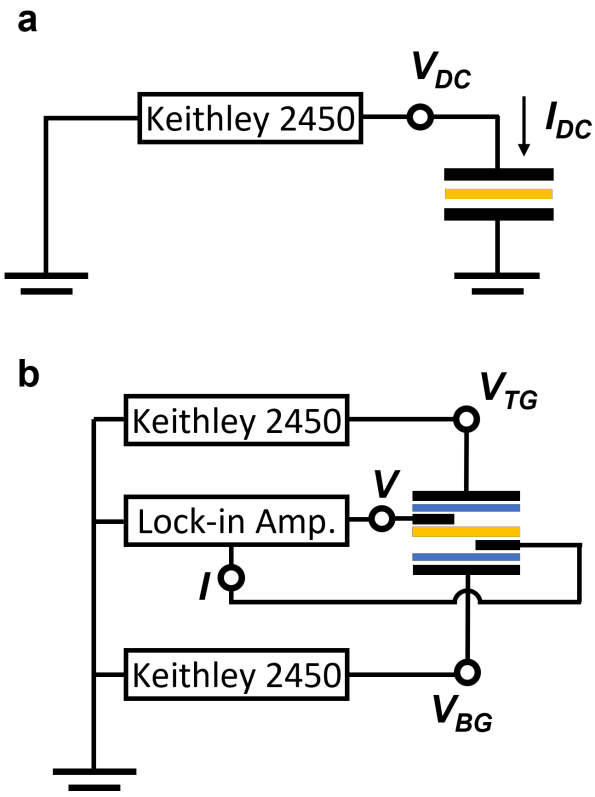


Figure B.1: Circuit designs for (a) tunneling magnetoresistance and (b) lateral transport measurement with dual gates. (a) The two black blocks represent the top and bottom electrodes, and the yellow block represents the few-layer $CrX_3$. As a constant voltage (current) is applied between the two electrodes, the Keithley 2450 is able to measure the tunneling current (applied voltage) simultaneously. (b) The two blue blocks represent the top and bottom h-BN, and the yellow block represents monolayer $\alpha$-$RuCl_3$. The two gate voltages are produced by two separate Keithley 2450's with the same common ground. The AC conductance is measured by Stanford Research SRS860 lock-in amplifier. To obtain IV characteristic curves, the lock-in amplifier was substituted by another Keithley 2450.

# Appendix C

# IETS

In the IETS measurements, AC conductance is measured as a function of DC voltage bias, which requires an AC excitation to be applied on top of DC voltage bias.

DC bias was applied by a Keithley 2450 source measure unit, and AC excitation was performed by a Stanford Research SRS830 lock-in amplifier. The circuit is shown in Figure C.1. If the resistor $R_3$ (usually chosen as 50 Ω) is especially smaller than the sample resistance (in most cases, the value is around 1 to 10 MΩ), then the DC and AC voltage bias can be estimated as $V_{DC} = \frac{R_3}{R_2+R_3} V_{DC,in}$ and $V_{AC} = \frac{R_3}{R_1+R_3} V_{AC,in}$, respectively, independent of the resistance of any given sample. To minimize the instrumental broadening for the tunnelling spectrum, the AC excitation should be set below 1 mV (typically the value is 100 $\mu$V to 500 $\mu$V).

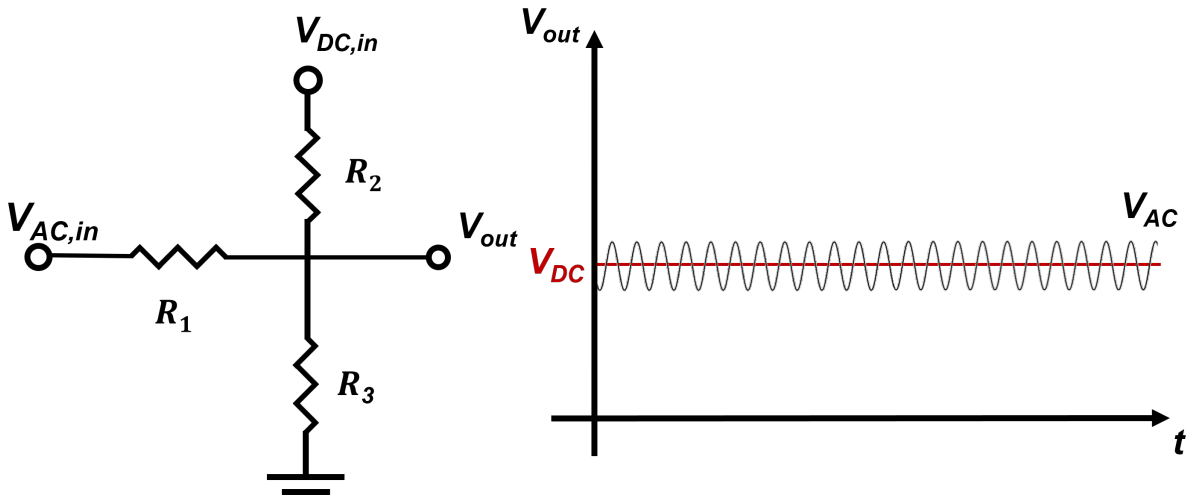


Figure C.1: IETS circuit setup. Left: the IETS circuit with output voltage $V_{out}$. Right: output from the circuit, consisting of $V_{DC}$ and $V_{AC}$.

However, if the lock-in amplifier itself is able to add a DC bias together with AC signal, for example, Stanford Research SRS860 lock-in amplifier, its output can be directly used as $V_{out}$ instead of using the circuit shown in Figure C.1.